Studies on the optogenetic tools to decrease the intracellular contractile force

細胞内収縮力を低減する光遺伝学技術に関する研究

Yamamoto, Kei

The Graduate University for Advanced Studies,
SOKENDAI
School of Life Science
Department of Basic Biology

Table of contents

List of figures

Abbreviations

actin filaments	F-actin
atomic force microscopy	AFM
cryptochrome 2	CRY2
cryptochrome 2-interacting bHLH1	CIB1
ezrin-radixin-moesin	ERM
improved light-induced dimer	iLID
light inducible dimerization	LID
myosin heavy chain	MHC
myosin light chain	MLC
myosin light chain kinase	MLCK
myosin light chain phosphatase	MLCP
nonmuscle myosin II	NMII
nuclear export signal	NES
PP1c-binding domain	PP1BD
protein of interest	POI
protein phosphatase 1c	PP1c
region of interest	ROI
Rho-kinase	ROCK

Abstract

Actomyosin contractility generated cooperatively by nonmuscle myosin II (NMII) and actin filaments (F-actin) plays essential roles in a wide range of biological processes, such as cell motility, cytokinesis, and tissue morphogenesis. To manipulate the function of contractile force, small chemical compounds have been widely used. While these compounds have allowed researchers to better understand the function of NMII, it is still technically challenging to control their actions at the subcellular resolution because of their rapid diffusion. To overcome the limitation, recent efforts have been devoted to the development and application of optogenetic tools to manipulate cell signaling related to actomyosin contractility by light. Although many of these tools enhance actomyosin contractility, tools that decrease actomyosin contractility below the basal level have not yet been developed. In this study, I developed an optogenetic tool, named OptoMYPT, to decrease actomyosin contractility at the subcellular level.

The NMII is inactivated by the dephosphorylation of its own myosin regulatory light chains (MLCs). To decrease the intracellular contractile force by optogenetics, I focused on MYPT1, which is a regulatory subunit of myosin light chain phosphatase. The strategy of OptoMYPT to decrease contractile force is based on the light-inducible plasma membrane recruitment of PP1c-binding domain (PP1BD) in MYPT1. This results in the co-recruitment of endogenous PP1c and dephosphorylation of MLC beneath the plasma membrane. As an optogenetic switch, I mainly used the improved Light-Induced Dimer (iLID) protein, which binds to its binding partner, SspB, upon blue light illumination and dissociates from SspB under the dark condition. I optimized the length of PP1BD for the efficient light-induced membrane translocation of the PP1BD and exogenous/endogenous PP1c.

To evaluate whether the OptoMYPT dephosphorylates MLC in a blue light-dependent manner, I first observed phosphorylated MLC with immunofluorescence. The blue light was

locally illuminated at the lamellipodia in Madin-Darby Canine Kidney (MDCK) cells expressing OptoMYPT proteins. The quantification of fluorescence intensity in dark and light-illuminated areas revealed a significant reduction in the phosphorylated MLC level. Second, I confirmed that the global blue light illumination decreased the phosphorylated MLC level by western blotting analysis. Third, local membrane protrusions were observed in the light-illuminated lamellipodial region, consistent with the morphology of the cells treated with NMII inhibitors.

Next, I examined whether the decrease in MLC phosphorylation by OptoMYPT affects actomyosin-based contractile force. To do this, I employed traction force microscopy, a method of estimating the force generated by cells pulling on a substrate. The traction force was decreased by local blue light illumination to the lamellipodial region in randomly migrating MDCK cells. I further applied OptoMYPT to the *in vivo* system by using *Xenopus laevis* embryos. The cell-cell junctions became wavy in shape by blue light illumination, suggesting decreased actomyosin contractility. For further validation, I combined laser ablation with optogenetic experiments, because junctional tension can be estimated by the recoil velocity between two vertices after ablation. The recoil velocity was significantly slower in OptoMYPT cells than in control cells, directly indicating the reduced tension at the cell-cell junction by OptoMYPT.

Finally, I applied the OptoMYPT system to elucidate the mechanical regulation of the actin cortex during cytokinesis. In this process, actin, NMII, and cross-linkers constitute a contractile ring in the equatorial plane, and generate force to divide a cell into two daughter cells. On the other hand, the tension developed in cortical actomyosin counteracts the force in the contractile ring. Due to the highly dynamic nature of cytokinesis, it is still challenging to understand to what extent the cortical actomyosin contributes to ring constriction. Using OptoMYPT, I found that the relaxation of cortical tension at both poles accelerated the furrow

ingression rate, revealing that the cortical tension substantially antagonizes constriction of the cleavage furrow. By combining the coarse-grained physical model with the experimental data, I estimated that the resisting force exerted by the cortices corresponds to 15~31% of the ring tension.

In summary, I developed the OptoMYPT system, which dephosphorylates MLC and decreases actomyosin contractility in a blue light-dependent manner. Using OptoMYPT, I quantitatively estimated the force balance between the actin cortex and the contractile ring during cytokinesis. The OptoMYPT system will provide new opportunities not only to understand cellular and tissue mechanics but also to shape the morphology of cells and tissues with precision and flexibility as desired.

1. General introduction

1.1. Roles of actomyosin contractility

Every eukaryotic cell expresses three types of cytoskeletal proteins: actin filaments (F-actin), microtubules, and intermediate filaments (Huber et al. 2015). These filamentous proteins, which dynamically polymerize and depolymerize, function not only to maintain cell morphology but also to serve as signaling hubs and as scaffolds for protein transport. Among cytoskeletal proteins, the actin cytoskeleton is important for the generation of contractility, which underlies force generation in a wide range of cellular and tissue morphogenesis (Murrell et al. 2015). Prominent examples include the tail retraction of directionally migrating fibroblasts and the constriction of a contractile ring during cytokinesis (Green, Paluch, and Oegema 2012; Ridley et al. 2003). Recently, amoeboid migration, which does not depend on cell-substrate adhesion, has also been focused on in the study of cell migration (Liu et al. 2015; Ruprecht et al. 2015). This mode of migration is driven by actomyosin contractility in the actin cortex (see below) and is 10 times faster than the previously observed mesenchymal migration. Such various modes of migrations are observed *in vivo* in wound healing, cancer invasion, and neutrophil migration (Paluch, Aspalter, and Sixt 2016). In a multicellular context, contraction of actomyosin at the apical surface allows for epithelial folding (Martin and Goldstein 2014). This apical constriction is an essential event during development, such as neural tube closure and gastrulation. It has also been reported that tumors retrieved from patients with metastatic colorectal cancer undergo collective amoeboid migration driven by actomyosin contractility as well as single-cell amoeboid migration (Pagès et al. 2020; Zajac et al. 2018). Thus, it is of critical importance to disentangle the mode of action of actomyosin in order to understand how cells generate force and shape their morphology.

1.2. Mechanisms of contractile force generation by nonmuscle myosin II

The actomyosin contractility in nonmuscle cells is mainly attributed to the force generated by nonmuscle myosin II (NMII) (M. Vicente-Manzanares et al. 2009). NMII contains two heavy chains, two essential light chains, and two regulatory light chains (MLCs) (M. Vicente-Manzanares et al. 2009; Heissler and Manstein 2013) (Fig. 1). These subunits form two globular heads and a long α-helical coiled-coil rod-like tail, which are involved in actin binding and motor activity, and bipolar filaments formation, respectively. The MLCs are phosphorylated by myosin light chain kinase (MLCK) and Rho-kinase (ROCK), thereby inducing a conformational change in NMII and increasing its motor activity (M. Vicente-Manzanares et al. 2009) (Fig. 2). The extended conformation of active NMII form bipolar filaments, leading to the generation of the contractile force together with actin filaments (Fig. 1). On the other hand, dephosphorylation of MLCs is achieved by myosin light chain phosphatase (MLCP), which is composed of three subunits, a catalytic subunit (PP1c), a regulatory subunit (MYPT1), and a smaller subunit of 20-kDa (M20) (Ito et al. 2004), leading to the decrease in contractile force (Fig. 2).

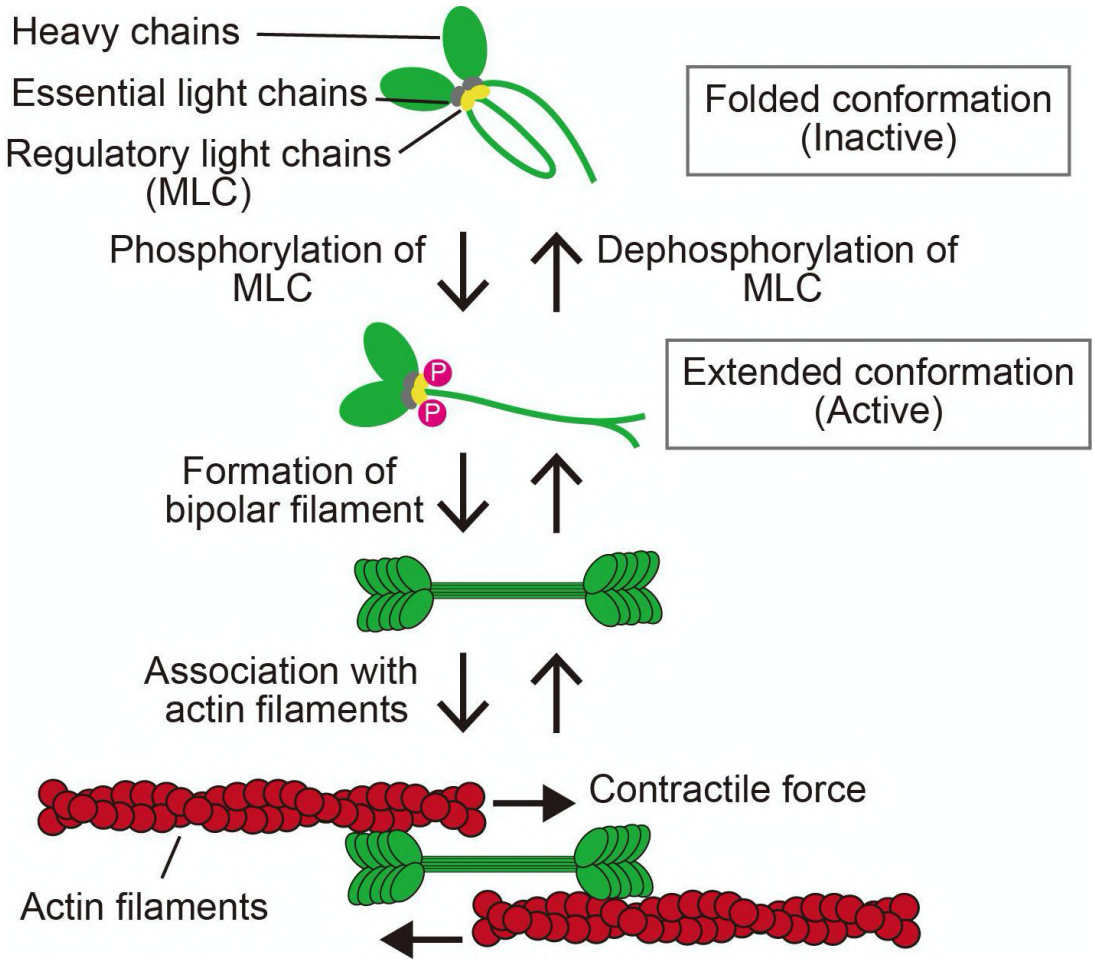

Figure 1. Conformational changes of NMII to generate contractile force.
Schematic illustration of the molecular mechanism to generate contractile force. NMII is composed of two heavy chains, two essential light chains, and two regulatory light chains (upper). Folded conformation of NMII is extended by the phosphorylation of its regulatory light chains (middle). Extended NMII filaments form bipolar filaments, leading to the generation of contractile force between actin filaments (lower).

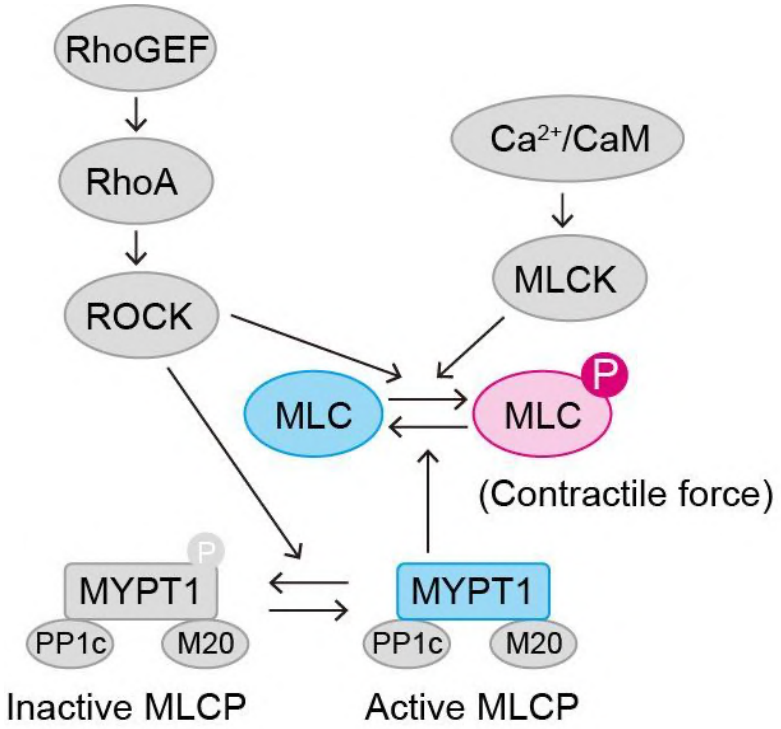

Figure 2. Signaling pathway for the regulation of MLC phosphorylation.
Schematic illustration of the signaling pathway for the regulation of MLC phosphorylation. MLC is phosphorylated by ROCK or MLCK, and dephosphorylated by MLCP complex. MLCP complex is composed of MYPT1, PP1c, and M20. ROCK phosphorylates MYPT1, leading to the inactivation of MLCP complex.

1.3. Structure of the actin cortex

The actin cortex is a mesh-like layer of F-actin that is located beneath the plasma membrane in most animal cells (Fig. 3). The main roles of the actin cortex are to resist extracellular mechanical stresses, and to allow cells to flexibly change their morphologies, such as cytokinesis, amoeboid cell migration, and membrane blebbing. In order to achieve such a dynamic morphological changes, the turnover of the proteins constituting actin cortex is fast (several tens of seconds) (Murthy and Wadsworth 2005; Kondo et al. 2011), and the thickness of actin cortex fluctuates dynamically (Laplaud et al. 2021). The thickness of the actin cortex is ~200 and ~400 nm in M phase cells and trypsinized interphase cells, respectively (Chugh et al. 2017). For the deformation of the cortex, NMII generates cortical tension and the ezrin-radixin-moesin (ERM) family proteins connect the actin cortex with the plasma membrane (Kelkar, Bohec, and Charras 2020). In addition, actin bundling proteins, such as α-actinin, stabilize the cortex structure.

The key factors to generate proper cortical tension are the mesh size of the cortex and the distribution of the NMII filaments. Based on scanning electron micrograph observations, the average mesh size of the cortex is ~50 nm. To achieve this mesh size, the activity of actin polymerization factors such as formin and depolymerization factors such as cofilin need to be maintained at appropriate levels (Chugh et al. 2017). If the density of the mesh is too low, NMII cannot cross-link F-actin and generate contractile force. If the density of the mesh is too high, the network is excessively rigid. Furthermore, in this situation, it has been reported that myosin bipolar-filaments, which is ~300 nm, cannot sterically penetrate the cortex from the cytoplasm (Truong Quang et al. 2021). Thus, cortical tension is tightly regulated by upstream signaling pathways and the structure of the cortex itself.

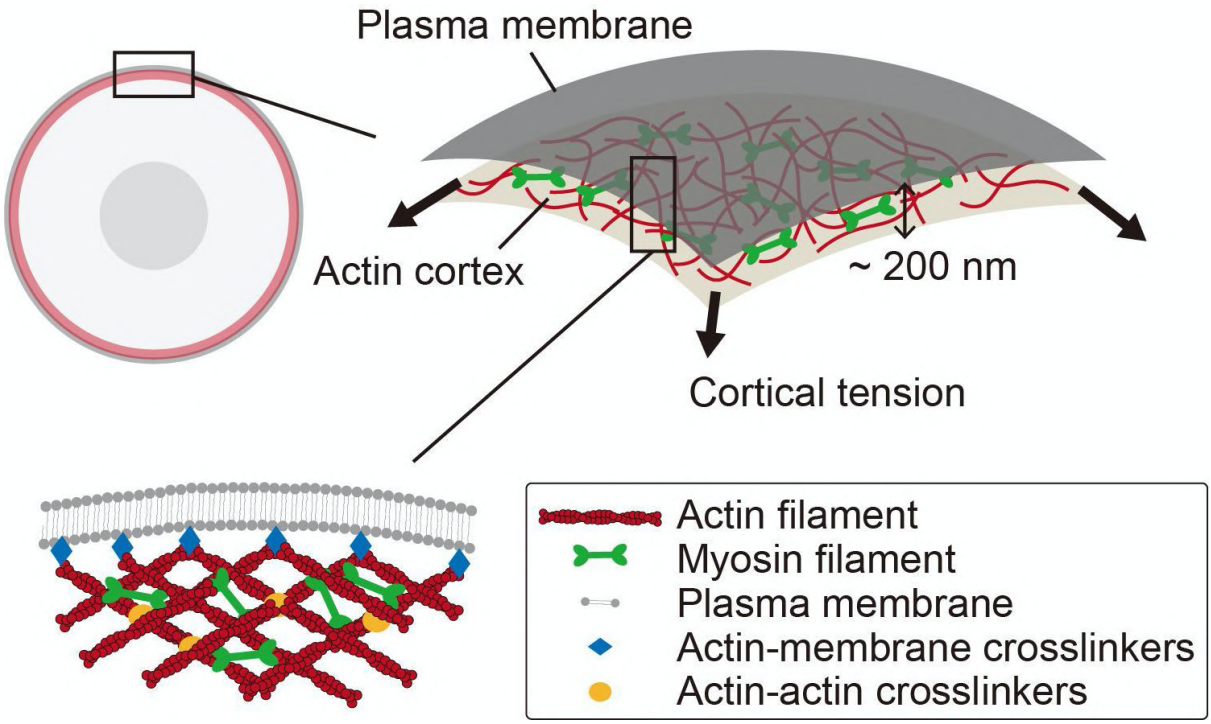

Figure 3. Structure of the actin cortex.
Schematic illustration of the actin cortex in animal cells. Myosin filaments generate contractile force between F-actins, leading to the generation of cortical tension. Actin-membrane crosslinkers, such as ERM family proteins, connect the cortex with the plasma membrane. Actin-actin crosslinkers, such as α-actinin, stabilize the cortex structure.

1.4. Advances of the optogenetics

To analyze the function of contractile force in various cellular processes, small chemical compounds have been widely used to perturb the actomyosin contractility, such as blebbistatin (an inhibitor for NMII ATPase activity), Y-27632 (a ROCK inhibitor), and ML-7 (an MLCK inhibitor) (Straight et al. 2003; Uehata et al. 1997; Saitoh et al. 1987). While these compounds have allowed researchers to better understand the function of NMII, it is still technically challenging to control their actions at the subcellular resolution because of their rapid diffusion.

To overcome the limitation, recent efforts have been devoted to the development and application of optogenetic tools to manipulate cell signaling related to actomyosin contractility (Krueger et al. 2019). Optogenetics is a technology for manipulating cellular functions using light-responsive proteins derived from plants and bacteria. As an optogenetic system, light inducible dimerization (LID) has been widely used, because the LID system allows us to reversibly control the localization of the protein of interest (POI) (Fig. 4). So far, optogenetic tools that respond to various wavelengths have been reported, such as iLID-SspB (Guntas et al. 2015) and CRY2-CIB (Kennedy et al. 2010), which respond to blue light, and PhyB-PIF (Uda et al. 2017), which responds to red/near-infrared light. In the iLID-SspB system, the iLID protein is composed of AsLOV2 and SsrA, which is derived from *Avena Sativa* and *Escherichia coli*, respectively. Upon blue light illumination, the structural change of AsLOV2 enables SsrA to bind with SspB, which is derived from *E. coli* (Fig. 4, left). In the CRY2-CIB system, cryptochrome 2 (CRY2) and CRY2-interacting bHLH1 (CIB1) are derived from *Arabidppsis thaliana*. Blue light illumination activates CRY2, leading to the binding with CIB1 (Fig. 4, right).

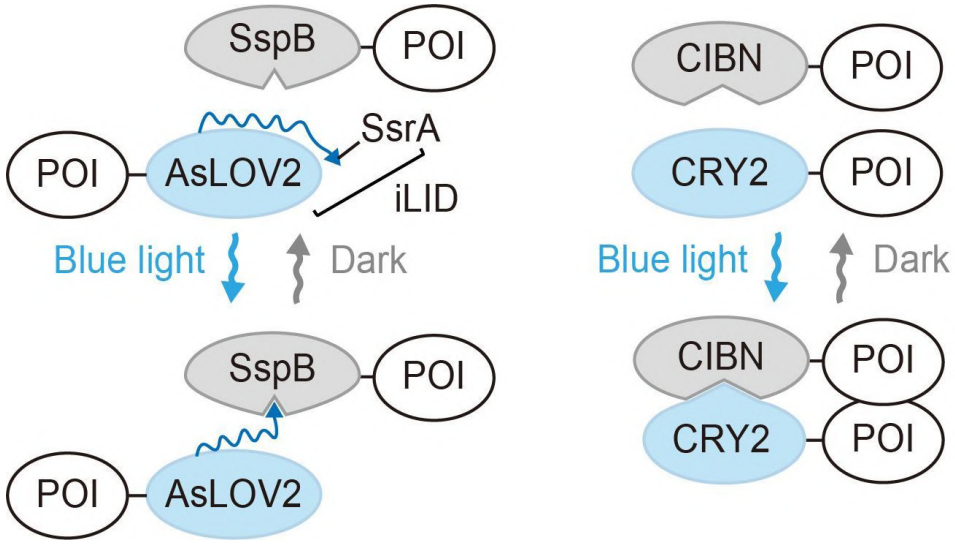

Figure 4. Light inducible dimerization (LID) system.
Schematic illustrations of iLID-SspB (left) and CRY2-CIB (right) systems. Blue light illumination induces structural changes of AsLOV2 and CRY2, leading to binding with SspB and CIBN, respectively. AsLOV2 and SsrA together are called iLID. The CRY2-CIB system often uses only the N-terminus region of the CIB1 (CIBN) that can bind to CRY2.

1.5. Purpose of this study

In this study, I develop a new optogenetic tool to directly inactivate NMII; the system, called OptoMYPT, is designed to recruit an endogenous catalytic subunit of type Ic phosphatase (PP1c) to the plasma membrane with light, thereby dephosphorylating and inactivating NMII. I demonstrate that MLCs are dephosphorylated and the traction force exerted by cells is reduced at the local area where a blue light is illuminated. In *Xenopus* embryos, OptoMYPT decreases the tension along the cell-cell junction, leading to deformation of the cell-cell junction. Moreover, this system is applied to the mechanics of cytokinesis to understand how and to what extent actomyosin-based cortical tension antagonizes contractile ring tension and contributes to the cleavage furrow ingression rate.

2. Materials and methods

2.1. Plasmids

The cDNAs of human MYPT1, PP1c, and Anillin were derived from HeLa cells (Human Science Research Resources Bank). The cDNA of human MLCK was the kind gift of Dr. Michiyuki Matsuda (Kyoto Univ.). The cDNA of iMyo was the kind gift of Dr. Hidehiko Hashimoto (Univ. Chicago). SspB-mScarlet-I-PP1BDs were obtained by Gibson assembly cloning, combining the SspB obtained from pLL7.0: tgRFPt-SSPB WT (plasmid #60415: Addgene) and cDNAs of PP1BDs. Stargazin-mEGFP-iLID was obtained by Gibson assembly cloning, combining the Stargazin derived from Stargazin-GFP-LOVpep (plasmid #80406: Addgene) and iLID derived from pLL7.0: Venus-iLID-CAAX (from KRas4B) (plasmid #60411: Addgene). CRY2 and CIBN-EGFP-KRasCT were obtained from pCX4puro-CRY2-CRaf and pCX4neo-CIBN-EGFP-KRasCT (Kazuhiro Aoki et al. 2013) and inserted into the pCAGGS vector (Niwa, Yamamura, and Miyazaki 1991). The cDNAs of Lifeact and NES were obtained by oligo DNA annealing and ligation, and inserted into each vector. The cDNA of hyPBase, an improved PiggyBac transposase (Yusa et al. 2011), was synthesized (FASMAC), and inserted into the pCAGGS vector. Tol2-based transposon donor vector (pT2A) and Tol2 transposase expression vector (pCAGGS-T2TP) were the kind gifts of Koichi Kawakami (National Institute of Genetics). The cDNA of Stargazin-mEGFP-iLID was inserted into the pT2Apuro vector (pT2Apuro-Stargazin-mEGFP-iLID). The cDNAs of rtTA (Roney et al. 2016) synthesized by FASMAC, tet-response element, and SspB-mScarlet-I-MYPT169 were inserted into a PiggyBac donor vector with ligation and Gibson assembly to generate pPBbsr2-rtTA2-TRE-SspB-mScarlet-I-MYPT169. For *in vitro* mRNA synthesis, these cDNAs were subcloned into the pCSf107mT vector. The nucleotide sequences of newly generated constructs are provided in Table 1.

Plasmid name	Relevant features	Figures	Source or reference	Sequence
pCAGGS-SspB-mScarlet-I	CAG promoter, SspB-mScarlet-I	8a,e, 9a, 15a, 25, 26a	This study	https://benchling.com/s/seq-LizO8aJvYQvytA26tnvk
pCAGGS-SspB-mScarlet-I-MYPT38	CAG promoter, SspB-mScarlet-I-MYPT38-NES	8a,e, 9a	This study	https://benchling.com/s/seq-e5c4XNGJU7VUDY1Adw0D
pCAGGS-SspB-mScarlet-I-MYPT169	CAG promoter, SspB-mScarlet-I-MYPT169-NES	8a,e, 9a, 12c, 15b,e, 17, 19, 25, 28a, 31a	This study	https://benchling.com/s/seq-VFtIByTEhOa69PaBJ7FF
pCAGGS-SspB-mScarlet-I-MYPT296	CAG promoter, SspB-mScarlet-I-MYPT296-NES	8a,e, 9a	This study	https://benchling.com/s/seq-NfHUqB2v72pMzw7Umbrv
pCAGGS-SspB-mScarlet-I-MYPT38 w/o NES	CAG promoter, SspB-mScarlet-I-MYPT38 (without NES)	8a	This study	https://benchling.com/s/seq-M5vohEavn7YouFTOsbqR
pCAGGS-SspB-mScarlet-I-MYPT169 w/o NES	CAG promoter, SspB-mScarlet-I-MYPT169 (without NES)	8a	This study	https://benchling.com/s/seq-4cIRYdnnkc5w1D7EG5pN
pCAGGS-SspB-mScarlet-I-MYPT296 w/o NES	CAG promoter, SspB-mScarlet-I-MYPT296 (without NES)	8a	This study	https://benchling.com/s/seq-ik7oQqR9I1hNqtdzAjGK
pCAGGS-Stargazin-mEGFP-iLID	CAG promoter, Stargazin-mEGFP-iLID	8e, 9a, 12c, 15a,b,e, 17, 19, 25, 26a, 28a, 31a	This study	https://benchling.com/s/seq-XUhPNN7CavWnbGAq1TUe
pCAGGS-PP1c-miRFP703	CAG promoter, PP1c-miRFP703	9a	This study	https://benchling.com/s/seq-8370yYN7igj1pyuf3TeZ
pCAGGS-CRY2-mCherry	CAG promoter, CRY2-mCherry	10b, 13b	This study	https://benchling.com/s/seq-bhM5JFtyaGL3itlXyRYw
pCAGGS-CRY2-mCherry-MYPT38	CAG promoter, CRY2-mCherry-MYPT38-NES	10b	This study	https://benchling.com/s/seq-tLDYRgH228MpcEprZ8H3
pCAGGS-CRY2-mCherry-MYPT169	CAG promoter, CRY2-mCherry-MYPT169-NES	10b, 13b, 18	This study	https://benchling.com/s/seq-jlDVZxO6I2j5bRqXLNAe
pCAGGS-CRY2-mCherry-MYPT296	CAG promoter, CRY2-mCherry-MYPT296-NES	10b	This study	https://benchling.com/s/seq-KgPOub2LM388hRapg

				VNp
pCAGGS-CIBN-EGFP-KRasCT	CAG promoter, CIBN-terminus-EGFP-KRasCT	10b, 13b, 18	This study	https://benchling.com/s/seq-RA16GvytRbNXBNzKX1hg
pPBbsr2-Lifeact-miRFP703	PiggyBac transposase donor vector, Lifeact-miRFP703	8a, 15a,b,e, 17, 18, 23b	This study	https://benchling.com/s/seq-6Umf325oqmk6HOmbykIX
pPBpuro-SspB-mCherry	PiggyBac transposase donor vector, SspB-mCherry	11, 12a	This study	https://benchling.com/s/seq-5d7Oj31YcZlxJqSsnNAa
pPBpuro-SspB-mCherry-MYPT38	PiggyBac transposase donor vector, SspB-mCherry-MYPT38-NES	11, 12a	This study	https://benchling.com/s/seq-fZysCS2LhI69PbhGD4tg
pPBpuro-SspB-mCherry-MYPT169	PiggyBac transposase donor vector, SspB-mCherry-MYPT169-NES	11, 12a,c	This study	https://benchling.com/s/seq-RrmRNQx2r9ULkAGO3yxd
pPBpuro-SspB-mCherry-MYPT296	PiggyBac transposase donor vector, SspB-mCherry-MYPT296-NES	11, 12a	This study	https://benchling.com/s/seq-WFNiQng3AysDppDUz4fk
pPBbsr2-Stargazin-mEGFP-iLID	PiggyBac transposase donor vector, Stagazin-mEGFP-iLID	11, 12a,c	This study	https://benchling.com/s/seq-iKCLTeMJ2f84JqYhfn1n
pPBbsr2-rtTA2-TRE-SspB-mScarlet-I-MYPT169	PiggyBac transposase donor vector, Doxycycline inducible expression, SspB-mScarlet-I-MYPT169	14a, 16	This study	https://benchling.com/s/seq-xf8zdl8VLNsyQHRmCXqC
pT2Apuro-Stargazin-mEGFP-iLID	Stargazin-mEGFP-iLID	14a, 16	This study	https://benchling.com/s/seq-rBh93iqQQT5hBXFNIIVG
pCAGGS-T2TP	CAG promoter, Tol2 transposase	14a, 16	This study	https://benchling.com/s/seq-yGo10mX966NnMTfpmt3F
pCAGGS-hyPBase	CAG promoter, PiggyBac transposase	8a, 11, 12a, 14a, 15a,b,e, 16, 17, 18, 23b	This study	https://benchling.com/s/seq-oGkw53b41IZqvzF5yQ9K
pCSf107mT-Lifeact-miRFP703	mRNA synthesis vector for *Xenopus*, Lifeact-miRFP703	20a, 21b	This study	https://benchling.com/s/seq-vtY7pCfmSVMpUQZXF5Us

pCSf107mT-SspB-mScarlet-I	mRNA synthesis vector for *Xenopus*, SspB-mScarlet-I	20a, 22a	This study	https://benchling.com/s/seq-NMiukyuyg4J64MgeMSrG
pCSf107mT-SspB-mScarlet-I-MYPT169	mRNA synthesis vector for *Xenopus*, SspB-mScarlet-I-MYPT169	20a, 21b, 22a	This study	https://benchling.com/s/seq-j1NmidSuKAuAX6LzGTy6
pCSf107mT-Stargazin-mEGFP-iLID	mRNA synthesis vector for *Xenopus*, Stargazin-mEGFP-iLID	20a, 21b, 22a	This study	https://benchling.com/s/seq-town7d8HHoJTrkapTNKX
pCSf107mT-mEGFP-KRasCT	mRNA synthesis vector for *Xenopus*, mEGFP-KRasCT	22a	This study	https://benchling.com/s/seq-0kClMWXvr2A6LllNkxtP
pCAGGS-CIBN-EGFP-MYPT170-296	CAG promoter, CIBN-EGFP-MYPT170-296	23b	This study	https://benchling.com/s/seq-0bg76IL3utQZ4EaCvPHI?m=slm-SKKgTRWdpgJMe18Mo2sg
pCAGGS-CIBN-EGFP-MYPT170-374	CAG promoter, CIBN-EGFP-MYPT170-374	23b	This study	https://benchling.com/s/seq-NNU40DgyA7tNp0FRA1wt?m=slm-JoyrRdyP1I3LbbJ3kAcK
pCAGGS-CIBN-EGFP-Anillin	CAG promoter, CIBN-EGFP-Anillin	23b	This study	https://benchling.com/s/seq-O5fKcMKjCLXmG79lFnG2?m=slm-KzwGyTM4Yt19j0fspbN4
pPBbsr2-telokin-mEGFP-iLID	CAG promoter, telokin-mEGFP-iLID	23b	This study	https://benchling.com/s/seq-1o7XgMoxVjICE3ne6q9K?m=slm-rVYVQsRyPi7TtVzZiRZl
pCAGGS-iMyo-mEGFP-iLID	CAG promoter, iMyo-mEGFP-iLID	23b	This study	https://benchling.com/s/seq-6BcJpyTG1tVlIJIlsZpW?m=slm-m9skqXLuRKf52w7gNMDv
pPBbsr2-Lifeact-mEGFP-iLID	PiggyBac transposase donor vector, Lifeact-mEGFP-iLID	23b	This study	https://benchling.com/s/seq-2z0IVCc36lbZhE09vrf4?m=slm-BNrHo1rr07SUVia7Jm5u

Table 1. Plasmids used in this study.

2.2. Cell culture

MDCK cells (no. RCB0995: RIKEN Bioresource Center) were maintained in minimal essential medium (MEM; 10370-021: ThermoFisher Scientific) supplemented with 10% fetal bovine serum (FBS; 172012-500ML: Sigma), 1x Glutamax (35050-061: ThermoFisher), and 1 mM sodium pyruvate (11360070: ThermoFisher) in a 5% CO_2 humidified incubator at 37 °C. NIH-3T3 cells (no. RCB0150: RIKEN Bioresource Center), a kind gift from Jun-ichi Nakayama (National Institute for Basic Biology), were maintained in DMEM (Nacalai Tesque) supplemented with 10% FBS in a 5% CO_2 humidified incubator at 37 °C. When splitting the MDCK cells, the growth media was removed, and 3 mL PBS/1 mM EDTA solution was added to the cells and incubated for 5 min at 37 °C. Next, the PBS/1 mM EDTA solution was discarded, and 2 mL PBS/1 mM EDTA/0.25% Trypsin was added. The cells were incubated for 5 min at 37 °C. Prewarmed growth medium was added to resuspend the cells. When splitting the NIH-3T3 cells, the first treatment with 3 mL PBS/1 mM EDTA solution was omitted.

2.3. Transfection

Because PP1BDs of MYPT1 fused with fluorescent proteins tend to aggregate for long-term expression, most experiments were performed by transient expression. The MDCK cells and NIH-3T3 cells were electroporated by using Nucleofector IIb (Lonza) according to the manufacturers' instructions (T-023 program) with a house-made DNA- and cell-suspension solution (4 mM KCl, 10 mM $MgCl_2$, 107 mM Na_2HPO_4, 13 mM NaH_2PO_4, 11 mM HEPES pH. 7.75). For transient expression, the plasmids were mixed according to the following ratios to achieve efficient membrane translocation by light: SspB:iLID = 1:4; and CRY2:CIB = 1:3. After electroporation, the cells were plated on 35-mm culture dishes or collagen-coated 35-mm glass-bottom dishes.

2.4. Establishment of stable cell lines

For transposon-mediated gene transfer, MDCK cells were transfected with PiggyBac or Tol2 donor vectors and PiggyBac or Tol2 transposase-expressing vectors at a ratio of 3:1. One day after transfections, cells were treated with 10 μg/mL blasticidin S (InvivoGen, San Diego, CA) or 1.0 μg/mL puromycin (InvivoGen) for selection. The bright bulk cell population was collected using a cell sorter (MA900; SONY).

2.5. Live-cell fluorescence imaging

Cells were imaged with an IX83 inverted microscope (Olympus, Tokyo) equipped with an sCMOS camera (Prime: Photometrics, Tucson, AZ; or ORCA-Fusion BT: Hamamatsu Photonics, Hamamatsu, Japan), a spinning disk confocal unit (CSU-W1; Yokogawa Electric Corporation, Tokyo), and diode lasers at wavelengths of 488 nm, 561 nm, and 640 nm. An oil immersion objective lens (UPLXAPO60XO, N.A. 1.42; UPLXAPO 40X, N.A. 1.4; Olympus), an air/dry objective lens (UPLXAPO40X, N.A. 0.95; UPLXAPO 20X, N.A. 0.8; Olympus) were used. The excitation laser and fluorescence filter settings were as follows: Excitation laser, 488 nm (mEGFP), 561 nm (mScarlet-I), and 640 nm (miRFP703); dichroic mirror, DM 405/488/561 dichroic mirror (mEGFP, mScarlet-I, and miRFP703); emission filters, 500–550 nm (mEGFP), 580–654 nm (mScarlet-I), and 665–705 nm (miRFP703). During observation, cells were incubated with a stage incubator set to 37 °C and containing 5% CO_2 (STXG-IX3WX; Tokai Hit).

Due to the different kinetics depending on the optogenetic systems, the cells expressing iLID-SspB or CRY2-CIB system were illuminated with blue light for 500 msec less than every 20 sec for iLID-SspB system and less than every 2 min intervals for CRY2-CIB. For global illumination of the blue light, blue LED light (450 nm) (LED-41VIS450;

OptoCode Corp., Japan) was continuously illuminated from the top of the stage or pulsed blue light (488 nm) was illuminated through the objective lens. For local light illumination in the interphase cells, a digital micromirror device (Polygon 400; Mightex) mounted on the IX83 microscopic system, and pT-100 (CoolLED) were used. For local light illumination during cytokinesis, an SP8 FALCON inverted confocal laser scanning microscope (Leica) equipped with a water immersion objective lens (HC PL APO 63x/1.20 W motCORR; Leica) was used. Local light illumination was started using the FRAP function just after chromosome segregation onset. I illuminated every 3.11 sec, and acquired images every 15.54 sec. The positions of regions of interest (ROIs) were manually corrected every 2 min in all samples.

For all time-lapse imaging, MDCK cells were plated on 35 mm glass-bottom dishes (IWAKI) or 4-well glass-bottom dishes (The Greiner Bio-One). Before time-lapse imaging, the medium was replaced with FluoroBrite (Invitrogen) supplemented with 10% FBS, 1x Glutamax.

2.6. Immunofluorescence

Cells were fixed with 3.7% formaldehyde in PBS for 20 min, followed by permeabilization by 5 min incubation in 0.05% Triton X-100-containing PBS. Samples were soaked for 30 min in Can Get Signal immunostain (solution A) (Toyobo, Japan) and then incubated with primary antibodies, phospho-MLC antibody (1:50 dilution; Cell Signaling Technology #3674), or PPP1CB antibody (1:200 dilution; abcam #ab53315) diluted in Can Get Signal immunostain (solution A) for 1 h at room temperature. Next, the cells were washed 3 times with PBS, and then incubated for 1 h at room temperature with Alexa 633-conjugated anti-rabbit IgG (1:1000 dilution; ThermoFisher) in Can Get Signal immunostain (solution A). Finally, the cells were washed 3 times with PBS and subjected to fluorescence imaging.

In Figure 13, the cells expressing control proteins or OptoMYPT were seeded on the 4-well glass-bottom dish 2 h before light illumination. Lamellipodial regions of the cells were locally illuminated with blue light for 30 min under the microscope, and then fixed with 3.7% formaldehyde in PBS on the stage of the microscope. Subsequent immunostaining steps were also performed on the stage of the microscope. For one experiment, the locations of 10 sites per well where the cells expressed control and OptoMYPT proteins were recorded, and fluorescence images were acquired at the same positions after staining.

2.7. Traction force microscopy

Polyacrylamide gel substrates were prepared according to previously published protocols (Tambe et al., 2011; Trepat et al., 2009). In brief, the gel solution was prepared with 4% acrylamide, 0.1% bisacrylamide, 0.8% ammonium persulfate, 0.08% TEMED (Nacalai Tesque), and 5% deep red fluorescent carboxylate-modified beads (0.2 μm diameter; F8810; Thermo Fisher Scientific). 13 μL of the mixture was added to a 35 mm glass-bottom dish (IWAKI) and then covered with a glass coverslip of 15 mm diameter (Matsunami). After gel polymerization at room temperature, the surface was coated with 0.3 mg/mL type I collagen (Nitta Gelatin, Osaka, Japan) using 4 mM sulphosuccinimidyl-6-(4-azido-2-nitrophenylamino) hexanoate (Sulfo-SANPAH; Pierce). Cells were seeded on the gel, and imaged with a spinning disk confocal microscope. To quantify the traction force, two Fiji plugins, *i.e.*, the iterative PIV and FTTC plugins, were used. Note that Young's modulus of the gel was estimated as ~2 kPa according to a previous report (Tse and Engler 2010). The traction force in locally illuminated areas was used for the quantification.

2.8. Western blotting

Cells were lysed in 1x SDS sample buffer. After sonication for 5 min, the samples were boiled at 95 °C for 5 min. Then, the samples were separated by 5–20% gradient SDS-polyacrylamide gel electrophoresis (Nacalai Tesque) and transferred to polyvinylidene difluoride membranes (Millipore). After blocking with Odyssey Blocking Buffer-TBS (LICOR Biosciences) for 1 h, the membranes were incubated with primary antibodies overnight at 4 °C, followed by the secondary antibodies for 1 h at room temperature. For primary antibodies, phospho-MLC antibody (1:500 dilution; Cell Signaling Technology #3674), phospho-Ezrin/Radixin/Moesin antibody (1:500 dilution; Cell Signaling Technology #3276), MYPT1 antibody (1:500 dilution; Cell Signaling Technology #2634) and α-Tubulin antibody (DM1A) (1:5000 dilution; sc-32293: Santa Cruz Biotechnology) were diluted in Odyssey Blocking Buffer-TBS. For secondary antibodies, IRDye680LT-conjugated goat polyclonal anti-rabbit IgG (H + L) (1:5000 dilution; LI-COR Bioscience) and IRDye800CW-conjugated donkey polyclonal anti-mouse IgG (H + L) (1:5000 dilution; LI-COR Bioscience) were diluted in Odyssey Blocking Buffer-TBS. Proteins were detected with an Odyssey infrared scanner (LI-COR Bioscience).

2.9. *Xenopus* embryo manipulation and microinjection

All experiments using *Xenopus laevis* were approved by The Institutional Animal Care and Use Committee, National Institutes of Natural Sciences. Manipulation of *X. laevis* embryos and microinjection experiments were carried out according to standard methods as follows. Unfertilized eggs were obtained from female frogs injected with gonadotropin (ASKA Animal Health, Japan) and artificially fertilized with testis homogenate. Fertilized eggs were dejellied with 4% L-cysteine solution (pH adjusted to 7.8 with NaOH) and incubated in 1/10x Steinberg's solution at 14 °C or 17 °C. pCSf107mT, which contains 4 x SP6/T7 transcription

terminator sequences, was used to prepare plasmid constructs for mRNA synthesis (Mii and Taira 2009). Synthetic mRNAs were transcribed from plasmid DNAs using an mMessage mMachine SP6 kit (Invitrogen). Each four-cell stage embryo was microinjected with 50 pg of SspB-mScarlet-I or SspB-mScarlet-I-MYPT169 mRNA; 450 pg of Stargazin-mEGFP-iLID or mEGFP-KRasCT mRNA; and 150 pg of Lifeact-miRFP703 mRNA. Gastrula embryos (st. 12) were observed directly using the IX83 inverted microscope (see "Live-cell fluorescence imaging"). An oil immersion objective lens (UPLXAPO 40X, N.A. 1.4; Olympus) was used for three-dimensional imaging. The vitelline membrane was manually removed before imaging to clearly visualize the cell-cell junctions. For optogenetic experiments, blue light was illuminated from the objective lens for 500 msec every 20 sec.

2.10. Laser ablation

Laser ablation was conducted as described previously (Hara et al. 2013), using an IX81 inverted microscope (Olympus) equipped with a spinning disk confocal unit (CSU-X1; Yokogawa Electric Corporation) and iXon3 897 EM-CCD camera (Andor), and controlled with IQ2 software (Andor). A dry objective lens (UPlanAPO 20X, N.A. 0.7; Olympus) was used. An N2 Micropoint laser (16 Hz, 365 nm, 0.3 μW; Photonic Instruments) was focused on the plasma membrane at a cell-cell junction labeled with Stargazin-mEGFP-iLID or mEGFP-KRasCT. Time lapse images were acquired every 3.08 sec before and after the course of the laser ablation. Before ablation, the embryos in the incubator were illuminated from overhead by blue light for 20 min. The vitelline membrane was manually removed before imaging to clearly visualize the cell-cell junctions.

2.11. Imaging analysis

All fluorescence imaging data were analyzed and quantified by Fiji (Image J). For all images, the background was subtracted and images were registered by StackReg, a Fiji plugin to correct misregistration, if needed. To quantify the cytoplasmic fluorescence intensity changes in Figure 9, the ROI was selected in each image and normalized by the mean fluorescence intensity of the first 10 images under dark conditions. In Figure 13, to quantify the fluorescence intensity ratio of the light area to dark area, I used the cytoplasmic or lamellipodial region, avoiding extremely bright regions such as stress fibers. To quantify the area of membrane protrusion in Figure 15, the ROI was chosen so as to coincide with the local light-irradiated area. In OptoMYPT-dark cells, the ROI was a region of lamellipodia similar to that of light-illuminated cells. Fluorescence images of Lifeact-miRFP703 were binarized and the difference between the area at each time point and at t = 0 was calculated.

2.12. Statistics and reproducibility

In all box-and-whisker plots, the box shows the quartiles of data with the whiskers denoting the minimum and maximum except for the outliers detected by 1.5 times the interquartile range. All statistical analyses were conducted in Microsoft Excel software (ver. 16.54) for two-tailed student's t-test (Figs. 14b, 20f, 22d, e, 26b, 27b) or python (ver. 3.7) with scipy (ver. 1.4.1) (scipy.stats.brunnermunzel) for two-tailed Brunner-Munzel test (Fig. 13). The experiments were repeated at least two times independently with similar results. The number of samples for quantifications is listed in the figure legends.

3. Chapter I: Development of a new optogenetic tool to reduce the intracellular contractile force

3.1. Introduction

Optogenetic tools to control intracellular contractile force

In order to control actomyosin contractility using optogenetics, the most popular approach is to control the activity of RhoA, a member of Rho family small GTPases. Light-induced recruitment of RhoGEF to the plasma membrane triggers RhoA activation, which in turn activates ROCK and inactivates MLCP (Wagner and Glotzer 2016; Kimura et al. 1996; Valon et al. 2017) (Fig. 2). These reactions eventually induce myosin light chain phosphorylation, followed by an increase in the actomyosin contractility. It has been reported that local accumulation of RhoGEF by light increases contractile force at the subcellular scale (Wagner and Glotzer 2016; Oakes et al. 2017; Valon et al. 2017). These technologies allow activation of NMII at the equator and the induction of partial constriction in rounded cells in metaphase (Wagner and Glotzer 2016). Valon *et al*. further demonstrated that trapping of overexpressed RhoGEF to the outer membrane of mitochondria resulted in a decrease in actomyosin contractility (Valon et al. 2017). In addition, depletion of $PI(4,5)P_2$ at the plasma membrane by optogenetic membrane translocation of 5-phosphatase OCRL has been shown to modulate cell contractility and inhibit apical constriction during *Drosophila* embryogenesis (Guglielmi et al. 2015). Although many of these tools enhance actomyosin contractility through RhoA or phospholipids, tools that reduce actomyosin contractility below the basal level have not yet been developed.

3.2. Results

3.2.1. Design of the OptoMYPT system.

To manipulate the intracellular contractile force, I focused on MLCP, which is composed of three subunits, a catalytic subunit (PP1c), a regulatory subunit (MYPT1), and a smaller subunit of 20-kDa (M20) (Ito et al. 2004). MYPT1 contains a PP1c-binding domain (PP1BD) and myosin heavy chain (MHC)-binding domain (Fig. 5). MYPT1 holds PP1c through the PP1BD, and recruits it to NMII to dephosphorylate MLC, leading to the inactivation of NMII (Fig. 6). Phosphorylated MLC is mainly localized near the plasma membrane such as at cortical actin and stress fibers, where the NMII exerts mechanical force (Du and Frohman 2009).

The strategy to reduce actomyosin-based contractile force is based on inducing membrane translocation of the PP1BD in MYPT1 with light, resulting in the co-recruitment of endogenous PP1c at the plasma membrane and dephosphorylation of MLC. I refer to this system as the OptoMYPT system. It has been reported that the 1 to 38 amino acids (a.a.) in the PP1BD are particularly important for binding to PP1c, and that the 170 to 296 a.a. in the PP1BD serve as a phosphorylated MLC-binding domain (Hirano, Phan, and Hartshorne 1997) (Fig. 5). Moreover, the seven ankyrin repeats existing in the 39 to 296 a.a. in the PP1BD are responsible for increasing the binding ability of PP1c (Tanaka et al. 1998) (Fig. 5). Therefore, in this study, I examined three different lengths of PP1BDs: 1-38, 1-169, and 1-296. As an optogenetic switch, I mainly employed the iLID-SspB system; iLID protein binds to its binding partner, SspB, upon blue light illumination and dissociates from SspB under the dark condition (Guntas et al. 2015). The iLID-based OptoMYPT system consists of a light-switchable plasma membrane localizer, Stargazin-mEGFP-iLID, and an actuator, SspB-mScarlet-I-PP1BD, which is translocated to the plasma membrane for the co-recruitment of the endogenous PP1c with blue light (Fig. 7). The Stargazin-mEGFP-iLID is

suited for the subcellular protein recruitment, because the large N-terminal transmembrane anchor limits the diffusion of SspB proteins (Natwick and Collins 2021). Alternatively, I developed a CRY2-based OptoMYPT system, in which CRY2-mCherry-PP1BD was recruited to the plasma membrane with blue light through binding to the plasma membrane localizer CIBN-EGFP-KRasCT (Kennedy et al. 2010).

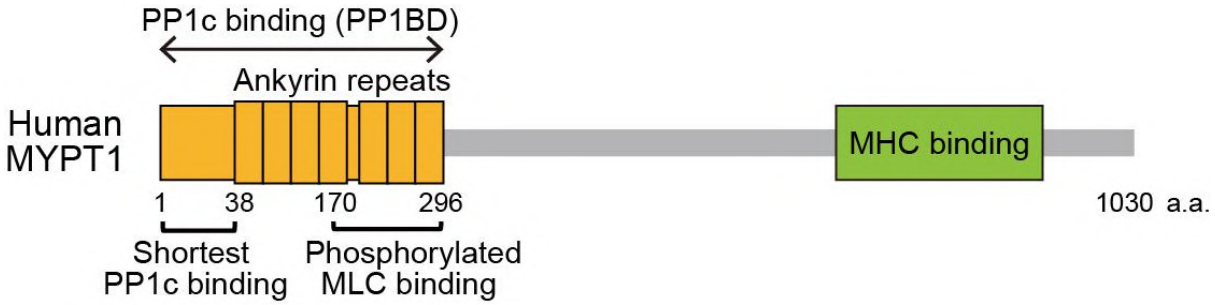

Figure 5. Domain structure of human MYPT1.
MYPT1 contains the PP1c binding domain in its N-terminus region (orange box). The 1 to 38 a.a. in PP1BD are particularly important for the PP1c binding. The 170 to 296 a.a. in the PP1BD serve as a phosphorylated MLC-binding domain. The seven ankyrin repeats existing in the 39 to 296 a.a. in the PP1BD are responsible for increasing the binding ability of PP1c. MYPT1 contains MHC binding domain to recruit PP1c to the phosphorylated sites (green box).

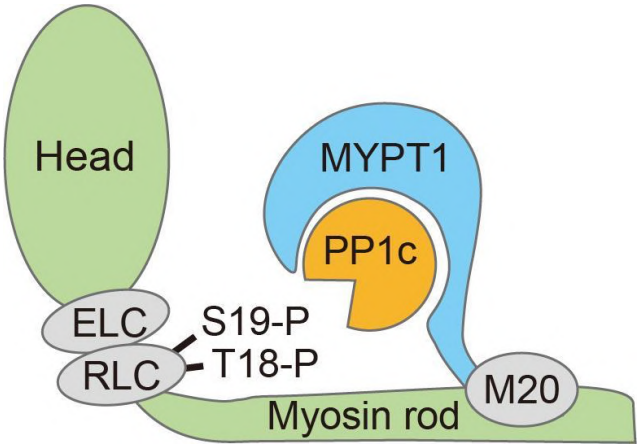

Figure 6. Dephosphorylation of MLC by MLCP complex.
Schematic illustration of the MLCP complex binding to NMII. MLCP complex is composed of MYPT1, PP1c, and M20. MYPT1 recruits PP1c to the phosphorylated MLC sites through its MHC binding domain and PP1c binding domain.

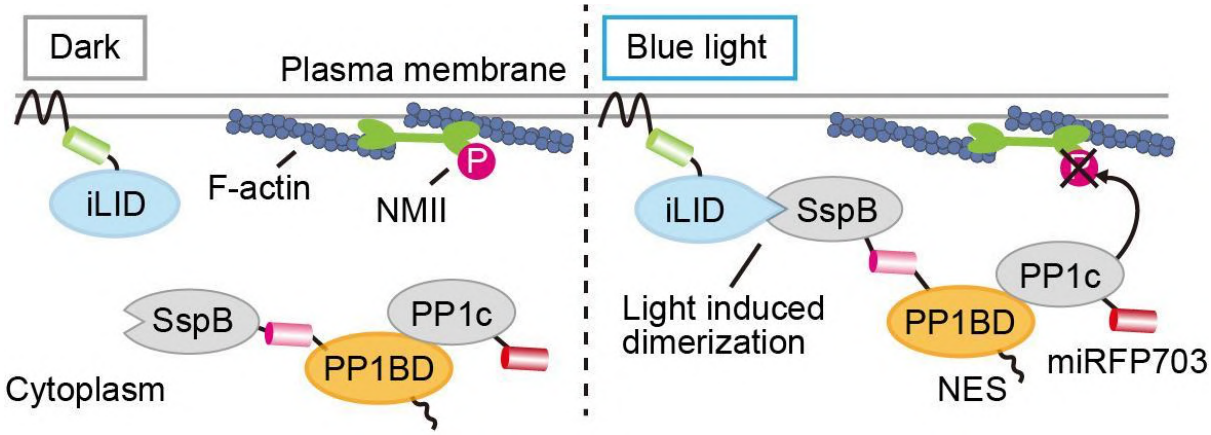

Figure 7. Design of the OptoMYPT system.
Schematic illustration of the OptoMYPT system. Stargazin-mEGFP-iLID is anchored to the plasma membrane. Upon blue light illumination, the SspB-mScarlet-I-fused PP1c-binding domain (PP1BD) of MYPT1 translocates to the plasma membrane along with endogenous PP1c, and inactivates NMII at the cell cortex.

3.2.2. Light inducible membrane translocation of PP1BD and PP1c.

I first compared the efficiency of light-induced membrane translocation between three different lengths of PP1BDs: 1-38, 1-169, and 1-296 (hereafter referred to as MYPT38, MYPT169, and MYPT296, respectively). In line with the previous study (Wu et al. 2005), SspB-mScarlet-I-PP1BDs accumulated at the nucleus (Fig. 8a, b). To circumvent this problem, the nuclear export signal (NES) was fused with the C terminus of the PP1BDs to export them to the cytoplasm (Fig. 8a, b). We confirmed that Madin-Darby Canine Kidney (MDCK) cells exhibited the translocation of SspB-mScarlet-I from the cytoplasm to the plasma membrane upon blue light illumination as a control (Fig. 9a, b). SspB-mScarlet-I-MYPT169 showed the best membrane translocation in three differential lengths of PP1BDs (Fig. 9a, b). I recognized that a small fraction of SspB-mScarlet-I-MYPT38 still resided in the nucleus (Fig. 9a, yellow arrowhead), and CRY2-mCherry-MYPT38 formed aggregates and puncta in a blue light-dependent manner for an unknown reason (Fig. 10).

Next, I investigated whether PP1BDs of MYPT1 indeed bind to PP1c and recruit it to the plasma membrane. In control cells, PP1c fused with miRFP703 (PP1c-miRFP703), which was mainly localized at the nucleus, did not show any change in the subcellular localization upon blue light illumination (Fig. 9a, c). As expected, SspB-mScarlet-I-MYPT38, -MYPT169, and -MYPT296 demonstrated similar levels of translocation of PP1c-miRFP703 from the cytoplasm to the plasma membrane upon blue light illumination (Fig. 9a, c). I also confirmed the plasma membrane translocation of the endogenous PP1c by immunofluorescence analysis (Fig. 11). During these experiments, I noticed that the cells expressing MYPT296 showed elongated membrane protrusions even under the dark condition (Fig. 8a), which was similar to the morphology of cells treated with ROCK inhibitor or myosin inhibitor (Worthylake and Burridge 2003; Totsukawa et al. 2004), while the cell size was not substantially different between cells expressing PP1BDs of MYPT (Fig.

8c). I evaluated the effect of the expression of PP1BDs on basal phosphorylation of MLC by western blotting analysis. The expression levels of SspB-mScarlet-I-MYPT169 were estimated relative to that of the endogenous MYPT, showing an approximately 12-fold increase in stable expression and 50-fold increase in transient expression under our experimental conditions (Fig. 12). As expected from the cell morphology, MLCs were dephosphorylated in MDCK cells stably expressing MYPT296 (Fig. 8d). This result is consistent with the previous report pointing out the existence of the phosphorylated MLC-binding domain at the 170–296 a.a. (Hirano, Phan, and Hartshorne 1997), which may facilitate recruitment of PP1BD to NMII and dephosphorylation of MLC without blue light stimulation. The ERM family of plasma membrane-actin cytoskeleton cross-linking proteins, which are known to be the substrates of PP1c, maintained their phosphorylation levels detected with pan-phospho-ERM antibody (Fig. 8d), suggesting that the expression of PP1BD of MYPT has no impact on phosphorylation of the ERM proteins under these conditions. Taken together, these results led me to conclude that MYPT169 is well suited for the OptoMYPT system.

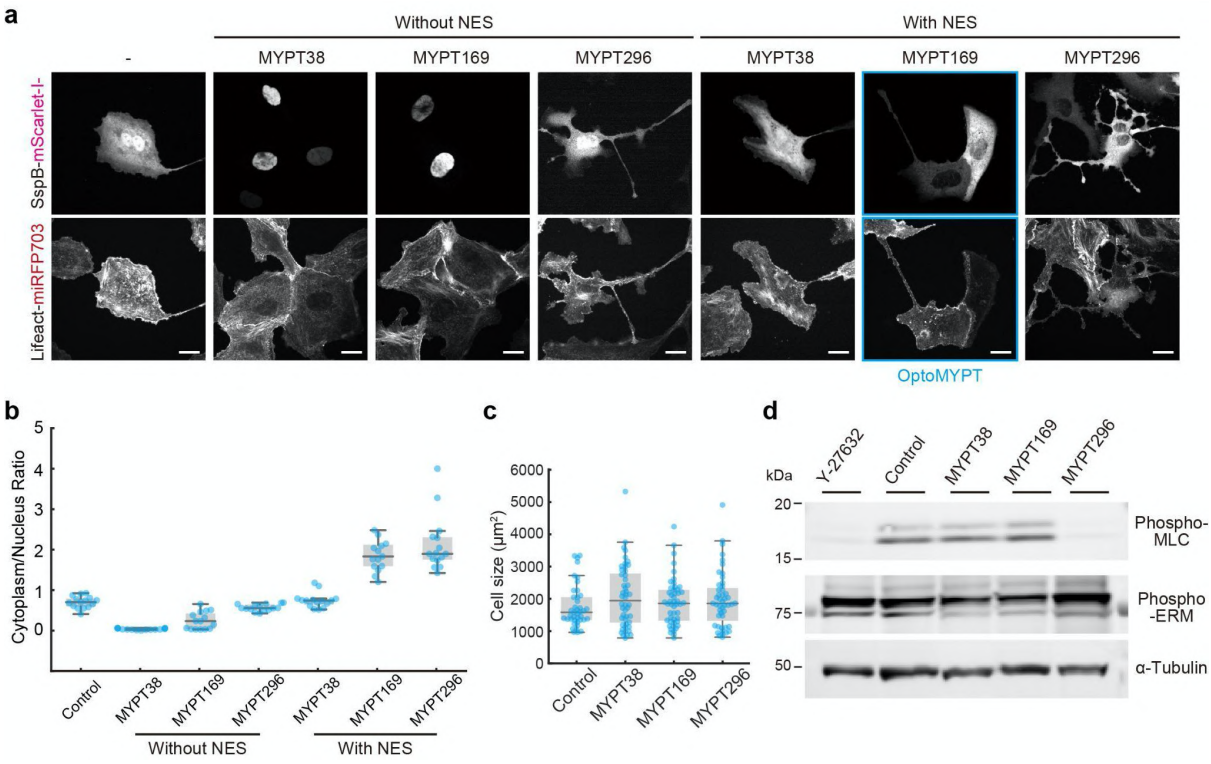

Figure 8. Optimization of the length of PP1BD for OptoMYPT.
(a) Representative images of MDCK cells transiently expressing SspB-mScarlet-I or SspB-mScarlet-I-PP1BDs without or with NES (upper panels), transiently expressing Stargazin-mEGFP-iLID, and stably expressing Lifeact-miRFP703 (lower panels). SspB-mScarlet-I-MYPT169-NES was used for the OptoMYPT (panels outlined in blue). Of note, SspB-mScarlet-I-MYPT296-expressing cells showed aberrant morphology with elongated protrusions. Scale bar, 20 μm. (b) The ratio of cytoplasmic to nuclear fluorescence intensity of SspB-mScarlet-I-MYPTs was quantified in each cell, and shown as a box plot, in which the box extends from the first to the third quartile with the whiskers denoting 1.5 times the interquartile range. A blue dot indicates data from individual cells. n = 14–15 cells. (c) The cell size of MDCK cells transiently expressing SspB-mScarlet-I or SspB-mScarlet-I-PP1BDs with NES was quantified, and shown as a box plot as in panel b. n = 41, 48, 48, and 47 for cells expressing plasmids of Control, MYPT38, MYPT169, MYPT296, respectively. (d) Western blot analysis of phospho-MLC, phospho-ERM, and α-Tubulin in MDCK cells stably expressing SspB-mScarlet-I (Control) or SspB-mScarlet-I-PP1BDs with NES, and Stargazin-mEGFP-iLID. Control cells were treated with 40 μM Y-27632 as a negative control (Y-27632).

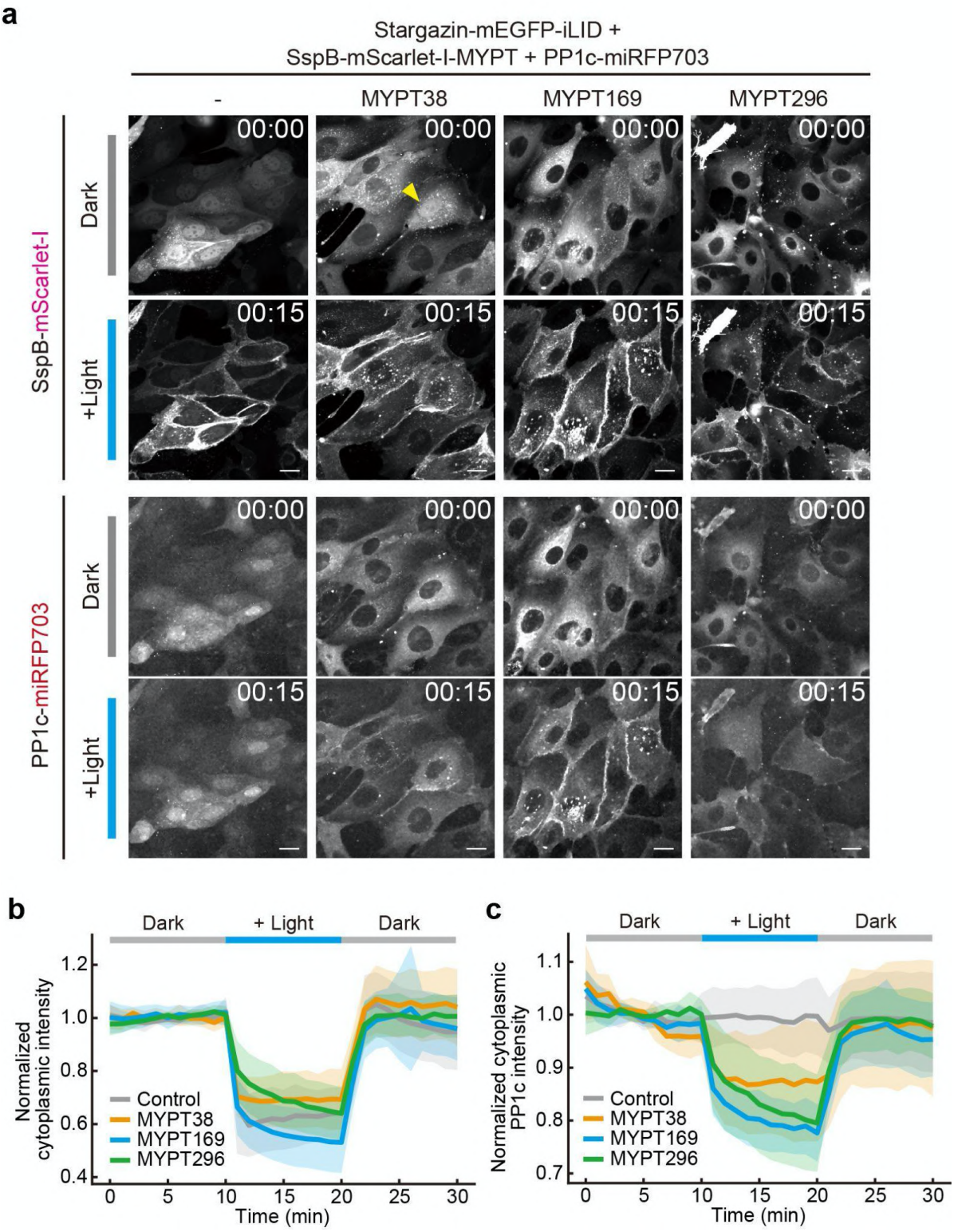

Figure 9. Membrane translocation of the PP1BD in MYPT1 and PP1c with blue-light. (a) Representative images of the SspB-mScarlet-I or the indicated SspB-mScarlet-I-PP1BDs of MYPT1 (upper two rows) and simultaneously expressing PP1c-miRFP703 (lower two rows) in MDCK cells under the dark condition (the first and third rows) and blue light condition (the second and fourth rows). Stargazin-mEGFP-iLID was also expressed as a localizer in all experiments. The yellow arrowhead indicates a cell showing nuclear

accumulation of SspB-mScarlet-I-MYPT38. Blue light was continuously illuminated from the top of the stage. Scale bar, 20 μm. (b) Quantification of the cytoplasmic fluorescence change in mScarlet-I in panel d. The average values (bold lines) are plotted as a function of time with the SD. n = 15 cells. (c) Quantification of the cytoplasmic fluorescence change in PP1c-miRFP703 in the indicated MDCK cells. The average values (bold lines) are plotted as a function of time with the SD. n = 15 cells.

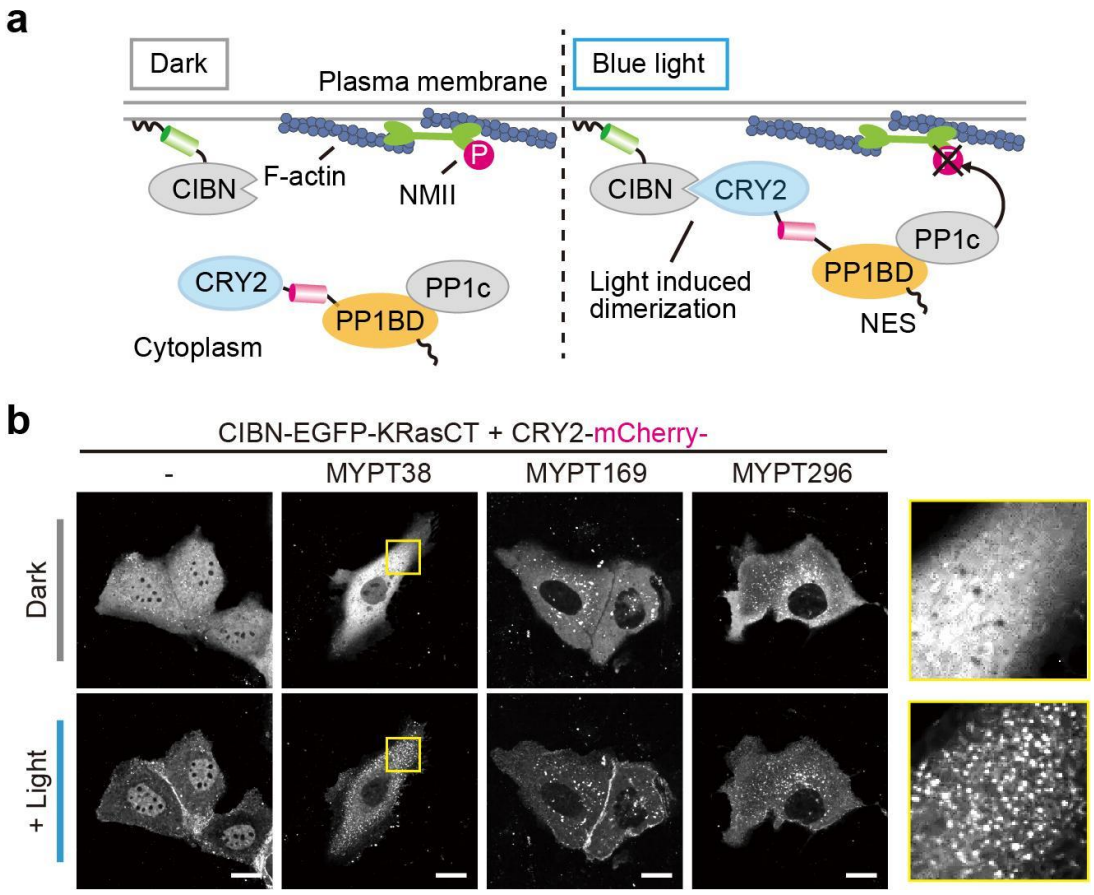

Figure 10. CRY2-based OptoMYPT system.
(a) Schematics of the CRY2-based OptoMYPT system. (b) Representative images of MDCK cells transiently expressing CRY2-mCherry or CRY2-mCherry-PP1BDs with NES, and CIBN-EGFP-KRasCT. The cells expressing CRY2-mCherry-MYPT38 showed aggregates and puncta upon blue light illumination (yellow boxed region). Blue light was illuminated through the objective lens for 500 msec every 1 min. Scale bar, 20 μm.

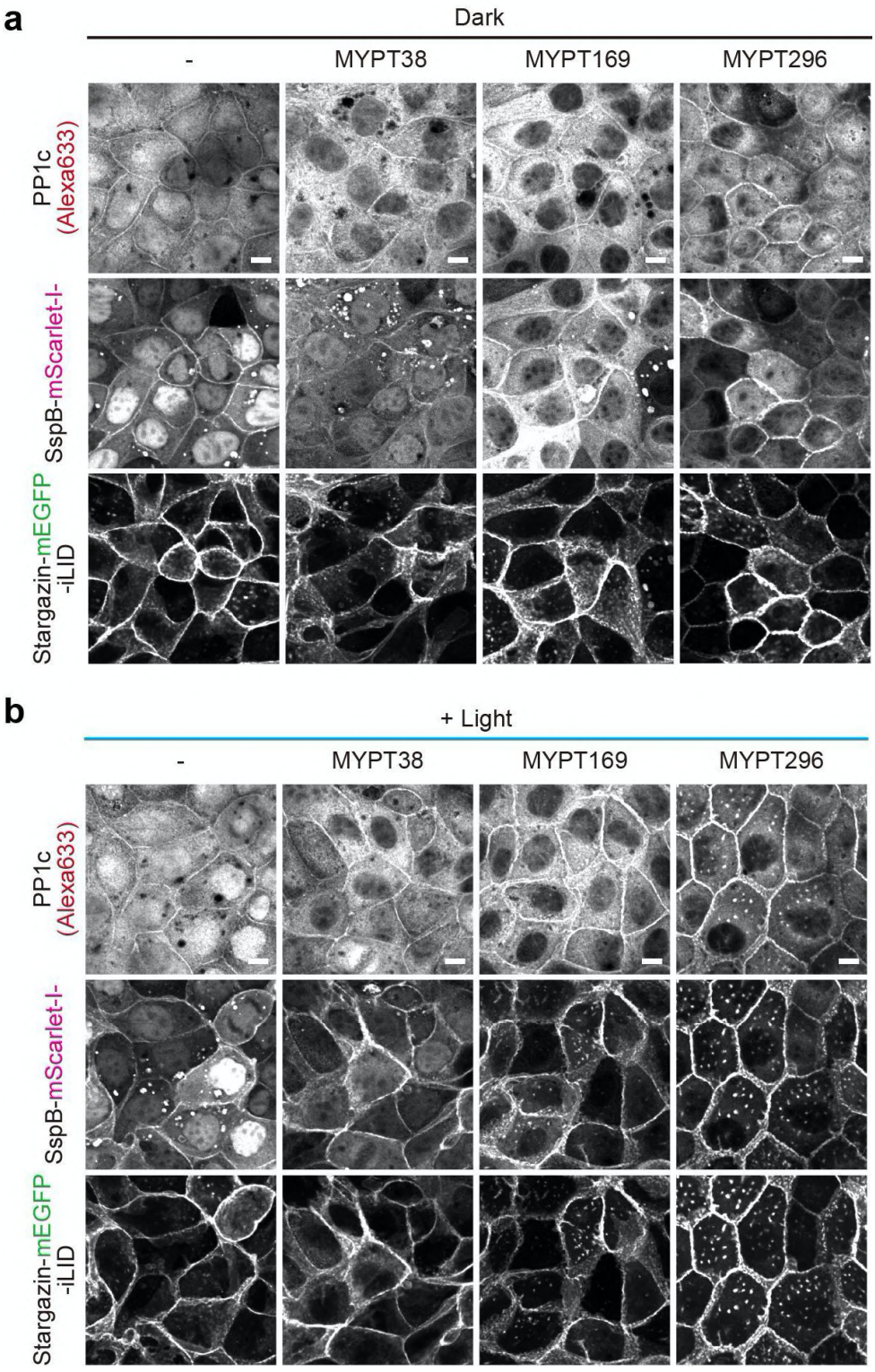

Figure 11. Immunofluorescence analysis of endogenous PP1c.
(a, b) Immunofluorescence of the endogenous PP1c in MDCK cells stably expressing SspB-mScarlet-I-PP1BDs with NES, and Stargazin-mEGFP-iLID in dark conditions (a) and light-illuminated conditions (b). Blue light was illuminated from the top of the culture dishes for 3 min before fixation. Scale bar, 20 μm.

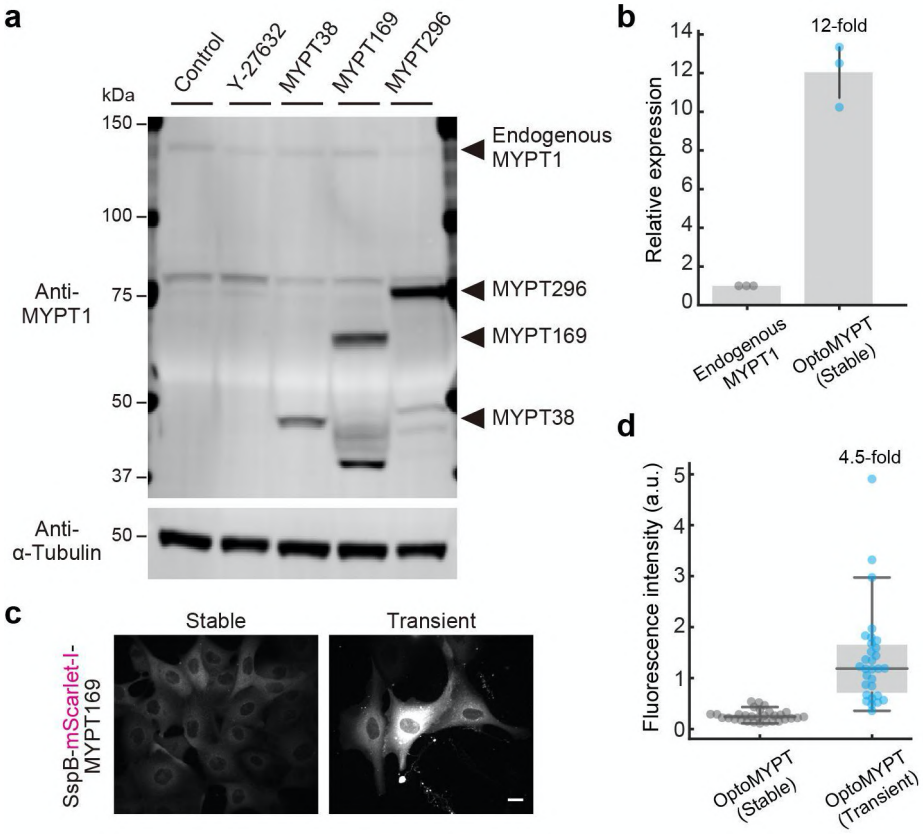

Figure 12. Quantification of the expression level of OptoMYPT relative to endogenous MYPT1.

(a) Western blot analysis of MYPT1 and α-Tubulin in MDCK cells stably expressing SspB-mScarlet-I (Control) or SspB-mScarlet-I-PP1BDs with NES, and Stargazin-mEGFP-iLID. Control cells were treated with 40 μM Y-27632 as a negative control (Y-27632). Note that the MYPT1 antibody recognizes the N-terminus of the MYPT1. (b) Quantification of the relative expression level of SspB-mScarlet-I-MYPT169 to endogenous MYPT1. A total of n = 3 experiments were performed. (c) The representative images of SspB-mScarlet-I-MYPT169 in stably and transiently expressing MDCK cells. (d) The expression levels of SspB-mScarlet-I-MYPT169 in stably and transiently expressing MDCK cells are represented as a box plot, in which the box extends from the first to the third quartile with the whiskers denoting 1.5 times the interquartile range. Each gray and blue dot indicates data from individual cells. n = 30 cells for each condition.

3.2.3 Light-induced dephosphorylation of MLC by OptoMYPT.

To evaluate whether the OptoMYPT dephosphorylates MLC in a blue light-dependent manner, I directly measured phosphorylated MLC with immunofluorescence. Given the design of OptoMYPT, we expected that the OptoMYPT dephosphorylates MLCs that are located beneath the plasma membrane upon light stimulation. Therefore, I focused on lamellipodia, in which a sheet-like thin structure with an actin meshwork propels the cell membrane in a myosin IIA-dependent manner (Even-Ram et al. 2007; Miguel Vicente-Manzanares et al. 2008; Kuragano, Murakami, and Takahashi 2018). The blue light was locally illuminated at the lamellipodia in MDCK cells for 30 min, followed by fixation and immunofluorescence staining with the anti-phospho-MLC antibody (Fig. 13a). I herein adopted a CRY2-based OptoMYPT system (Kennedy et al. 2010), because the slower dissociation kinetics of the CRY2-CIB system compared to that of the iLID-SspB system was preferable for this experiment. Local illumination of blue light induced spatially restricted recruitment of CRY2-mCherry and CRY2-mCherry-MYPT169 (Fig. 13b, left column). In addition, the local recruitment of CRY2-mCherry-MYPT169, but not CRY2-mCherry, attenuated the MLC phosphorylation (Fig. 13b, right column). The quantification of phosphorylated MLC fluorescence intensity in dark and light illuminated areas (Fig. 13a) revealed a partial but significant reduction in the phosphorylated MLC level (Fig. 13c). I further evaluated the dephosphorylation of MLC by biochemical studies. To this end, I established a doxycycline-inducible expression system of OptoMYPT proteins, because PP1BDs of MYPT tended to form aggregates by long term expression. I found that the global blue light illumination partially decreased the phosphorylated MLC level, based on western blotting analysis in MDCK cells expressing OptoMYPT proteins (Fig. 14). This partial reduction of MLC phosphorylation by OptoMYPT was probably due to the limited accessibility of PP1BD of MYPT to MLCs; OptoMYPT could reach MLCs that were located

beneath the plasma membrane, such as lamellipodia, but not at the sites far from the plasma membrane. Note that just OptoMYPT expression induced a slight decrease in phosphorylated MLC levels even before blue light irradiation (Fig. 14), implying that PP1c is partially activated by overexpression of MYPT169 with the doxycycline-inducible expression system. Taken together, these results indicate that the OptoMYPT system dephosphorylates MLCs located beneath the plasma membrane by light stimulation.

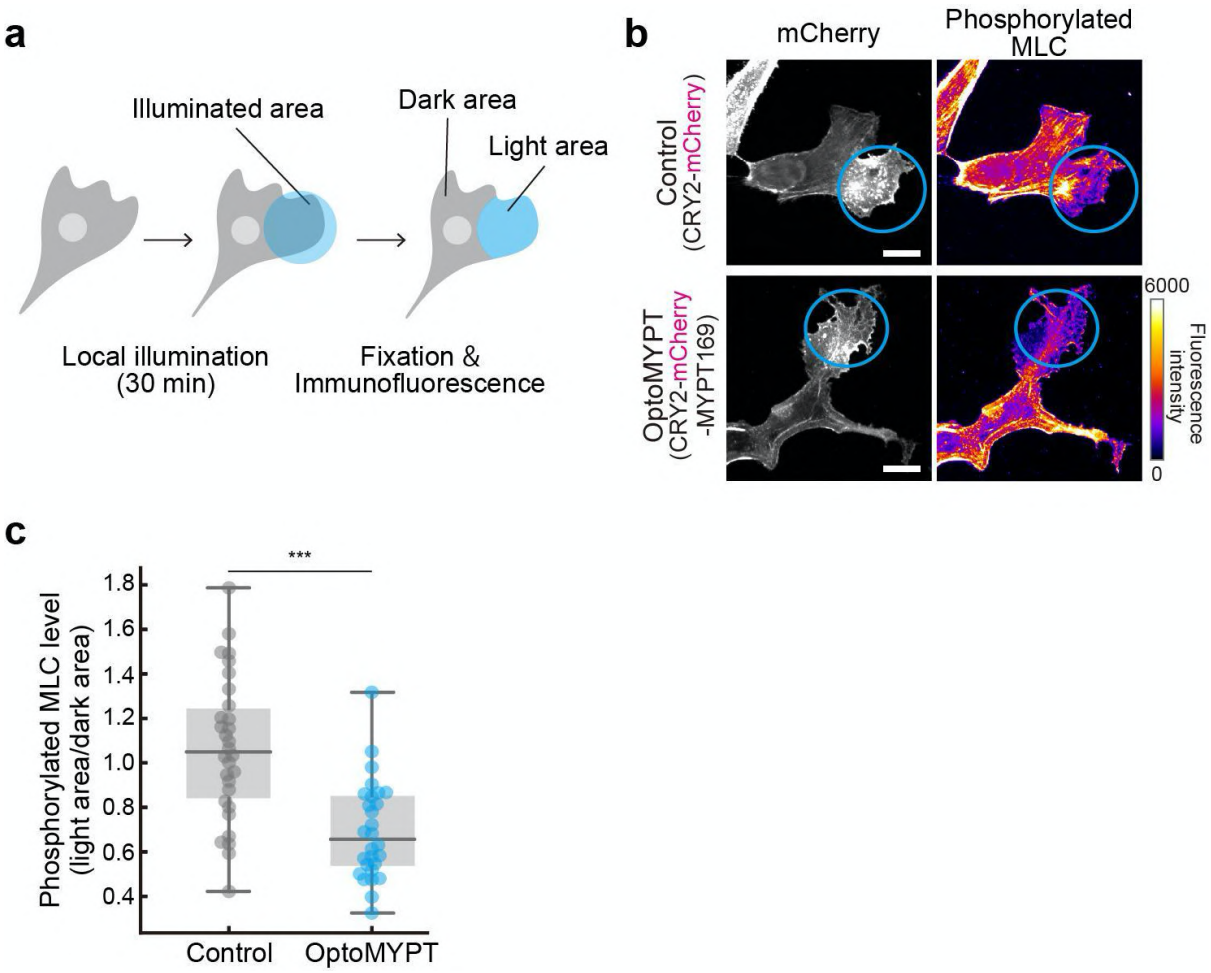

Figure 13. OptoMYPT-induced dephosphorylation of MLC with immunofluorescence analysis.

(a) Schematic illustration of an experimental procedure to quantify phosphorylated MLC levels. The blue light was locally focused on the lamellipodial area in each cell, followed by fixation and immunostaining. (b) Immunofluorescence analysis of MLC phosphorylation after local blue-light illumination. The upper and lower images show MDCK cells expressing CRY2-mCherry and CRY2-mCherry-MYPT169, respectively. CIBN-EGFP-KRasCT was also expressed as a localizer in both experiments. The blue circular region was locally illuminated with 500 msec of blue light at 2 min intervals for 30 min. Scale bar, 10 μm. (c) The phosphorylated MLC level was quantified by dividing the mean fluorescence intensity of the light area by that of the dark area in panel a, and shown as a box plot, in which the box extends from the first to the third quartile with the whiskers denoting 1.5 times the interquartile range. n = 30 and 28 cells for the control and OptoMYPT, respectively. ***$p <$ 0.001 (Brunner-Munzel test) (Brunner and Munzel 2000).

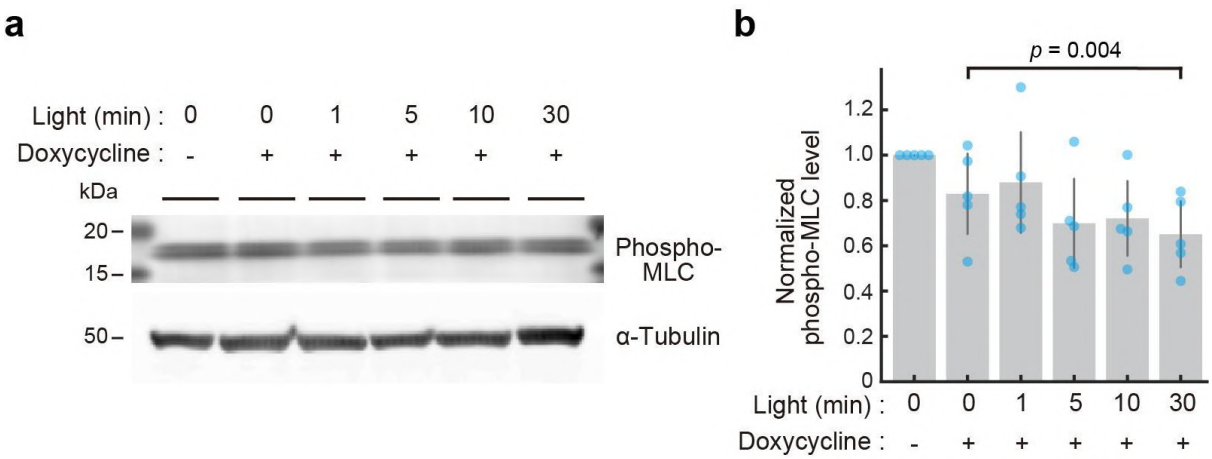

Figure 14. OptoMYPT-induced dephosphorylation of MLC with western blot analysis. (a) Western blot analysis of phosphorylated MLC and α-Tubulin in MDCK cells. In this cell line, Stargazin-mEGFP-iLID is constitutively expressed, whereas SspB-mScarlet-I-MYPT169 is expressed in a doxycycline-dependent manner (0.25 µg/mL doxycycline for one day). Blue light was globally and continuously illuminated from the top of the dish for the number of minutes indicated on the figure. (b) Quantification of phosphorylated MLC levels. α-Tubulin was used as loading control. n = 5 experiments. $p = 0.004$ (Paired *t*-test).

3.2.4. Light-induced membrane protrusions by OptoMYPT.

The depletion of myosin IIA, blebbistatin treatment, or overexpression of the non-phosphorylatable form of MLC has been shown to result in membrane protrusion (Even-Ram et al. 2007; Miguel Vicente-Manzanares et al. 2008; Burnette et al. 2011; Kuragano, Murakami, and Takahashi 2018). These reports prompted us to examine whether dephosphorylation of MLC by OptoMYPT would induce membrane protrusion. The control MDCK cells that expressed SspB-mScarlet-I, Stargazin-mEGFP-iLID, and Lifeact-miRFP703 demonstrated local accumulation of SspB-mScarlet-I by blue light illumination, but did not show the morphological change (Fig. 15a). On the other hand, the OptoMYPT-expressing MDCK cells reproducibly showed peripheral membrane protrusions in the blue-light exposed area (Fig. 15b). I evaluated light-induced membrane protrusion with a kymograph and time-course graph, which showed the movement of the cell edge upon blue light illumination in OptoMYPT-expressing cells (Fig. 15c). The protruding membrane was subsequently maintained under dark conditions (Fig. 15c). Interestingly, I often recognized membrane retraction on the opposite side of the blue-light illumination area (Fig. 15e, yellow arrowhead). This data suggests that the decrease of the concentration of PP1c in the non-illuminated area activates actomyosin. Furthermore, the global, blue-light illumination of MDCK cells expressing OptoMYPT induced membrane protrusions mainly from lamellipodial regions (Fig. 16). Similarly, in NIH-3T3 cells, the local illumination of blue light induced membrane protrusions from the pre-existing lamellipodia (Fig. 17a, b, inset 1), but did not induce the change in stress fiber formation and membrane protrusions from the site in close proximity to stress fibers (Fig. 17a, b, inset 2). This result suggests that MLCs on stress fibers probably escape the dephosphorylation by OptoMYPT because they are far from the plasma membrane. Finally, I tested whether the CRY2-based OptoMYPT system induces the same protrusions as the iLID-based one. In an actively migrating MDCK cell, I repeatedly

induced membrane protrusions in the light-illuminated area (Fig. 18). Taken together, I concluded that the OptoMYPT system induces membrane protrusions from the lamellipodial region due to the dephosphorylation of MLCs.

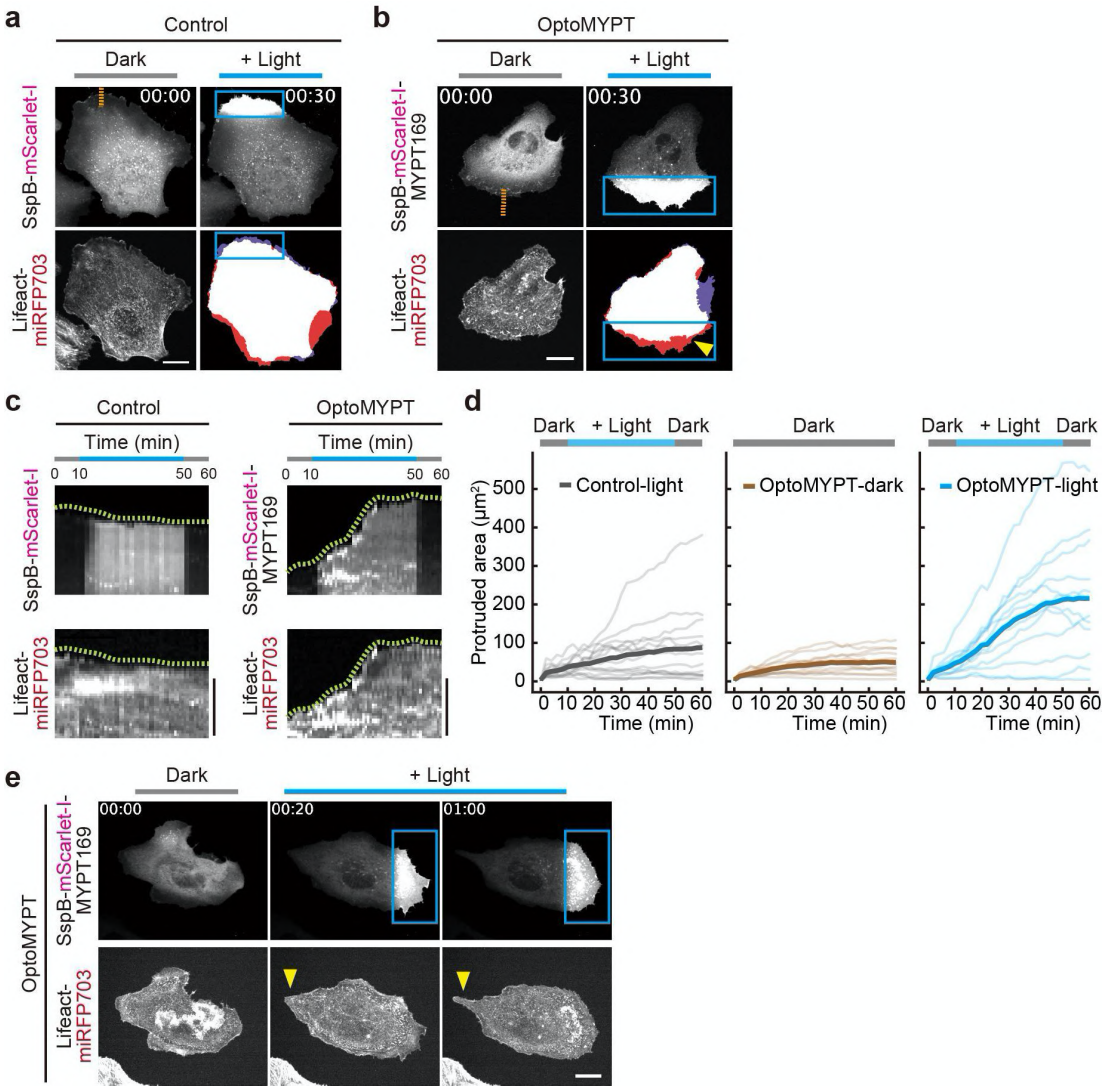

Figure 15. OptoMYPT-induced membrane protrusions by local illumination.
(a, b) Simultaneous visualization of SspB-mScarlet-I (a) or SspB-mScarlet-I-MYPT169 (b) with F-actin (Lifeact-miRFP703) in MDCK cells. The blue rectangular regions were locally illuminated with 500 msec blue light every 20 sec. The right bottom image shows a binary image reconstructed from Lifeact-miRFP703 images; red and purple areas represent protruding and retracting areas, respectively. The yellow arrowheads depict membrane protrusion. Scale bar, 20 μm. (c) Kymographs were drawn along the orange dashed lines in panels a and b. Green dashed lines show cell boundaries. Scale bar, 5 μm. (d) Quantification of the local protruding areas under the indicated conditions. The total protruded area was calculated by subtracting the cell area in the locally illuminated region at t = 0 from that at each time point. Local blue light was illuminated from 10 to 50 min. The thin and bold lines indicate the individual and averaged data, respectively. n = 15, 13, and 12 cells for Control-light (local blue light illumination), OptoMYPT-dark (dark condition), OptoMYPT-light (local blue light illumination), respectively. (e) Representative images of the induction of membrane retraction (yellow arrowhead) on the opposite side of the blue-light illuminated area. The blue rectangular regions were locally illuminated with 500 msec blue light every 20 sec. Scale bar, 20 μm.

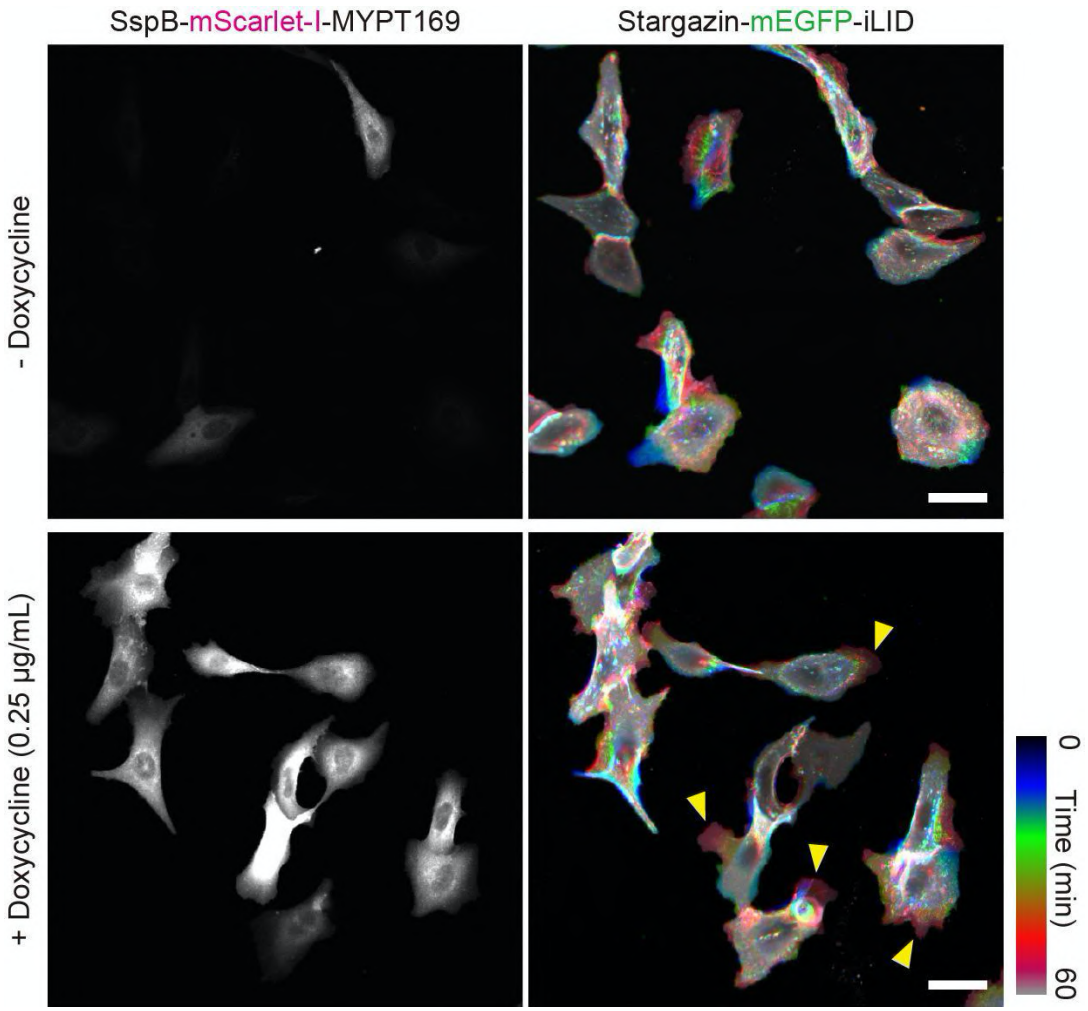

Figure 16. OptoMYPT-induced membrane protrusions by global illumination. Simultaneous visualization of SspB-mScarlet-I-MYPT169 with Stargazin-mEGFP-iLID in MDCK cells. In this cell line, Stargazin-mEGFP-iLID is constitutively expressed, whereas SspB-mScarlet-I-MYPT169 is transiently expressed by a doxycycline-inducible promoter (0.25 µg/mL doxycycline for one day). Blue light was globally and continuously illuminated from the top of the dish just after imaging onset for 60 min. The upper and lower panels represent the cells without or with doxycycline induction, respectively. The left columns show the expression of SspB-mScarlet-I-MYPT169, indicating the induction of SspB-mScarlet-I-MYPT169 in a doxycycline-dependent manner. The right columns show the deformation of cell shape across 60 min of blue light illumination, with the time elapsed indicated by the color code on the right side. Yellow arrowheads indicate lamellipodial protrusion. Scale bar, 50 µm.

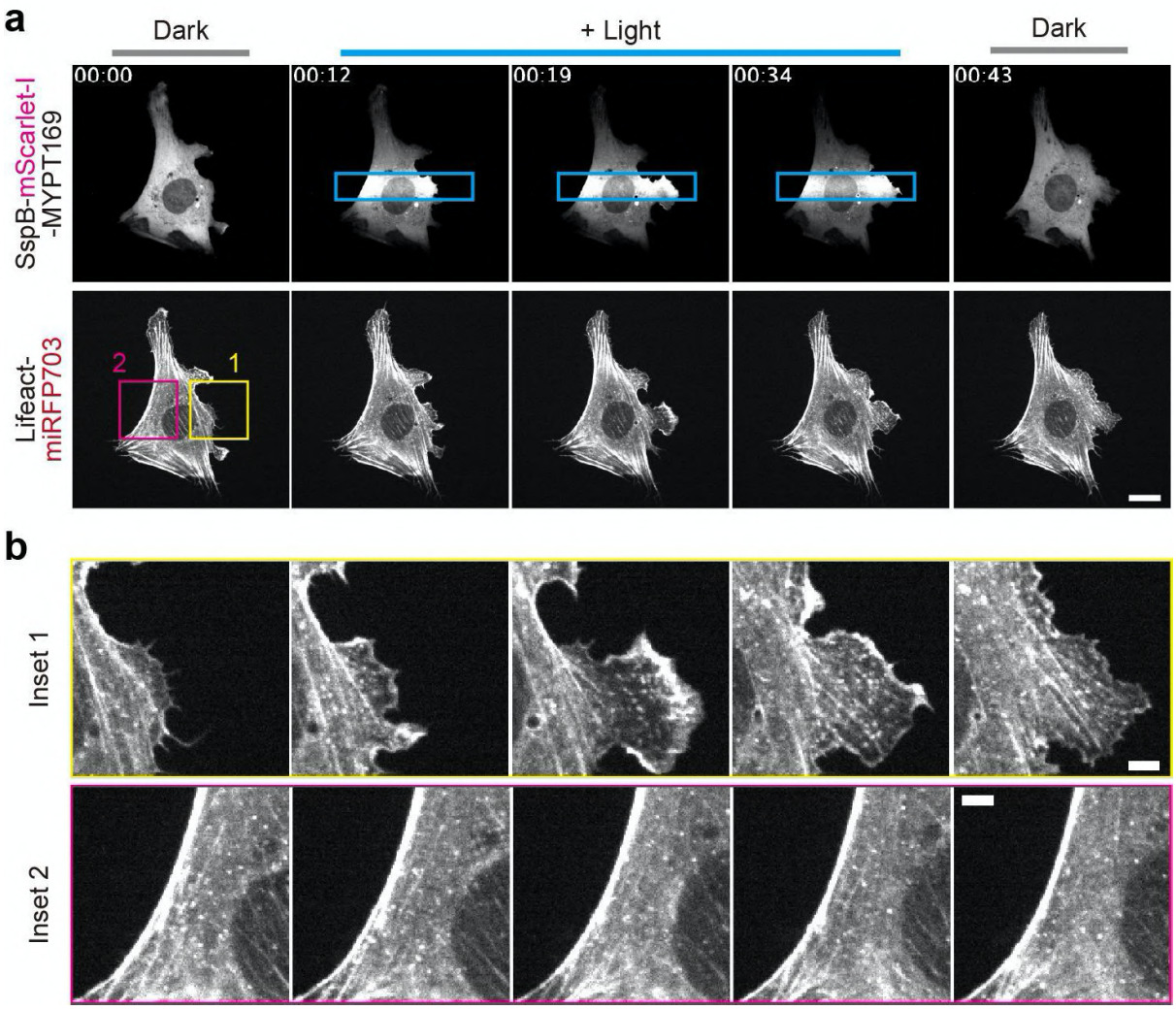

Figure 17. OptoMYPT-induced membrane protrusions in NIH-3T3 cells.
(a) Simultaneous visualization of SspB-mScarlet-I-MYPT169 (upper) with F-actin (Lifeact-miRFP703) (lower) in NIH-3T3 cells. The rectangular regions were illuminated with blue light for 500 msec every 20 sec. Blue rectangles indicate illuminated areas. Scale bar, 20 μm. (b) Inset images of Lifeact-miRFP703 in panel a. Scale bar, 5 μm.

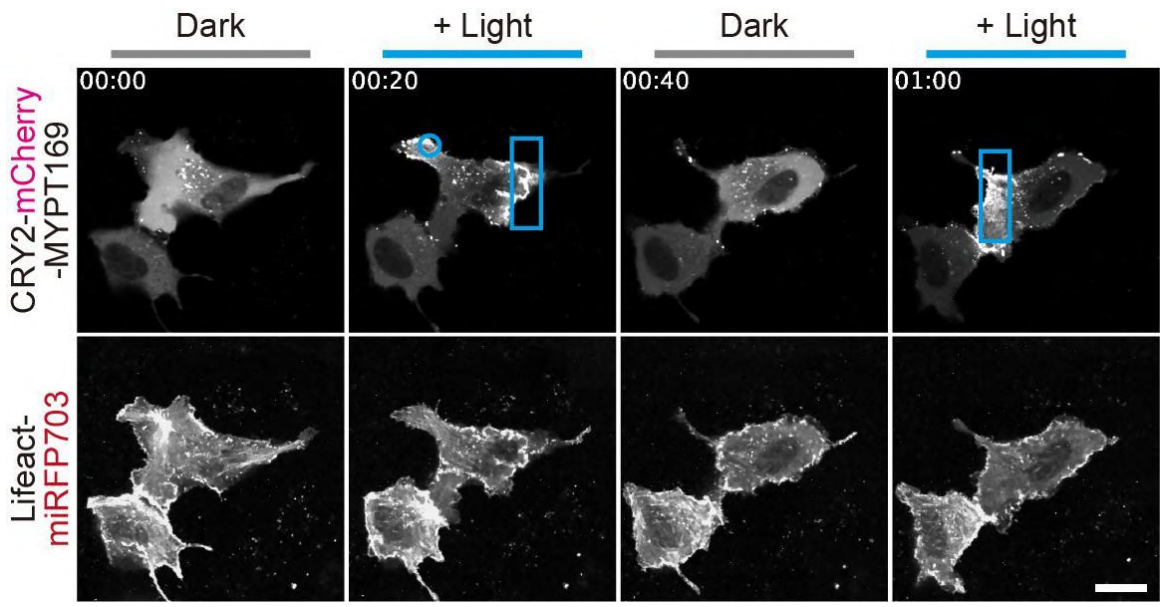

Figure 18. OptoMYPT-induced membrane protrusions based on CRY2-CIB system. Simultaneous visualization of CRY2-mCherry-MYPT169 (upper) with F-actin (Lifeact-miRFP703) (lower) in an MDCK cell. The rectangular and circular regions were illuminated with blue light for 500 msec every 1 min. Blue rectangles indicate illuminated areas. Scale bar, 20 μm.

3.2.5. OptoMYPT reduced the traction force in migrating cells.

Next, I examined whether the decrease in MLC phosphorylation by OptoMYPT affects actomyosin-based contractile force. To do this, I employed traction force microscopy, which is a method of estimating the force with which cells pull on a substrate. The cells were seeded on polyacrylamide gel containing fluorescence beads. Based on the movement of the beads and the stiffness of the gel, the traction force can be inferred (Fig. 19a). In order to simultaneously observe the membrane translocation of SspB-mScarlet-I or SspB-mScarlet-I-MYPT169 and the movement of the beads, infra-red beads were used. The blue light was locally focused on the lamellipodial region of randomly migrating MDCK cells, where the cells were generating strong traction force. SspB-mScarlet-I (control) and SspB-mScarlet-I-MYPT169 (OptoMYPT) were successfully recruited to the locally illuminated area (Fig. 19b, c). In contrast to the control cells, the cells expressing the OptoMYPT system showed a decrease in traction force after blue light illumination (Fig. 19d). These results indicate that the OptoMYPT system can dephosphorylate MLCs by local blue light illumination, leading to a reduction of traction force in randomly migrating cells.

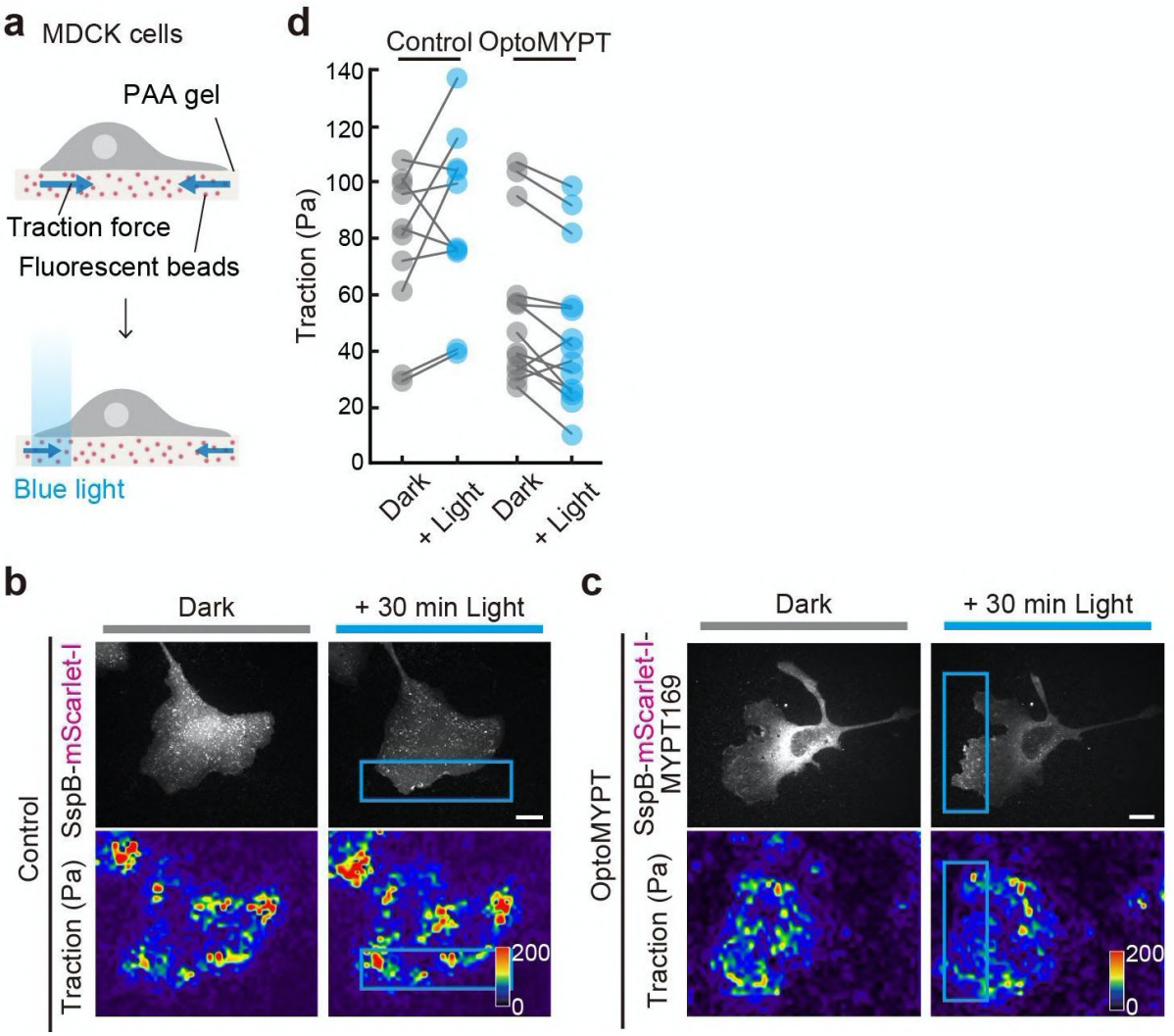

Figure 19. OptoMYPT reduced the traction force in migrating cells.
(a) Schematic illustration of the traction force microscopy. (b,c) Traction force measurement in an MDCK cell expressing SspB-mScarlet-I (b), and SspB-mScarlet-I-MYPT169 (c) with Stargazin-mEGFP-iLID. The blue rectangular regions were locally illuminated with 500 msec of blue light at 20 sec interval for 30 min. Traction force (Pa) is represented as a pseudo color. Scale bar, 20 μm. (d) Quantification of the traction force before and after blue-light illumination. n = 10 and 13 cells for Control and OptoMYPT cells, respectively.

3.2.6. OptoMYPT reduced the tension at the cell-cell junction in *Xenopus* embryos.

I further applied OptoMYPT to the *in vivo* system by using *Xenopus laevis* embryos. For this purpose, I observed the animal pole of stage 12 gastrula embryos, which generate relatively strong tension at the cell-cell junctions (Kinoshita et al. 2020). The embryos expressing SspB-mScarlet-I or SspB-mScarlet-I-MYPT169 together with Stargazin-mEGFP-iLID and Lifeact-miRFP703 demonstrated rapid plasma membrane translocation of SspB-mScarlet-I or SspB-mScarlet-I-MYPT169 in response to blue light illumination, respectively (Fig. 20a, upper panels). In embryos expressing OptoMYPT, the cell-cell junctions became wavy in shape by blue light illumination, suggesting decreased actomyosin contractility (Fig. 20a, lower panels, b) (Hara, Shagirov, and Toyama 2016; Hara 2017; Arnold et al. 2019). I quantified the temporal changes in waviness at the cell-cell junctions and found that waviness increased significantly in the cells expressing OptoMYPT constructs after blue light illumination (Fig. 20c-f).

Next, I investigated the recovery time of the wavy cell-cell junctions to return to its original state by long-term imaging (Fig. 21a). As in the previous results, SspB-mScarlet-I-MYPT169 rapidly translocated to the plasma membrane by blue light illumination, and the cell-cell junctions gradually changed to wavy shape (Fig. 21b). After turning off blue light, SspB-mScarlet-I-MYPT169 rapidly dissociated from the plasma membrane, while it took approximately 2 hours to recover the basal shape of the cell-cell junctions. Interestingly, I often found an accumulation of F-actin in the recovering wavy cell-cell junctions (Fig. 21b, yellow arrowheads). These F-actin accumulations gradually disappeared during the course of recovering wavy cell-cell junction. This result suggests that actin reorganization is abnormal in the wavy cell-cell junctions.

To directly validate the decrease in actomyosin contractility at the cell-cell junctions, I combined laser ablation with optogenetic experiments. This is because the tension along the

cell-cell junction can be estimated by measuring the recoil velocity of the cell-cell junction after laser ablation (Gómez-González et al. 2020; Iyer et al. 2019). For convenience, the ablation point was determined based on the membrane-targeted mEGFP signal at the cell-cell junctions. To prevent membrane translocation of SspB-mScarlet-I-MYPT169 by excitation light for mEGFP, mEGFP-KRasCT, which is a plasma membrane-localized protein incapable of recruiting SspB proteins, was co-expressed instead of Stargazin-mEGFP-iLID and was used as an "OptoMYPT-no translocation" control (Fig. 22a). In these experiments, the cells were 20 min pre-illuminated and then illuminated by the mEGFP excitation blue light for laser ablation experiments. To avoid potential contributions of the initial junction lengths to recoil, cell-cell junctions of similar lengths were selected for the laser ablation experiments (Fig. 22b). I tested the following three conditions; Control (SspB-mScarlet-I and Stargazin-mEGFP-iLID), OptoMYPT-no translocation (SspB-mScarlet-I-MYPT169 and mEGFP-KRasCT), and OptoMYPT (SspB-mScarlet-I-MYPT169 and Stargazin-mEGFP-iLID). The center of the cell-cell junctions was ablated, and the displacement was measured from the subsequent change in the distance between cell-cell junctions (Fig. 22c, d). The recoil velocity of the cell-cell boundary was significantly slower in OptoMYPT cells (0.81 ± 0.42 μm/min) than in Control cells (1.06 ± 0.38 μm/min) and OptoMYPT-no translocation cells (1.35 ± 0.50 μm/min) (Fig. 22e), indicating the reduced tension at the cell-cell junction by OptoMYPT. These results demonstrate that the OptoMYPT system is applicable *in vivo* and decreases actomyosin contractility in a multicellular context.

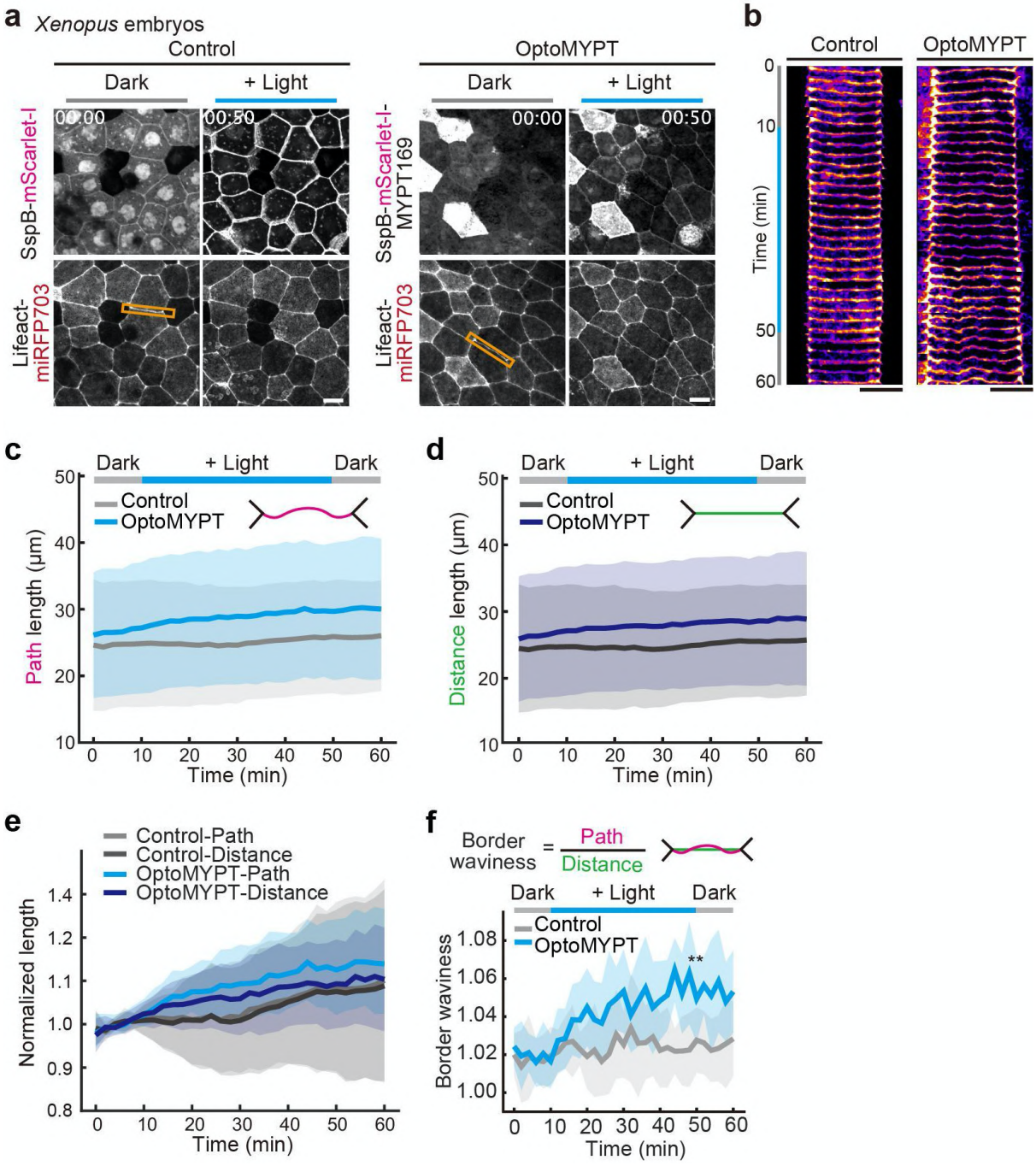

Figure 20. OptoMYPT induced wavy cell-cell junction in *Xenopus* embryos.
(a) Simultaneous visualization of SspB-mScarlet-I (left) or SspB-mScarlet-I-MYPT169 (right) with F-actin (Lifeact-miRFP703) in *Xenopus* embryos at gastrula stages. The mRNAs for SspB-mScarlet-I (left) or SspB-mScarlet-I-MYPT169 (right) with Stargazin-mEGFP-iLID and Lifeact-miRFP703 were injected into the animal pole region of a ventral blastomere at the four-cell stage. Cells were globally illuminated through the objective lens with 500 msec of blue light at 20 sec intervals. Scale bar, 20 μm. (b) Kymographs were drawn along the orange boxed areas in panels a. Scale bar, 20 μm. (c, d) The path length (c) and total distance (d) of cell-cell junctions were quantified in *Xenopus* embryos expressing SspB-mScarlet-I (Control) and SspB-mScarlet-I-MYPT169 (OptoMYPT) with Stargazin-mEGFP-iLID. The average of path length and total distance are plotted as a function of time with SD.

Results are shown for n = 15 cells from three embryos for both Control and OptoMYPT. (e) The path length and total distance in panel c and d were normalized by the average value before blue light illumination, and are plotted as a function of time with SD. (f) Quantification of the border waviness of cell-cell junctions visualized by Lifeact-miRFP703. The border waviness was calculated by dividing the actual length of the cell-cell junction by the distance at each time point. Blue light was illuminated for a total of 10 to 50 min. The average values (bold lines) are plotted as a function of time with the SD. n = 15 cells from three embryos for both the Control and OptoMYPT experiment. $^{**}p<0.01$ by Student's *t*-test at 50 min.

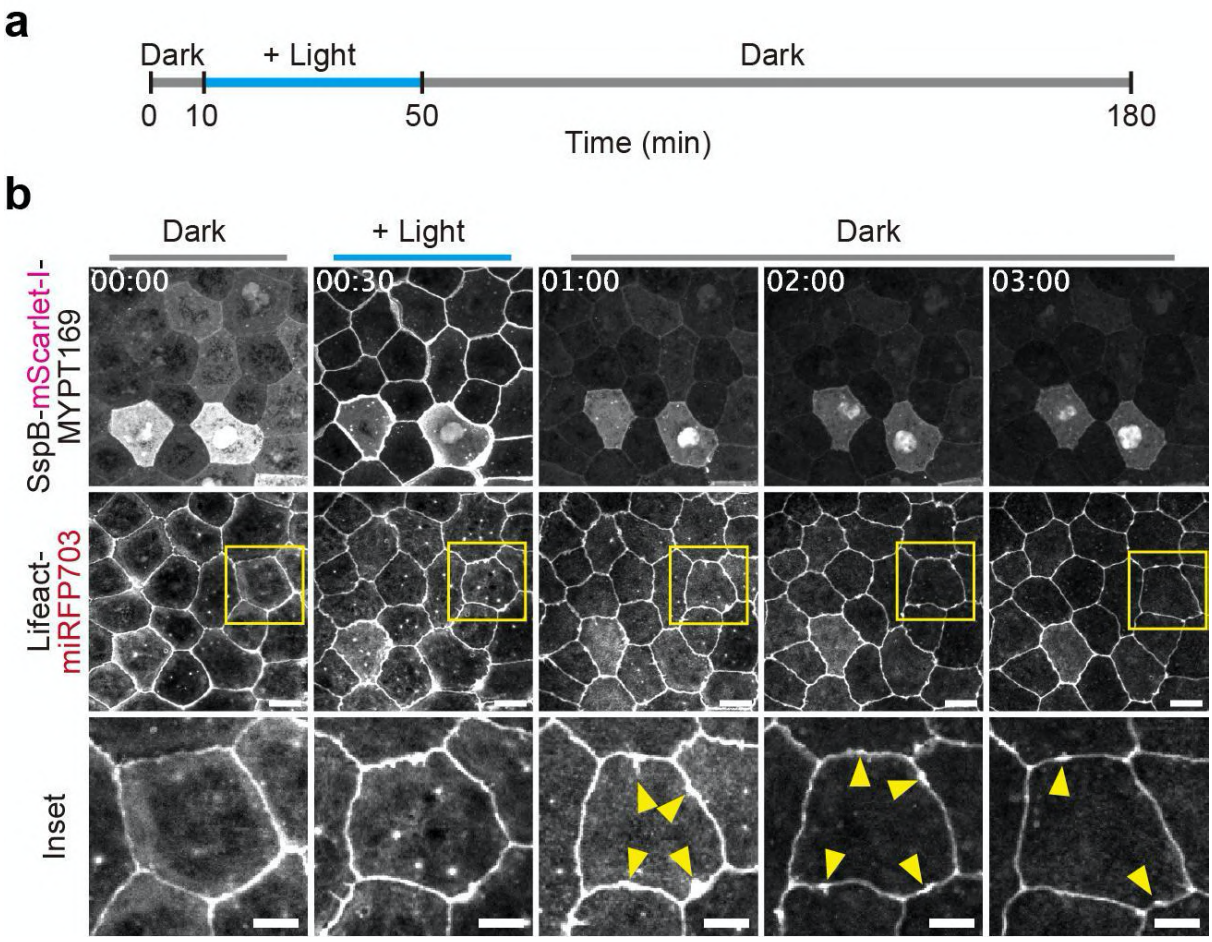

Figure 21. Recovery of wavy cell-cell junction visualized by long-term live imaging.
(a) Time course of long-term imaging. Blue light was illuminated from t = 10 min to t = 50 min. (b) Simultaneous visualization of SspB-mScarlet-I (left) or SspB-mScarlet-I-MYPT169 (right) with F-actin (Lifeact-miRFP703). Cells were globally illuminated through the objective lens with 500 msec of blue light at 20 sec intervals. Lower panels indicate the inset images of yellow boxed regions in middle panels. Yellow arrowheads indicate the accumulation of F-actin. Scale bar, 20 and 10 μm for middle panels and lower panels, respectively.

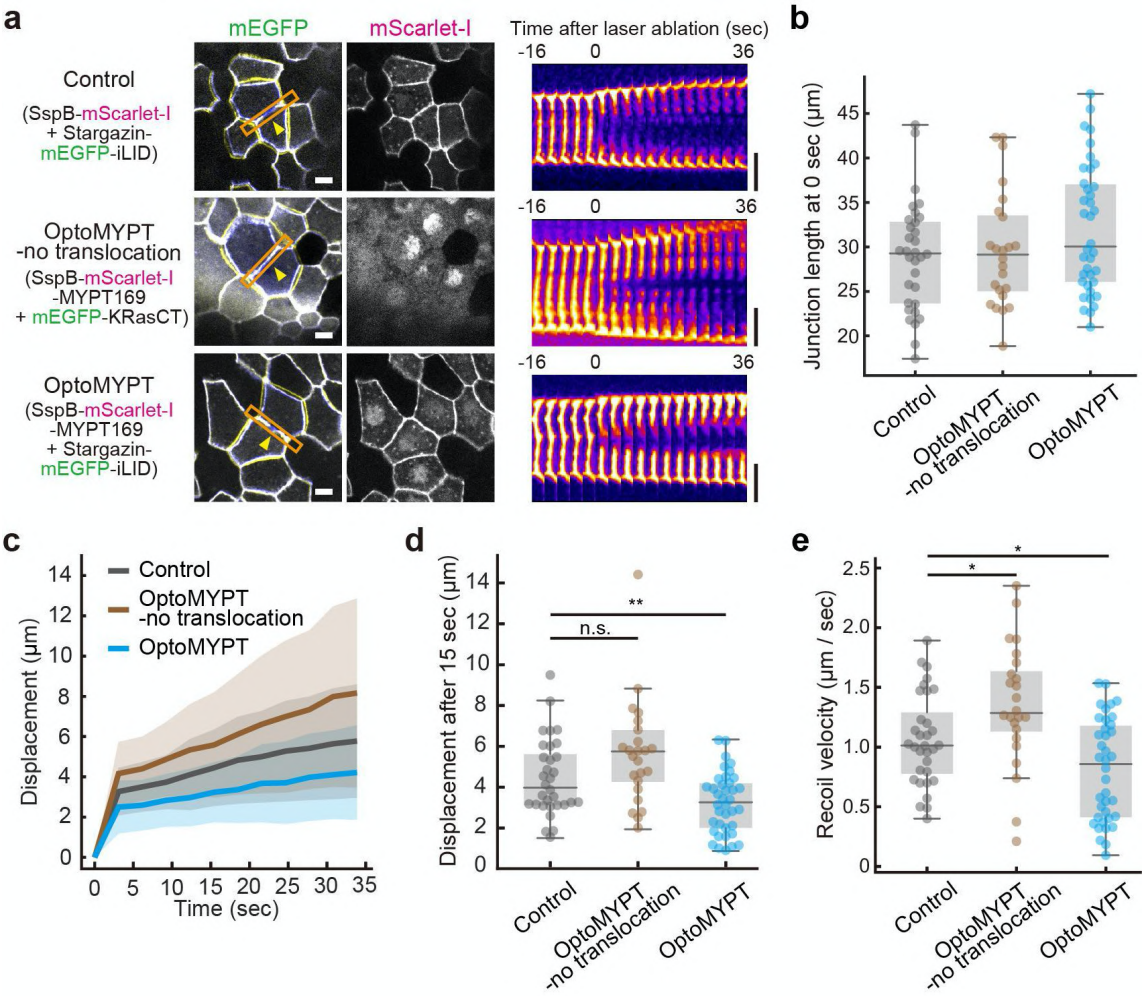

Figure 22. OptoMYPT reduced tension at the cell-cell junction in *Xenopus* embryos.
(a) Laser ablation of the animal pole region at gastrula stages. Representative images of plasma membranes visualized by Stargazin-mEGFP-iLID (upper and lower) or mEGFP-KRasCT (middle) in the left column and SspB-mScarlet-I (upper) and SspB-mScarlet-I-MYPT169 (middle and lower) in the right column. The images at t = 16 sec (blue) before and t = 36 sec (yellow) after ablation were overlaid with the image at t = 0 sec (gray). The yellow arrowheads depict the ablation points. Blue light was continuously illuminated from the top of the embryo 20 min before imaging and continued to be illuminated through the objective lens every 3 sec to visualize cell-cell junctions. Kymographs of the orange boxed areas in panel h are shown on the right side. Scale bar, 20 μm. (b) The junction length at t = 0 sec was shown as a box plot, in which the box extends from the first to the third quartile with the whiskers denoting 1.5 times the interquartile range. A dot indicates data from an individual cell. (c) Time-course kinetics of the displacement after laser ablation. The average values (bold lines) are plotted as a function of time with the SD. n = 32, 24, 38 cells from at least 6 embryos for Control, OptoMYPT-no translocation and OptoMYPT, respectively. (d) Displacement 15 s after ablation. $^{**}p<0.01$ by Student's *t*-test. (e) Recoil velocity was calculated from the difference in junction length before (t = 0) and just after (t = 3.08) laser ablation. $^{*}p<0.05$ (Student's *t*-test). (d, e) Results are shown for n = 32, 24, and 38 cells from at least 6 embryos for Control, OptoMYPT-no translocation, and OptoMYPT, respectively.

3.2.7. Characterization of various actomyosin-binding proteins towards the improvement of the OptoMYPT system.

In the current version of the OptoMYPT, I employed Stargazin or KRasCT to recruit PP1BD and PP1c to the plasma membrane (Fig.7, 10a). However, the dephosphorylation of MLC by this approach is partial and not efficient (Fig.13, 14). Furthermore, the strategy of recruiting PP1c to the plasma membrane may induce dephosphorylation of other proteins such as ERM (see the Discussion section for more details). To address this problem, I investigated some actomyosin-binding localizers other than proteins localized at the plasma membrane.

I cloned MYPT1, Anillin, and MLCK, which are known to contain myosin-binding domains, from cDNAs of HeLa cells (Piekny and Glotzer 2008; Straight, Field, and Mitchison 2005; Silver et al. 1997; Ito et al. 2004) (Fig. 23a). It has been reported that 170-296 a.a. region in the MYPT1 binds to phospho-MLC (Hirano, Phan, and Hartshorne 1997; Tanaka et al. 1998). The acidic cluster located in 297-374 a.a maximizes the affinity with phospho-MLC (Hirano, Phan, and Hartshorne 1997). Therefore, two types of lengths with and without acidic clusters were examined. I also examined iMyo, which is known as an intrabody that binds to myosin heavy chains (Vielemeyer et al. 2010; Hashimoto and Munro 2019), and Lifeact, which binds to F-actin (Riedl et al. 2008) (Fig. 23a). I expressed fusion proteins of these localizers and optogenetic proteins such as CIB and iLID in MDCK cells stably expressing Lifeact-miRFP703, and confirmed their localizations (Fig. 23b). Among the six candidates, Anillin, iMyo, and Lifeact showed fiber-like localization. In particular, iMyo showed a spotted pattern along the fibers, which is characteristic of localization of NMII. On the other hand, MYPT1 and MLCK-derived localizers were diffused in the cytoplasm. These results suggest that the Anillin, iMyo, and Lifeact can be used as actomyosin-binding localizers.

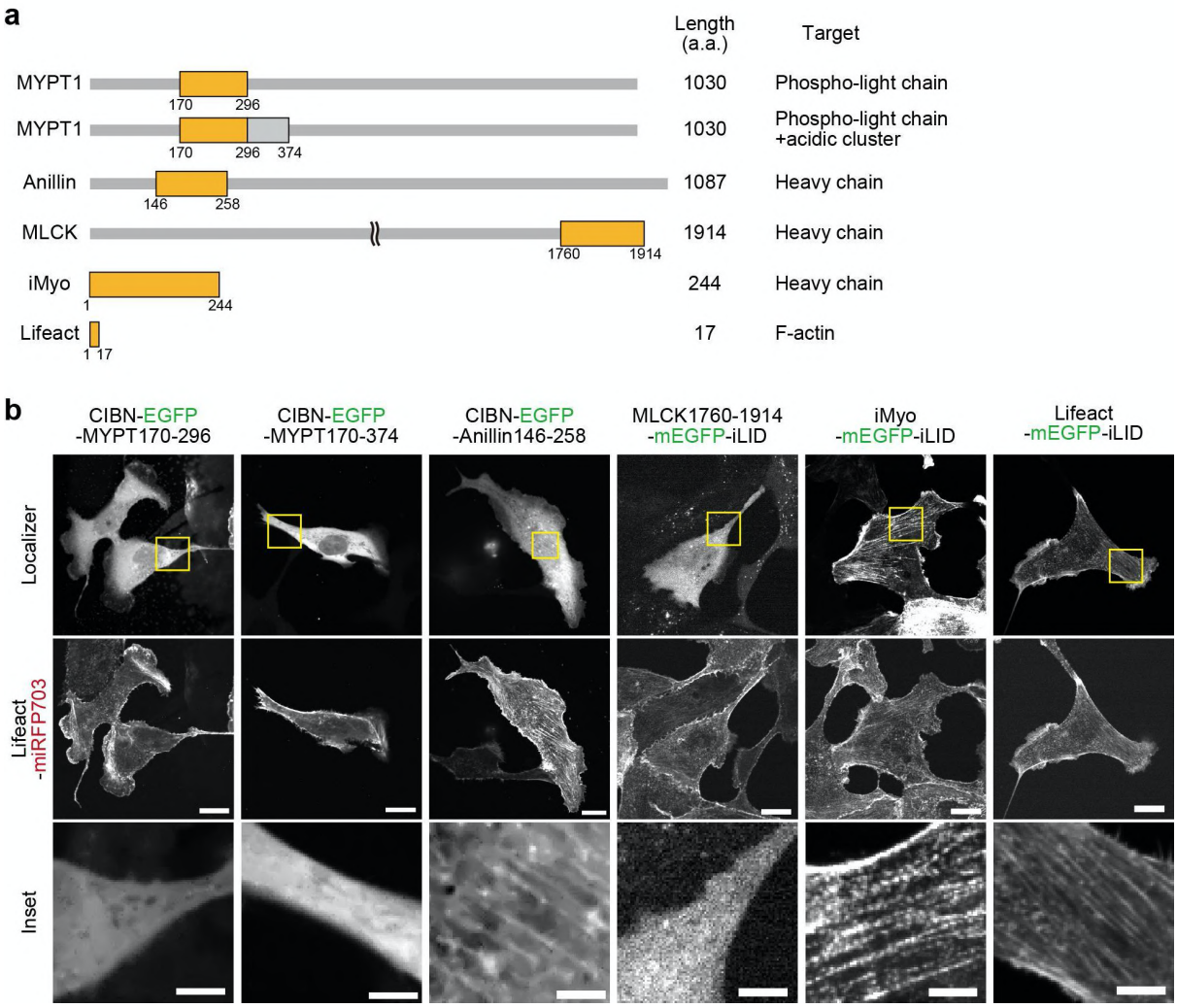

Figure 23. Examination of localizers for the improvement of the OptoMYPT system.
(a) Schematic illustrations of MYPT1 (human), Anillin (human), MLCK (human), iMyo, and Lifeact. The actomyosin-binding domain and the acidic cluster are represented as an orange and gray box, respectively. Binding targets of each protein are shown on the right side. (b) Localizations of each actomyosin-binding protein. Inset images show yellow boxed regions in upper panels. Scale bar, 20 and 5 μm in middle and lower panels, respectively.

3.3. Discussion

3.3.1. Comparison of OptoMYPT and conventional methods

In this chapter, I developed a new optogenetic tool, OptoMYPT, and demonstrated light-dependent relaxation of cellular forces at the subcellular level. The current main method to weaken actomyosin contractility is pharmacological, using small chemical compounds (Straight et al. 2003; Uehata et al. 1997; Saitoh et al. 1987). These drugs act on the entire cell, making it difficult to act on them locally. Although local application of drugs with a micropipette have been reported, it is difficult to observe specimens for a long time due to rapid diffusion of drugs (Sedzinski et al. 2011; O'Connell, Warner, and Wang 2001). In addition, genetic approach such as knock-down or knock-out of actomyosin-related protein also affects the entire cell. On the other hand, using OptoMYPT, I have succeeded in dephosphorylating MLCs and weakening contractility at the subcellular level (Figs. 13, 15, and 17-19). A notable advantage of OptoMYPT is the ability to move or specify multiple ROIs for light irradiation (Table 2).

The OptoMYPT will provide new flexibility in force measurement. Various methods have been used to study the mechanical properties of cells, such as laser ablation, AFM, and microaspiration (Gómez-González et al. 2020). Although these methods are significant to acquire absolute value of the mechanical properties, these methods are sometimes invasive to the cell. Moreover, these methods only measure one part of the cell, making it difficult to examine the contributions of multiple local forces within the cell or tissues. In this respect, OptoMYPT affects the cell mildly and perturb multiple regions simultaneously. Future studies are expected to validate the OptoMYPT in more detail, and establish a quantitative force reduction method. In addition, optogenetic experiments only require conventional confocal microscopy; it does not require special equipment such as laser ablation, AFM, and microaspiration. This makes force measurement or perturbation much easier in terms of

technique. Furthermore, while it is still technically difficult to combine high-resolution imaging with conventional methods, optogenetic experiments make it possible. Such an advantage is suitable for studying causal relationships between local force perturbation and morphological changes with high spatial and temporal precision (Table 3).

The OptoMYPT is substantially different from existing optogenetic tools that are related to cell mechanics in two ways. First, the OptoMYPT reduces contractile forces below the basal level, and therefore provides additional flexibility for *in situ* control of actomyosin contractility and cellular morphology. Second, the OptoMYPT directly regulates NMII through MLC dephosphorylation, whereas optogenetic modulation of RhoA activity, so-called "OptoRhoGEF", or $PI(4,5)P_2$ may affect pathways other than NMII, since RhoA and $PI(4,5)P_2$ are known to control various downstream effectors such as ROCK, mDia, and the ERM proteins (Oshiro, Fukata, and Kaibuchi 1998; Yonemura et al. 2002; Narumiya, Tanji, and Ishizaki 2009) (Table 2 and 3).

	Local control	Specificity	Reversibility	Efficiency
OptoMYPT	○	△	○	△
Chemical compounds	△	○	△	○
Genetics	×	○	×	○
OptoRhoGEF	○	△	○	△

Table 2. Comparison of OptoMYPT and conventional force perturbation methods.

	Quantitative measurement	Invasiveness	Multi-point measurement	Combination with imaging
OptoMYPT	△	○	○	○
Laser ablation	○	×	△	△
Microaspiration	○	△	×	△
AFM	○	△	×	△
OptoRhoGEF	△	○	○	○

Table 3. Comparison of OptoMYPT and conventional force measurement methods.

3.3.2. Substrate specificity of the OptoMYPT system.

There still remain some issues to be addressed with respect to the OptoMYPT. First is the issue of substrate specificity in OptoMYPT (Table 2). We could not exclude the possibility that the OptoMYPT dephosphorylates additional substrates other than MLC. In addition, the expression of PP1BD of MYPT affected the localization of endogenous PP1c (Figs.9a and 11a). Some proteins are dephosphorylated by PP1c in the nucleus (Kiss et al. 2008), and therefore the nuclear exclusion of PP1c by OptoMYPT may disturb its nuclear function. However, based on the fact that the expression of MYPT296 did not dephosphorylate ERM proteins (Fig. 8d), it seems somewhat unlikely that OptoMYPT dephosphorylates and inactivates the ERM proteins.

The next issue is the localizer of optogenetic switches. In the current OptoMYPT system, dephosphorylation of MLC was induced by recruiting MYPT169 to the plasma membrane upon illumination with blue light. It is plausible that the OptoMYPT dephosphorylates and inactivates only the NMII existing in the vicinity of the plasma membrane, such as in the lamellipodial region (Fig. 13) and at cell-cell junctions in *Xenopus* embryos (Figs. 20-22). Meanwhile, my data suggest that OptoMYPT is incapable of dephosphorylating MLCs that are located away from the plasma membrane and/or that are incorporated in the highly bundled actin fibers, such as stress fibers (Fig. 17) and the contractile ring (Fig. 28). To overcome this limitation, I examined six candidates of localizer derived from actomyosin-binding proteins, and found that Anillin, iMyo, and Lifeact can be used as localizers (Fig. 23). In future, it is necessary to validate whether these localizers can reduce the contractile force more efficiently. One concern is that these localizers bind to the endogenous actomyosin, so that their expression level should be carefully controlled in order not to freely diffuse in the cytoplasm.

3.3.3. Efficiency of dephosphorylation of MLC by OptoMYPT system

Here, I discuss the efficiency of MLC dephosphorylation by the OptoMYPT system (Table 2). Based on immunofluorescence analysis, the efficiency of MLC dephosphorylation was approximately 60% (Fig. 13). This value may contain the effect of increased phosphorylation level in the dark area, because I quantified phospho-MLC level by dividing the fluorescence intensity of the light area by that of the dark area. I often observed tail retraction in the opposite side of the light-illuminated area, supporting the possibility of increase in phosphorylation in the dark area (Fig. 15e). In addition, based on western blotting analysis, the efficiency of dephosphorylation was approximately 75% compared to cells expressing OptoMYPT proteins under dark conditions (Fig. 14). The resulting decrease of the traction force was approximately 70-80% compared to the dark condition (Fig. 19). These results indicate that the efficiency of dephosphorylation of MLC and force reduction is partial.

As I mentioned in the above section, these low efficiencies may be improved using other actomyosin-binding localizers. Another possible way is to increase the expression level of PP1c. According to my estimation, the expression level of transiently overexpressed PP1BD was 50-fold higher than that of endogenous MYPT1 (Fig. 12). Therefore, there could be an excess amount of PP1BDs that do not bind to the endogenous PP1c. In principle, if the expression level of PP1c can be increased by overexpression, local concentration of PP1c can be increased upon local light-illumination. However, this approach seems to be difficult for the following two reasons. First, the overexpression itself is difficult. I overexpressed PP1c in MDCK cells, but the expression level was low compared to that of other proteins overexpressed by the same amount of plasmids (data not shown). The overexpressed PP1c could be unstable and/or toxic. Second, it has been reported that the soluble fraction of PP1c in the cytoplasm can also dephosphorylate MLC (Chang et al. 2018), suggesting that the basal phospho-MLC level may be reduced by the overexpression.

3.3.4. Reversibility of the OptoMYPT system

One of the advantages of using optogenetics is its reversibility (Table 2). In experiments using small chemical compounds, it is often technically difficult to wash out the drug. In this respect, most LID proteins reversibly dissociate under the dark conditions or illumination with specific wavelengths (Klewer and Wu 2019; Krueger et al. 2019). SspB-mScarlet-I-PP1BDs also rapidly dissociated from the plasma membrane after turning off blue light (Figs. 9, 17, and 21). However, it took a relatively long time for the cell morphology to recover to the original state (Figs. 17, 21). Particularly, the recovery of junctional shape took approximately 2 hours in *Xenopus* embryos (Fig. 21). On the other hand, Valon et al. reported that optogenetic recruitment of RhoGEF to the plasma membrane increases the traction force and it recovered to the original state within 15 min in MDCK cells (Valon et al. 2017). Similar strategy has demonstrated that local accumulation of actomyosin by light diminishes within 10 min (Wagner and Glotzer 2016). In the case of *Xenopus* embryos, higher junctional tension induces RhoA flares, leading to the local accumulation of F-actin and reorganization of cell-cell junctions (Varadarajan et al. 2021). This process is completed within 300 sec, although a similar phenotype of local accumulation of F-actin was observed in my long-term observation (Fig. 21). One possibility to explain these differential recovery times is the existence of bistability of actomyosin contractility. If the actomyosin contractility is stable at the high-contractile state, optogenetic increase in actomyosin contractility is rapidly recovered to the original state due to the decay or negative feedback mechanisms. On the other hand, optogenetic decrease in actomyosin contractility should be recovered by positive feedback mechanisms from actomyosin to upstream factors (Uyeda et al. 2011; Priya et al. 2015). The experimental data of long recovery time may indicate that the transition to another state where positive feedback is less likely to be worked and low-contractile state is stabilized.

4. Chapter II: Application of the OptoMYPT system to understand the mechanics of cytokinesis

4.1. Introduction

Mechanics of cytokinesis

Cytokinesis is the final step of cell division to mechanically divide a cell into two daughter cells. In this process, actin, NMII, and cross-linkers constitute a contractile ring in the equatorial plane, and generate force by constriction (Pollard 2010; Green, Paluch, and Oegema 2012) (Fig. 24, solid arrows). On the other hand, the tension developed in cortical actomyosin counteracts the force in the contractile ring (Yoneda and Dan 1972; Turlier et al. 2014; Stachowiak et al. 2014; Rodrigues et al. 2015; Kunda et al. 2008; Chapa-Y-Lazo et al. 2020) (Fig. 24, dashed arrows). Thus, to advance the constriction, the contractile ring has to overcome the resistance of the actin cortex. There are two mechanisms for driving the cytokinesis; increasing tension of the contractile ring and weakening tension of the cell cortex. The latter mechanism, so-called “polar relaxation”, through, for example, NMII removal from the polar region, is required for proper cytokinesis (Yoneda and Dan 1972; Turlier et al. 2014; Stachowiak et al. 2014; Rodrigues et al. 2015; Kunda et al. 2008; Chapa-Y-Lazo et al. 2020), but genetic and pharmacological inhibition of cortical actomyosin often induce cytokinetic failure (Taneja et al. 2020; Yamamoto et al. 2019; O’Connell, Warner, and Wang 2001; Wiggan et al. 2012). To elucidate the underlying mechanics, the strength of cortical tension has been directly measured using atomic force microscopy (AFM), microaspiration, and laser ablation methods (Taneja et al. 2020; Matzke, Jacobson, and Radmacher 2001; Tinevez et al. 2009). However, clarifying the contribution of cortical tension is still technically challenging due to the highly dynamic nature of cytokinesis.

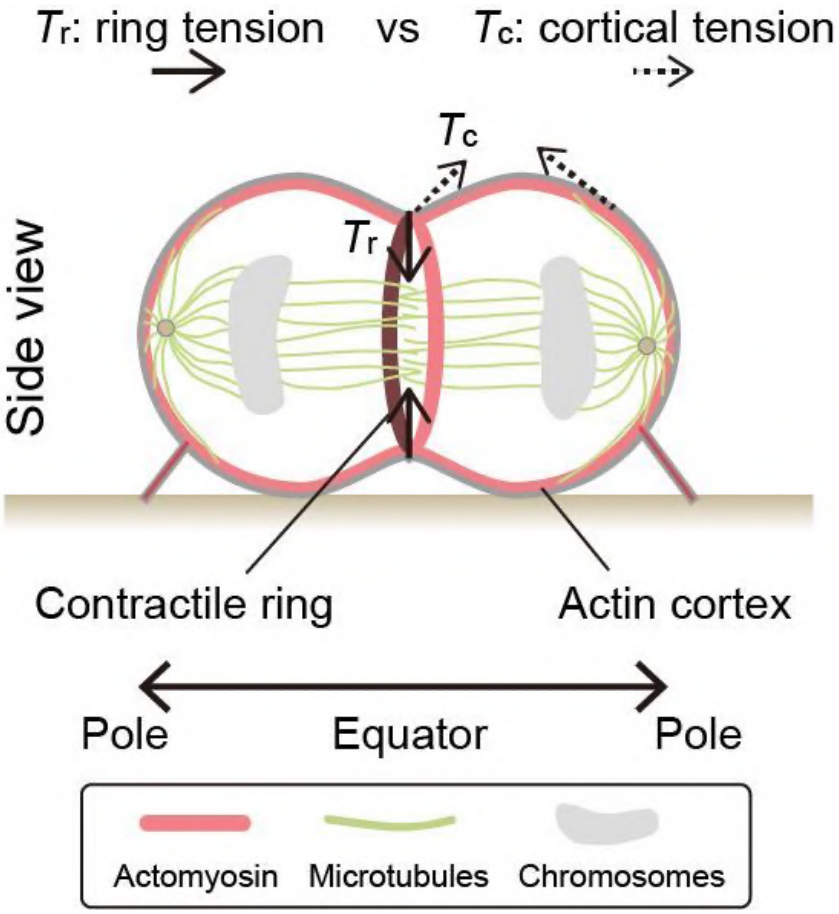

Figure 24. Mechanics of cytokinesis.
Schematic illustration of cytokinesis in animal cells. Solid and dashed arrows indicate ring tension and cortical tension, respectively. Pink, green, and gray objects indicate actomyosin, microtubules, and chromosomes, respectively.

4.2. Results

4.2.1. Experimental setup for the local blue light illumination during cytokinesis.

To quantitatively clarify the contribution of cortical tension to the ring tension, I expected that optogenetic perturbation of the cortical tension by the OptoMYPT system would be a new and potentially effective approach. Blue light was locally and repeatedly illuminated at both poles from the onset of chromosome segregation (Fig. 25a, upper and lower panels). SspB-mScarlet-I and SspB-mScarlet-I-MYPT169 were trapped in the polar region (Control-pole and OptoMYPT-pole, respectively) (Fig. 25a). Because the overexpression of OptoMYPT might reduce basal actomyosin activity (Fig. 15), cells expressing SspB-mScarlet-I-MYPT169 under a dark condition throughout cytokinesis (OptoMYPT-dark) were also used as another control (Fig. 25a, middle panels).

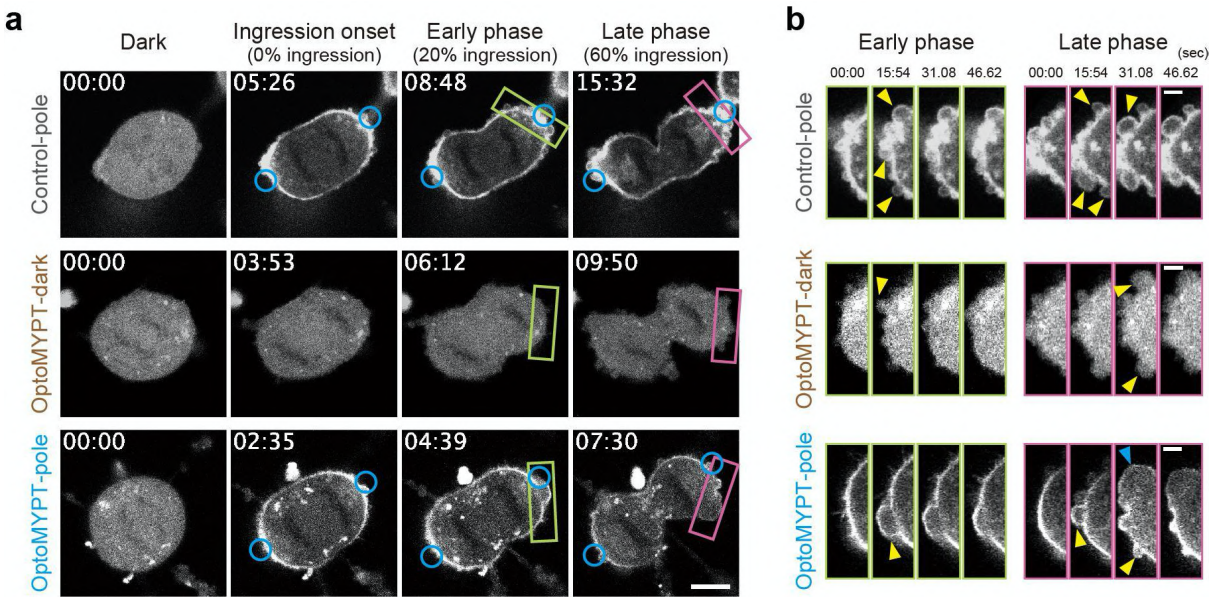

Figure 25. Local blue-light illumination during cytokinesis.
(a) Representative images of SspB-mScarlet-I (upper) or SspB-mScarlet-I-MYPT169 (middle and lower) in MDCK cells during cytokinesis. The blue circular regions were locally illuminated with blue light every 3.11 sec. Middle panels represent the cytokinesis of a cell under dark conditions. Scale bar, 10 μm. (b) Inset images of polar blebbing (the green and magenta boxed regions in panel b, representing the early and late phases, respectively). Yellow and blue arrowheads indicate small and large new blebs per stack, respectively. Scale bar, 3 μm.

4.2.2. Quantification of blebbing dynamics during cytokinesis.

I quantified the dynamics of membrane blebbing at the polar cortex during cytokinesis (Fig. 26a), because bleb formation requires the intracellular pressure generated by cortical tension to be high enough to overcome membrane-cortex anchoring and surface tension of the plasma membrane (Sedzinski et al. 2011; Tinevez et al. 2009; Charras and Paluch 2008). I found that the level of membrane bleb formation following the onset of cleavage furrow ingression was lower in OptoMYPT-pole cells than Control-pole or OptoMYPT-dark cells (Fig. 26b). In addition, I found that the local activation of OptoMYPT altered the onset and size of membrane bleb formation during cytokinesis (Fig. 26c, d). First, the onset of blebbing was delayed in OptoMYPT-pole cells, while Control-pole and OptoMYPT-dark cells showed blebbing from the early phase of ring constriction (Fig. 26c). Second, in the later phase of cytokinesis, OptoMYPT-pole cells exhibited large blebs (Figs. 25b, blue arrowhead, 26d), although the bleb counts were still smaller than the control cases. I should note that the OptoMYPT activation might weaken the membrane-cortex linkage, such as by ERM deactivation. However, this weakening of the membrane-cortex linkage has been shown to render the OptoMYPT-pole cells more prone to bleb formation (Rodrigues et al. 2015; Charras and Paluch 2008). Therefore, the absence of blebbing in the early phase indicates reduced tension in OptoMYPT-pole cells independent of whether membrane-cortex linkage is weakened or not. On the other hand, the larger blebs of the OptoMYPT-pole cells in the late phase, possibly initiated by excess intracellular pressure coming from ring constriction, might be explained by both the weakening of the membrane-cortex linkage and inefficient bleb retraction (see the Discussion section for more details).

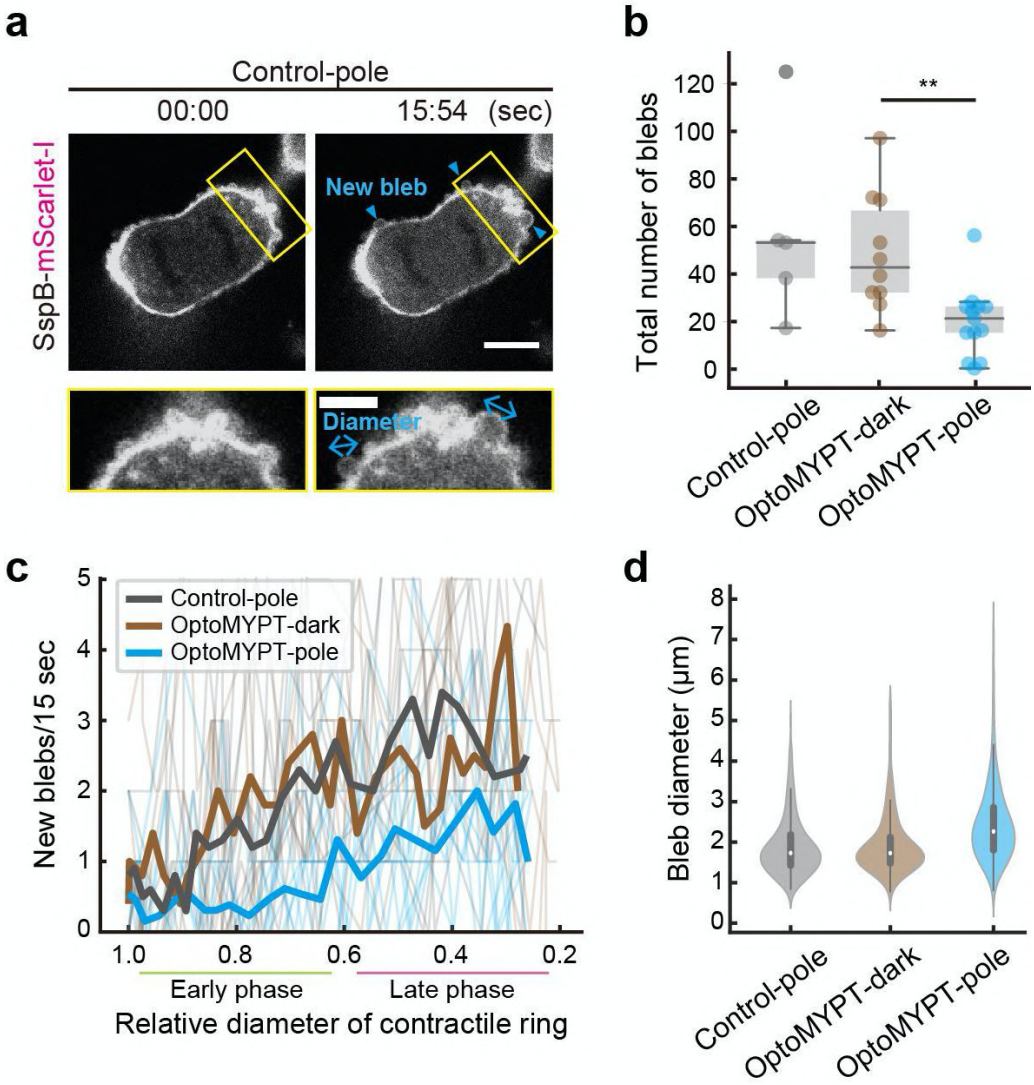

Figure 26. Quantification of blebbing dynamics during cytokinesis.
(a) Representative image of an MDCK cell expressing SspB-mScarlet-I and Stargazin-mEGFP-iLID used for the quantification of the bleb diameter. The blue arrowheads in the upper panel indicate new blebs per 15.54 sec. The blue arrows in the lower panel indicate measured bleb diameters. The lower panels are a magnified view of the yellow-boxed regions in the upper panels. Scale bar, 10 and 5 μm for the upper and lower panels, respectively. (b, c) Quantification of the total number of blebs during cytokinesis, shown as a box plot (b), and of the number of new blebs emerged within 15.54 sec, shown as a line graph (c), in which thin and bold lines indicate individual and averaged data, respectively. n = 5, 10, and 13 cells for Control-pole, OptoMYPT-dark, and OptoMYPT-pole, respectively. $^{**}p < 0.01$ (student's *t*-test). (d) The diameter of blebs in the Control-pole, OptoMYPT-dark, and OptoMYPT-pole cells are shown as a violin plot. The counted number of blebs was 266, 360, and 257 for Control, OptoMYPT-dark, and OptoMYPT-pole, respectively.

4.2.3. Acceleration of the ingression rate of cleavage furrows during cytokinesis by the optical relaxation of cortical tension.

Next, I investigated the effects of OptoMYPT on the dynamics of ring constriction. I measured the furrow ingression rate under each condition to gain insight into how the cortices affected the furrow ingression. The ingression rate of the cleavage furrow was significantly higher in OptoMYPT-pole cells (2.26 ± 0.25 μm/min) than in Control-pole cells (1.55 ± 0.20 μm/min) and OptoMYPT-dark cells (1.93 ± 0.33 μm/min) (Fig. 27). These results highlight the negative contribution of the cortices to the cleavage furrow ingression. Of note, the ingression rate of OptoMYPT-dark cells was slightly higher than that of Control-pole cells (Fig. 27), suggesting the basal effects of OptoMYPT on MLC phosphorylation even under the dark condition.

I also conducted an experiment in which the equatorial plane of dividing cells was irradiated with blue light, because it has been reported that the actomyosin-based contractility is associated with the constriction of the contractile ring (Pollard 2010; Green, Paluch, and Oegema 2012). However, blue light illumination at the equatorial plane of dividing cells had no influence on the ingression rate of cleavage furrow (see the Discussion section for more details) (Fig. 28).

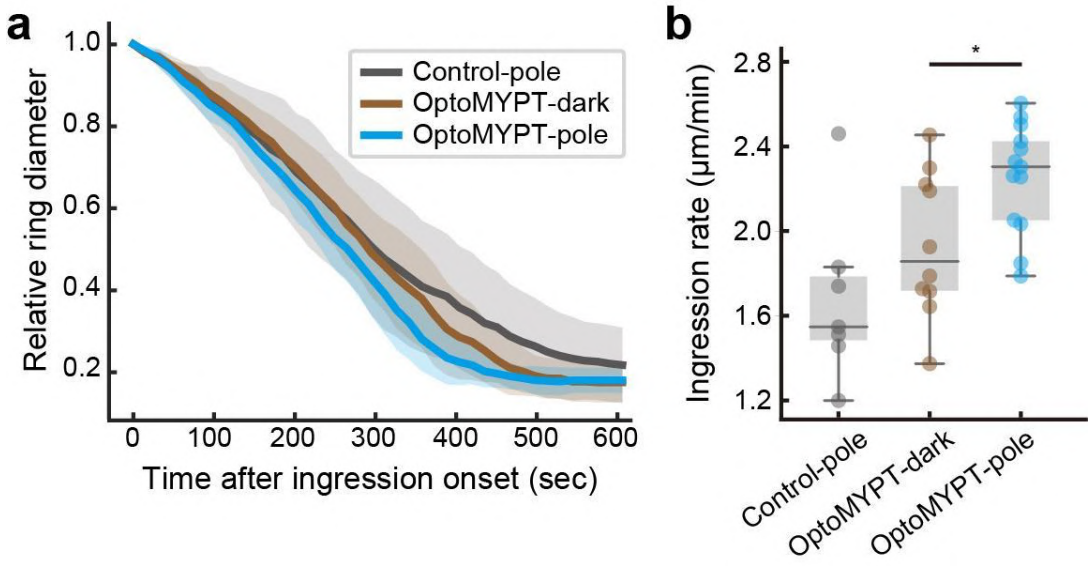

Figure 27. Quantification of the furrow ingression rate.
(a, b) Quantification of the furrow ingression rate after ingression onset. Averaged relative diameters are plotted as a function of time with the SD (a). The ingression rate was estimated by calculating the slope of the ingression rate from 1.0 to 0.6 in panel f, and shown as a box plot (b). n = 7, 10, and 13 cells for Control-pole, OptoMYPT-dark, and OptoMYPT-pole, respectively. *$p < 0.05$ (student's *t*-test).

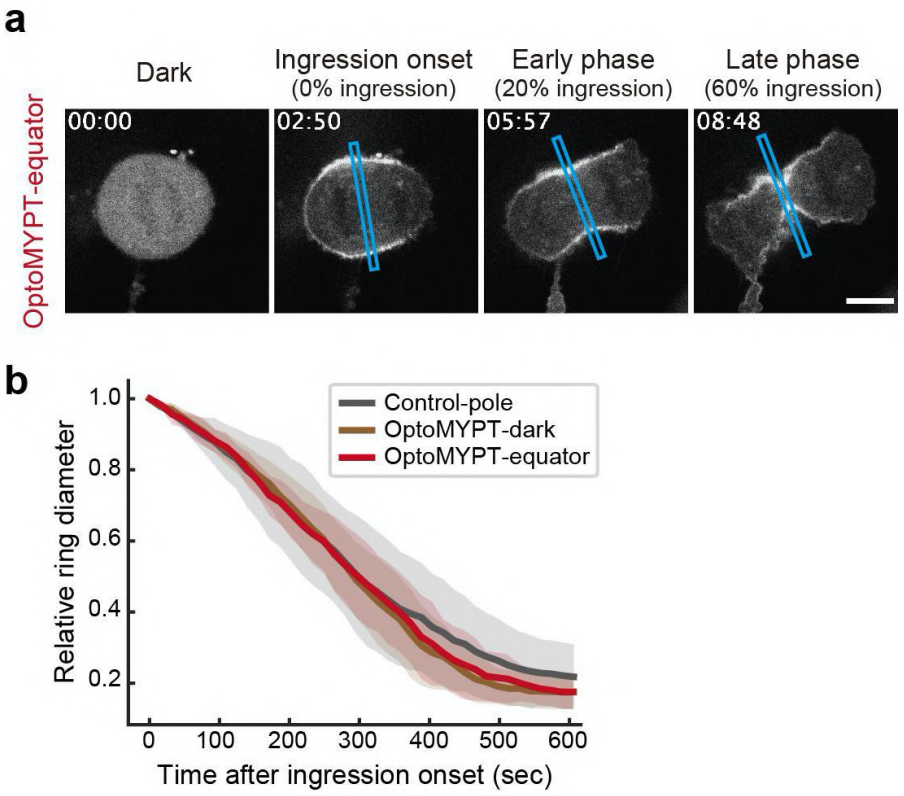

Figure 28. Blue light illumination to the equatorial region during cytokinesis.
(a) Representative images of SspB-mScarlet-I-MYPT169 in MDCK cells during cytokinesis. The blue boxed regions were illuminated with blue light every 3.11 sec. Scale bar, 10 μm. (b) Quantification of the furrow ingression rate in OptoMYPT-equator cells. Ingression rates of Control-pole and OptoMYPT-dark in Figure 4f are merged. Averaged relative diameters are plotted as a function of time with the SD. Results are shown for n = 5 cells for OptoMYPT-equator.

4.2.4. Physical modeling of cytokinesis.

To quantify how the OptoMYPT activation modified the cortical tension, I adopted a coarse-grained physical model describing the mechanics of cytokinesis. Previous studies have established a simple equation for the equilibrium of forces between the contractile ring and the two polar cortices (Yoneda and Dan 1972; Sedzinski et al. 2011; Turlier et al. 2014). Based on the Young-Laplace law, the force balance is written as

$$\boldsymbol{\sigma_r = 2R_r T_c \cos\theta}\ , \text{(S1)}$$

where σ_r is the net tension in the ring and T_c is the tension in the polar cortices (see Figure 29 for the definitions of the geometric factors R_r and θ). Since the turnover of cortical actin (~10 sec) is much faster than the time scale of cytokinesis (~10 min), the material property of polar cortices can be described as active viscous liquid (Turlier et al. 2014). Thus, the cortical tension depends on both the mechanical strength of the cortical cytoskeleton, which causes the effective viscosity, and myosin motors, which cause active tension. Here I simply describe the cortices as an active viscous membrane having tension T_c. On the other hand, the net tension in the ring is composed of two factors, tension generated by myosin motors T_r and viscous resistance by, e.g., cross-linkers, as

$$\boldsymbol{\sigma_r = T_r + \alpha \frac{dR_r}{dt}},\ \text{(S2)}$$

where the coefficient α represents the viscosity of the actin network constituting the ring (Sedzinski et al. 2011; Yoneda and Dan 1972; Turlier et al. 2014). Here, if we combine Eqs. S1 and S2, we obtain

$$\boldsymbol{\alpha \frac{dR_r}{dt} = -(T_r - 2R_r T_c \cos\theta)}\ ,\quad \text{(S3)}$$

Note that this model was simplified from Eq. S1 in the report of (Sedzinski et al. 2011), since I consider symmetric pole shapes. For brevity, let F_r and F_c denote T_r (ring tension) and $2R_rT_c \cos\theta$ (cortical tension), respectively (Fig. 29).

Then, the furrow ingression rate of control cells (Control-light and OptoMYPT-dark), v, can be expressed as

$$\boldsymbol{v \propto F_r - F_c}\ , \text{(S4)}$$

where F_r and F_c are the ring tension and the cortical tension, respectively (Fig. S8). The furrow ingression rate of OptoMYPT-pole cells, v', can be expressed as

$$\boldsymbol{v' \propto F_r - F_c'}\ , \text{(S5)}$$

where F_c' is the cortical tension upon blue light illumination. Note that F_r is considered to be constant under each condition, because blue light was locally illuminated to the polar cortices. Taken together with Eqs. S4 and S5, I obtain

$$\boldsymbol{v/v' = (F_r - F_c)/(F_r - F_c') > (F_r - F_c)/(F_r)}. \quad \text{(S6)}$$

The rightmost expression represents the case where blue light illumination completely reduces cortical tension to zero. I rearrange the above formula as

$$\boldsymbol{F_c/F_r > 1 - v/v'}. \quad \text{(S7)}$$

Based on the experimental data in Figure 27, the furrow ingression rate of Control-pole cells, OptoMYPT-dark cells, and OptoMYPT-pole cells were v = 1.55 ± 0.20 μm/min, v = 1.93 ± 0.33 μm/min, and v' = 2.26 ± 0.25 μm/min, respectively. Thus, the cortical tension relative to ring tension is estimated as

$$\boldsymbol{F_c/F_r > 1 - (1.55\sim1.93)/2.26 = 0.15\sim0.31}. \quad \text{(S8)}.$$

Finally, I estimated that the resisting force exerted by the cortices corresponds to 15%~31% of the ring tension during cytokinesis.

Here, I discuss why I ignored the contribution of cytoplasmic pressure on the contractile ring. Assuming that the cytoplasmic pressure is uniform within a cell, then the contribution of cytoplasmic pressure on the contractile ring, P_r, is written as

$$\boldsymbol{P_r = aR_rP}. \quad (S9).$$

where a is the height of the contractile ring when it is assumed to be a cylinder, and P is the cytoplasmic pressure (Fig. 30).

Based on the Young-Laplace law for force balance at the polar cortice, $P = 2T_c/R_c$, then P_r is written as

$$\boldsymbol{P_r = 2aR_rT_c \,/\, R_c}. \quad (S10).$$

where Rc is the radius of the daughter cells (Fig. 30).

Combining Eqs. S1 and S10, I obtain the ratio of contributions made by cytoplasmic pressure on the contractile ring and cortical tension as

$$\boldsymbol{P_r \,/\, 2R_rT_c \cos\theta = (2aR_rT_c \,/\, R_c)/\, 2R_rT_c \cos\theta = a/R_c \cos\theta}. \quad (S11).$$

Based on my observation of HeLa and MDCK cells, a crude estimate for cos θ is ~ 0.5, and R_c is sufficiently large compared to a, so that the contribution of cytoplasmic pressure on the contractile ring, P_r, can be ignored except at the onset of furrow ingression. The contribution of cytoplasmic pressure may be significant when the height of the contractile ring is large, as is the case in *D. discoideum* (W. Zhang and Robinson 2005).

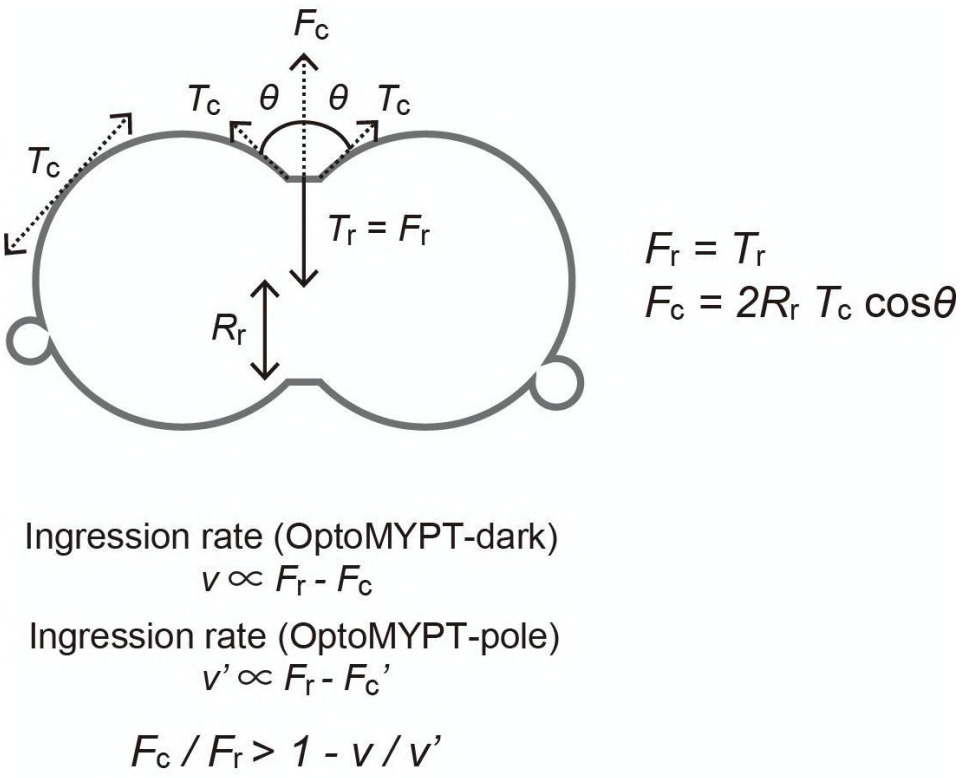

Figure 29. Physical modeling.
T_c and T_r are the cortical tensions at the actin cortex and contractile ring, respectively. R_r is the ring diameter. F_r and F_c correspond to the force generated by ring tension and cortical tension, respectively.

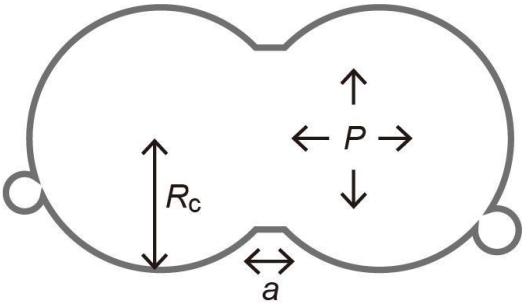

Figure 30. Estimation of the contribution of cytoplasmic pressure on the contractile ring.

P is the uniform cytoplasmic pressure. R_c is the diameter of the daughter cells. *a* is the height of the contractile ring when it is assumed to be a cylinder.

4.2.5. OptoMYPT induced shape instability during cytokinesis.

Finally, I varied the local activation patterns of OptoMYPT in dividing cells. Sedzinski *et al*. have demonstrated that the perturbation of the cortex at one pole of dividing cells by laser ablation or local application of an actin-depolymerizing drug leads to cytokinetic shape oscillations (Sedzinski et al. 2011). To reproduce this report, I illuminated only one of the polar regions by blue light throughout cytokinesis (OptoMYPT-single pole). As expected, I often observed extensive cell shape oscillation with the back-and-forth motion of separated chromosomes (Fig. 31a). In the early event of cell shape oscillation, a large bleb was formed from the pole irradiated with blue light (Fig. 31a, yellow arrowhead). This result is consistent with a report showing that cytokinetic oscillation is triggered by the retraction of large blebs (Taneja et al. 2020). I classified oscillation into three types: normal cytokinesis (no oscillation occurs), small oscillation (the daughter chromosomes oscillate slightly), and large oscillation (both chromosomes enter one daughter cell) (Fig. 31b). OptoMYPT-single pole experiments increased the fraction of cells showing “large oscillation” (Fig. 31b). OptoMYPT-dark seems to have a lower percentage of oscillation than Control-pole (Fig. 31b), possibly due to the decrease in basal cortical tension by the expression of OptoMYPT.

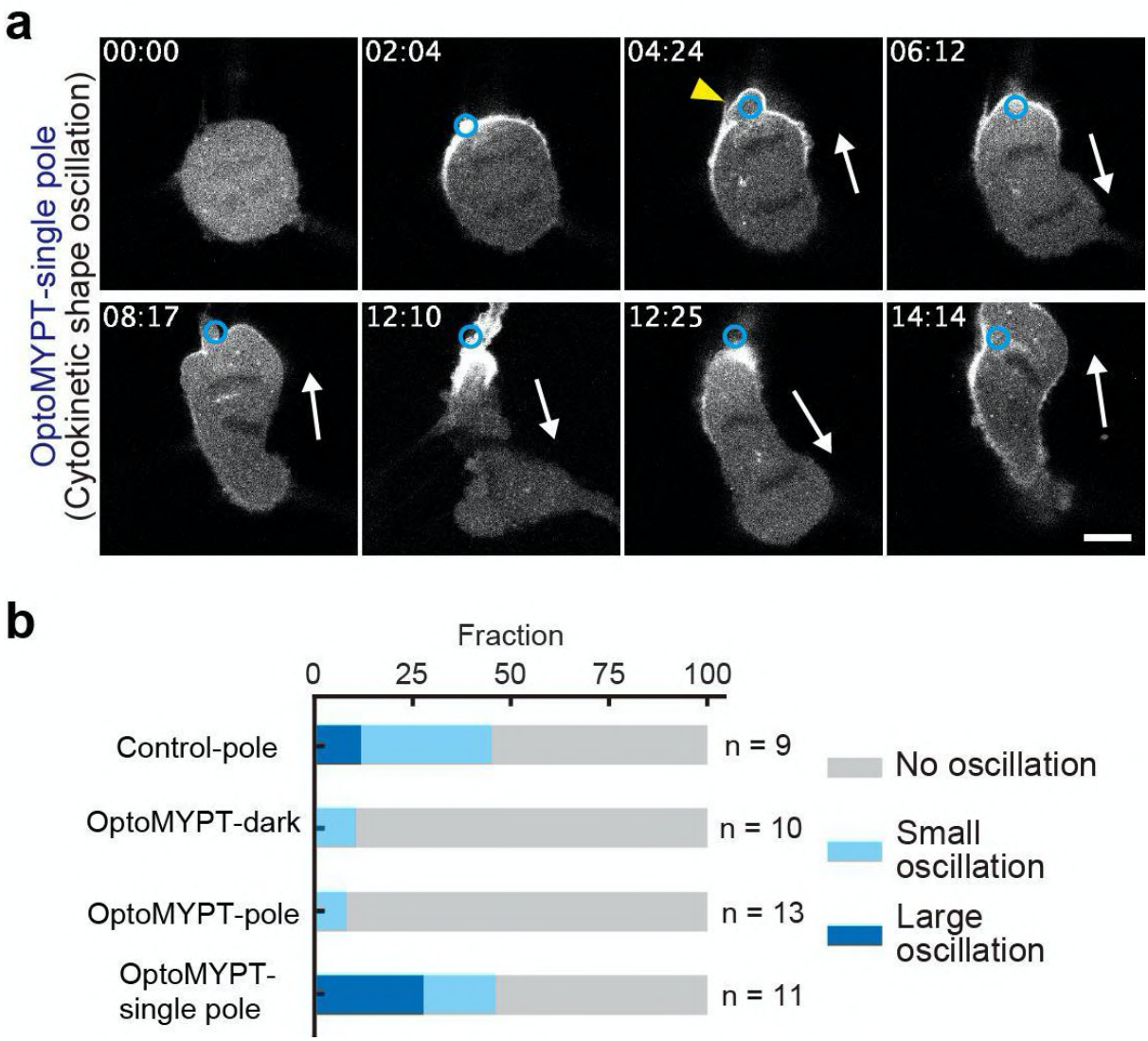

Figure 31. Single polar illumination-induced cytokinetic shape oscillation.
(a) Representative images of SspB-mScarlet-I-MYPT169 during cytokinesis upon illumination to the single pole. The blue circular regions were locally illuminated with blue light every 3.11 sec. The yellow arrowhead and white arrow indicate a large bleb just before spindle oscillation and the direction of chromosome motion, respectively. Scale bar, 10 μm. (b) Quantification of the fraction of the cytokinetic dynamics under the indicated conditions. The small oscillation and large oscillation are defined as a slight oscillation of the spindle and an oscillation of two daughter chromosomes entering one of the cells, respectively.

4.3. Discussion

4.3.1. Role of cortical tension during cytokinesis.

Using the OptoMYPT system, I experimentally revealed the negative contribution of the cortical tension to the cleavage furrow ingression rate during cytokinesis; *i.e.*, the decrease in cortical tension at both poles by OptoMYPT accelerates furrow ingression (Figs. 27 and 33). It has been reported that the reduction of cortical tension by laser ablation in the polar region decelerates cleavage furrow ingression in cytokinesis of *C. elegans* embryos (Khaliullin et al. 2018). This discrepancy could be due to the difference in the force balance between the pole and equator; in *C. elegans* zygotes, NMII is actively removed from the polar region and accumulates at the equator due to the cortical flow, so called polar relaxation, and thus cortical tension is much weaker than ring tension (Chapa-Y-Lazo et al. 2020; Reymann et al. 2016) (Fig. 32). Furthermore, this hypothesis about the weaker contributions of cortical tension in *C. elegans* is also supported using some genetic mutant strains; loss of CED-10 or ARX-2, either of which is known to generate cortical tension by promoting actin branching (Loria, Longhini, and Glotzer 2012), slightly decelerates furrow ingression rate (D. Zhang and Glotzer 2015). Meanwhile, my results indicate that cortical tension in cultured mammalian cells is comparable to contractile ring tension (Fig. 27), which is in good agreement with the previous work (Sedzinski et al. 2011). Although the mechanism of polar relaxation has been reported in cultured mammalian cells (Rodrigues et al. 2015), no clear cortical flow has been observed (Uehara et al. 2010). Such a high cortical tension is advantageous because it confers shape stability to mitotic cells (Sedzinski et al. 2011). This has been corroborated in a recent paper demonstrating that high cortical stiffness in cancer cells allows them to divide in a confined environment (Matthews et al. 2020). The benefit of cortical tension is not required in *C. elegans* embryos, because they are covered and protected by a rigid eggshell. However, high cortical tension is a double-edged sword, because

excessive cortical tension induces cytokinetic shape oscillation and abscission failure (Mukhina, Wang, and Murata-Hori 2007; Taneja et al. 2020; Girard et al. 2004). The estimated cortical tension relative to ring tension (F_c/F_r), approximately 20%, may achieve a balance between morphological maintenance and timely cytokinesis. Furthermore, the faster furrow ingression in *C. elegans* zygotes (~ 12 μm/min) (Khaliullin et al. 2018) compared to cultured mammalian cells (~ 2 μm/min) may be also explained by the balance between cortical tension and ring tension.

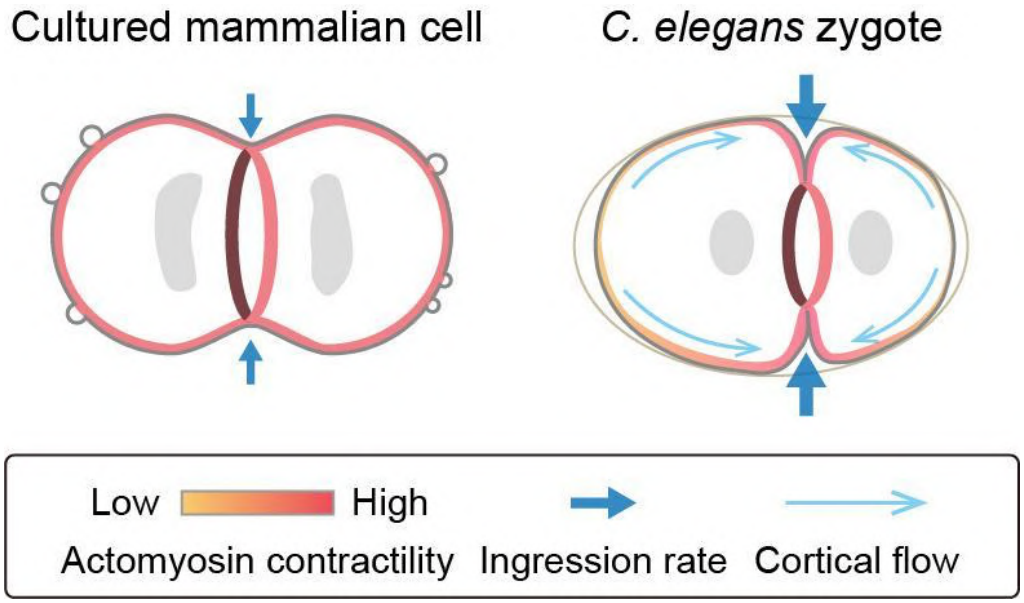

Figure 32. Comparison of cytokinetic mechanics between the cultured mammalian cell and the *C. elegans* zygote.
Schematic illustration describing the differences of cytokinetic mechanics between cultured mammalian cells and *C. elegans* zygotes. In cultured mammalian cells, cortical tension is comparable to contractile ring tension, leading to slower furrow ingression rate. The estimated cortical tension relative to ring tension, approximately 20%, may achieve a balance between morphological maintenance and timely cytokinesis. In *C. elegans* zygotes, the cortical flow induced by polar relaxation causes actomyosin to accumulate at the equator. Thus, cortical tension is much weaker than the ring tension, leading to faster furrow ingression rate.

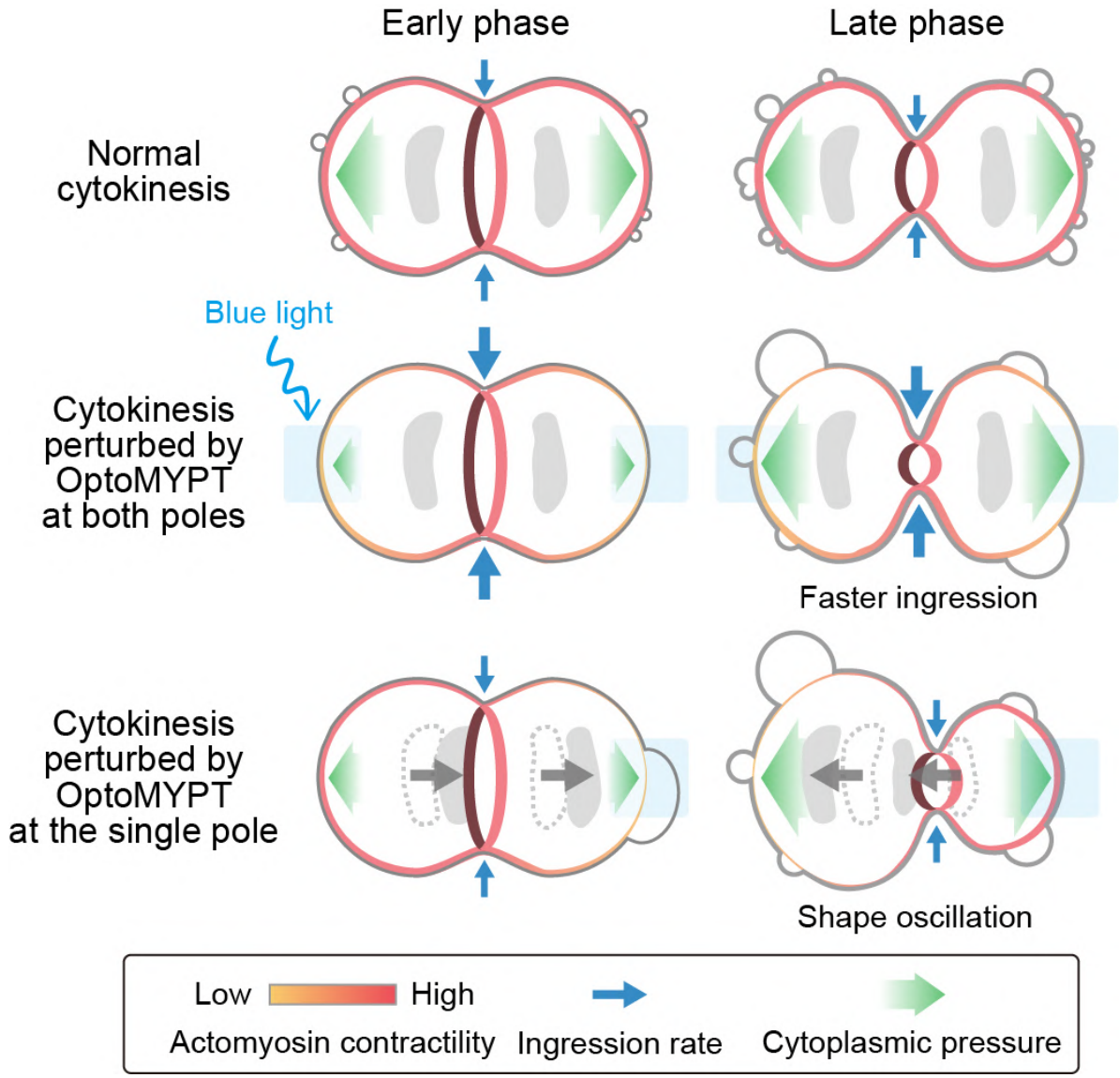

Figure 33. Summary of local perturbation experiments of cortical tension using OptoMYPT.

Schematic model of mechanical regulation of the contractile ring and the actin cortex during cytokinesis. In control cells, high cortical tension acts as a decelerator of the ring constriction. The high cortical tension and cytoplasmic pressure induce blebbing from the early phase of cytokinesis. The increased cytoplasmic pressure associated with ring constriction in the late phase is released by the increased number of blebs. In OptoMYPT-expressing cells illuminated by blue light at both poles, bleb formation is suppressed in the early phase of cytokinesis and the cleavage furrow ingression is accelerated due to the decrease in the cortical tension. As cleavage furrow ingression progresses, large blebs emerge due to the increased cytoplasmic pressure in the late phase of cytokinesis. In OptoMYPT-expressing cells illuminated by blue light at a single pole, the reduced cortical tension at one side leads to the formation of a large bleb and the cytoplasmic flow. The retraction of the bleb induces cell shape oscillation accompanied with the back-and-forth movement of chromosomes.

4.3.2. Estimation of the absolute value of cortical tension and ring tension during cytokinesis.

Due to the highly dynamic nature of cytokinesis, direct measurement of cortical tension during cytokinesis is still technically difficult. Therefore, I attempted to estimate the absolute value of cortical tension during cytokinesis based on previously reported absolute values of ring tension and the OptoMYPT experiments. It has been reported that the ring tension is ~390 pN and 8-15 nN in *S. pombe* spheroplasts and in fertilized echinoderm eggs, respectively (Rappaport 1967; Stachowiak et al. 2014). Based on these reports, I assumed that the ring tension in cultured mammalian cells is 1-5 nN; since the resisting force exerted by the cortices corresponds to at least ~20% of the ring tension based on my experiments, the cortical tension, $2R_rT_c \cos\theta$, is 200-1000 pN. Furthermore, substituting $\cos\theta = 1/2$ and $R_r = 5$ μm, the cortical tension, T_c, is estimated to be 40-200 pN/μm.

Next, I attempted to estimate the absolute value of ring tension based on previously reported cortical tension in cultured mammalian cells. Based on AFM and microaspiration measurements, absolute value of cortical tension is ~ 400 pN/μm, and ~ 1200 pN/μm in trypsinized interphase cells, and metaphase cells, respectively (Chugh et al. 2017; Tinevez et al. 2009). Then, substituting $\cos\theta = 1/2$, $R_r = 5$ μm, and $T_c = 400$-1200 pN/μm, the cortical tension, $2R_rT_c \cos\theta$, is ~2-6 nN. Based on my experiments, ring tension is estimated to be more than 5 times stronger than cortical tension. Therefore, ring tension, T_r, is estimated to be 10-30 nN.

The estimated value of cortical tension, 40-200 pN/μm, seems somewhat low compared to previous measurements, ~ 400 pN/μm, and ~ 1200 pN/μm in trypsinized interphase cells, and metaphase cells, respectively (Chugh et al. 2017; Tinevez et al. 2009). Moreover, the estimated value of ring tension, 10-30 nN seems somewhat high compared to previous reports, ~390 pN and 8-15 nN in *S. pombe* spheroplasts and in fertilized echinoderm

eggs, respectively (Rappaport 1967; Stachowiak et al. 2014). This discrepancy may be further magnified because OptoMYPT might not completely decrease cortical tension; in that case, my estimation of ring tension should be increased. One possibility to explain this discrepancy is cell-cycle dependent changes of tensions; actomyosin is incorporated into the contractile ring when the cells enter the anaphase from the metaphase. In fact, Matzke et al. reported that polar softening occasionally occurs by pole-to-pole scanning using AFM, while equatorial stiffening reproducibly occurs (Matzke, Jacobson, and Radmacher 2001). This supports my idea that the cortical tension decreases after anaphase onset.

We should also pay attention to the estimation of ring tension. The molecular structure and thickness of the contractile ring varies among species. Thus, it is not easy to make a reliable estimation of mammalian ring tension based solely on those tension measurements in yeast and sea urchin. More detailed information on the nano-structure of the contractile ring should be obtained in the future. Similarly, although measurements of cortical tension by AFM and microaspiration are significant, the measured value varies greatly depending on the cell type and methods. Therefore, combined with the uncertainty of ring tension, there is a huge uncertainty (~1-100%) in the estimation of the ratio of cortical tension and ring tension. In this respect, I expect that my method, based on local perturbation using OptoMYPT and measurement of furrow ingression rate, is an accurate estimation of the relative contribution of the cortical tension to ring tension.

4.3.3. Cause of membrane blebbing during cytokinesis.

I also focused on the dynamics of membrane blebbing during cytokinesis (Figs. 26, 31). Membrane blebbing is initiated by local rupture of the actin cortex and/or detachment of the actin cortex from the plasma membrane (Charras and Paluch 2008). The growth of membrane blebs requires a condition under which hydraulic pressure caused by actomyosin-based cortical tension overcomes plasma membrane tension (Tinevez et al. 2009). Using the OptoMYPT system, I showed the absence of membrane blebbing in OptoMYPT-pole cells in the early phase of furrow ingression (Fig. 26c). On the other hand, Rodrigues *et al*. reported that optogenetic inactivation of moesin, a member of the ERM family proteins, induces a bleb from the actin cortex during metaphase (Rodrigues et al. 2015). These opposite effects support that, in OptoMYPT-pole cells, the reduction in cortical tension prevails over the weakening of membrane-cortex linkage which is a possible side effect of OptoMYPT. However, even in OptoMYPT-pole cells, I reproducibly observed membrane blebbing in the late phase (Fig. 26c). Recently, Wang *et al*. have shown that the increase in the extracellular osmotic pressure, i.e., relative decrease in the cytoplasmic pressure, induces the delayed onset of blebbing during cytokinesis (Wang et al. 2021). These results support the idea that the ring constriction gradually increases cytoplasmic pressure, which causes bleb formation in the later phase.

4.3.4. Mechanism of cytokinetic shape oscillation.

In the experiments of single-pole illumination, I often observed cytokinetic shape oscillation. Before the onset of shape oscillation, I observed large blebs in the illuminated region (Fig. 31a, yellow arrowhead), which is consistent with a report showing that cytokinetic oscillation is triggered by the retraction of large blebs (Taneja et al. 2020). This large bleb is probably triggered by the instability of the weakened cortical tension or excessive weakening of cortex-membrane crosslinking. However, the mechanism by which relaxation at a single pole leads to back-and-forth motion is still unclear.

One possibility is that the large blebs promote actomyosin turnover and uptake into the opposite pole with cytoplasmic flow, thereby increasing tension on the opposite side as previously proposed (Sedzinski et al. 2011). The second possibility is based on local calcium dynamics (Fig. 34). Recently, Aoki et al. reported that the influx of ER into the bleb forms STIM1-Orai1 complex leading to increase in the local calcium concentration (Kana Aoki et al. 2021). In general, the increase in calcium concentration increases actomyosin contractility, which increases cortical tension in one daughter cell where the bleb originates. This may cause an influx of cytoplasm to the opposite pole, leading to back-and-forth movement. In future, detailed observation of the dynamics between the bleb and the organelle may help to elucidate the mechanism of shape oscillation. Such studies are expected to contribute to the understanding of various cellular processes, such as amoeboid migration and apoptosis, in which blebs are involved.

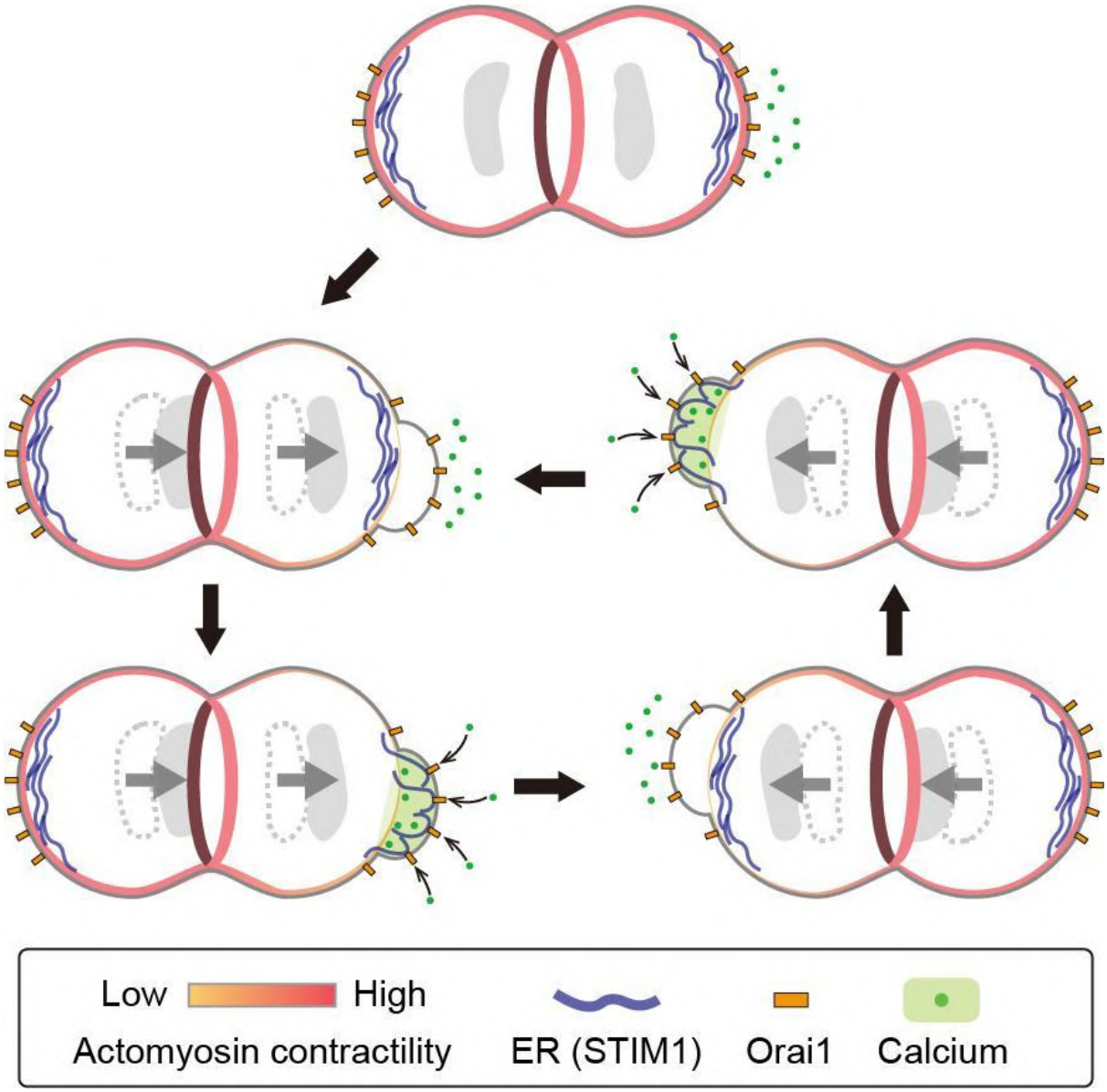

Figure 34. Possible mechanism of cytokinetic shape oscillation.
Schematic illustration describing cytokinetic shape oscillation based on the local calcium dynamics. The large blebs trigger influx of ER into the bleb leading to the formation of STIM1-Orai1 complex. The influx of calcium into the cytoplasm via Orai1 causes reorganization of actomyosin and increases cortical tension. The retraction of the large bleb and/or the increased cortical tension causes a new large bleb in the opposite pole.

4.3.5. Effect of OptoMYPT to the contractile ring.

Local light-illumination to the equatorial region was expected to decelerate the furrow ingression rate. However, it was almost the same as control cells (Fig. 28). This result also supports the possibility that OptoMYPT is less likely to act on highly bundled actin fibers (see section 3.3.2.). In addition, it is technically difficult to confine local activation of OptoMYPT at the contractile ring by conventional confocal microscopy, because of the diffusion of OptoMYPT proteins and the shape of the point spread function on the defocused planes with a high numerical aperture objective lens (Fig. 28). These effects might lead to the dephosphorylation of MLC not only in the contractile ring but also in actin cortices close to the cleavage furrow, thereby masking the effects of OptoMYPT at the contractile ring. It is also plausible that OptoMYPT weakened the viscoelasticity of the contractile ring, resulting in a balance between actomyosin contractile force and viscoelasticity of the contractile ring. The use of a localizer that is closer to endogenous active NMII or a specific localization could result in an OptoMYPT system with better specificity and spatial resolution than the current version (see section 3.3.2.).

5. General Discussion

Future perspective of the OptoMYPT system.

The OptoMYPT system will provide opportunities not only to understand the mechanics of morphogenesis, but also to shape the morphology of cells and tissues with precision and flexibility as desired. Recent papers have applied optogenetic systems *in vivo*, and succeeded in inducing arbitrary forms of apical constriction (Izquierdo, Quinkler, and De Renzis 2018; Martinez-Ara et al. 2021). By combining red light-responsive optogenetic tools such as PhyB-PIF with blue light-responsive tools (Levskaya et al. 2009; Uda et al. 2017), it will be possible to create more sophisticated morphology with an increase or decrease in contractile force in the same cells and tissues.

Unlike previous optogenetic tools for manipulating actomyosin (Valon et al. 2017; Wagner and Glotzer 2016), OptoMYPT is able to act directly on the cytoskeleton. In other words, it does not require an upstream signaling system to regulate actomyosin activity. Such an advantage would be useful in understanding cellular processes by a bottom-up approach. In recent years, attempts have been made to understand cellular processes by reconstituting the cytoskeleton in liposomes containing purified proteins. The reconstituted actin cytoskeleton has been reported to form blebs, contractile rings, and filopodia-like fibers (Miyazaki et al. 2015; Litschel et al. 2021; Loiseau et al. 2016). Future studies using a combination of optogenetics and reconstitution systems are expected to induce more complex deformations, such as cell migration, and provide insights into their mechanisms.

6. References

Aoki, Kana, Shota Harada, Keita Kawaji, Kenji Matsuzawa, Seiichi Uchida, and Junichi Ikenouchi. 2021. "STIM-Orai1 Signaling Regulates Fluidity of Cytoplasm during Membrane Blebbing." *Nature Communications* 12 (1): 480.

Aoki, Kazuhiro, Yuka Kumagai, Atsuro Sakurai, Naoki Komatsu, Yoshihisa Fujita, Clara Shionyu, and Michiyuki Matsuda. 2013. "Stochastic ERK Activation Induced by Noise and Cell-to-Cell Propagation Regulates Cell Density-Dependent Proliferation." *Molecular Cell* 52 (4): 529–40.

Arnold, Torey R., Joseph H. Shawky, Rachel E. Stephenson, Kayla M. Dinshaw, Tomohito Higashi, Farah Huq, Lance A. Davidson, and Ann L. Miller. 2019. "Anillin Regulates Epithelial Cell Mechanics by Structuring the Medial-Apical Actomyosin Network." *eLife* 8 (January). https://doi.org/10.7554/eLife.39065.

Brunner, Edgar, and Ullrich Munzel. 2000. "The Nonparametric Behrens-Fisher Problem: Asymptotic Theory and a Small-Sample Approximation." *Biometrical Journal. Biometrische Zeitschrift* 42 (1): 17–25.

Burnette, Dylan T., Suliana Manley, Prabuddha Sengupta, Rachid Sougrat, Michael W. Davidson, Bechara Kachar, and Jennifer Lippincott-Schwartz. 2011. "A Role for Actin Arcs in the Leading-Edge Advance of Migrating Cells." *Nature Cell Biology* 13 (4): 371–81.

Chang, Audrey N., Ning Gao, Zhenan Liu, Jian Huang, Angus C. Nairn, Kristine E. Kamm, and James T. Stull. 2018. "The Dominant Protein Phosphatase PP1c Isoform in Smooth Muscle Cells, PP1cβ, Is Essential for Smooth Muscle Contraction." *The Journal of Biological Chemistry* 293 (43): 16677–86.

Chapa-Y-Lazo, Bernardo, Motonari Hamanaka, Alexander Wray, Mohan K. Balasubramanian, and Masanori Mishima. 2020. "Polar Relaxation by Dynein-Mediated Removal of Cortical Myosin II." *The Journal of Cell Biology* 219 (8). https://doi.org/10.1083/jcb.201903080.

Charras, Guillaume, and Ewa Paluch. 2008. "Blebs Lead the Way: How to Migrate without Lamellipodia." *Nature Reviews. Molecular Cell Biology* 9 (9): 730–36.

Chugh, Priyamvada, Andrew G. Clark, Matthew B. Smith, Davide A. D. Cassani, Kai Dierkes, Anan Ragab, Philippe P. Roux, Guillaume Charras, Guillaume Salbreux, and Ewa K. Paluch. 2017. "Actin Cortex Architecture Regulates Cell Surface Tension." *Nature Cell Biology* 19 (6): 689–97.

Du, Guangwei, and Michael A. Frohman. 2009. "A Lipid-Signaled Myosin Phosphatase Surge Disperses Cortical Contractile Force Early in Cell Spreading." *Molecular Biology of the Cell* 20 (1): 200–208.

Even-Ram, Sharona, Andrew D. Doyle, Mary Anne Conti, Kazue Matsumoto, Robert S. Adelstein, and Kenneth M. Yamada. 2007. "Myosin IIA Regulates Cell Motility and Actomyosin-Microtubule Crosstalk." *Nature Cell Biology* 9 (3): 299–309.

Girard, Kristine D., Charles Chaney, Michael Delannoy, Scot C. Kuo, and Douglas N. Robinson. 2004. "Dynacortin Contributes to Cortical Viscoelasticity and Helps Define the Shape Changes of Cytokinesis." *The EMBO Journal* 23 (7): 1536–46.

Gómez-González, Manuel, Ernest Latorre, Marino Arroyo, and Xavier Trepat. 2020. "Measuring Mechanical Stress in Living Tissues." *Nature Reviews Physics*, May. https://doi.org/10.1038/s42254-020-0184-6.

Green, Rebecca A., Ewa Paluch, and Karen Oegema. 2012. "Cytokinesis in Animal Cells." *Annual Review of Cell and Developmental Biology* 28 (1): 29–58.

Guglielmi, Giorgia, Joseph D. Barry, Wolfgang Huber, and Stefano De Renzis. 2015. "An Optogenetic Method to Modulate Cell Contractility during Tissue Morphogenesis."

Developmental Cell 35 (5): 646–60.
Guntas, Gurkan, Ryan A. Hallett, Seth P. Zimmerman, Tishan Williams, Hayretin Yumerefendi, James E. Bear, and Brian Kuhlman. 2015. "Engineering an Improved Light-Induced Dimer (iLID) for Controlling the Localization and Activity of Signaling Proteins." *Proceedings of the National Academy of Sciences of the United States of America* 112 (1): 112–17.
Hara, Yusuke. 2017. "Contraction and Elongation: Mechanics Underlying Cell Boundary Deformations in Epithelial Tissue." *Development, Growth & Differentiation* 59 (5): 340–50.
Hara, Yusuke, Kazuaki Nagayama, Takamasa S. Yamamoto, Takeo Matsumoto, Makoto Suzuki, and Naoto Ueno. 2013. "Directional Migration of Leading-Edge Mesoderm Generates Physical Forces: Implication in Xenopus Notochord Formation during Gastrulation." *Developmental Biology* 382 (2): 482–95.
Hara, Yusuke, Murat Shagirov, and Yusuke Toyama. 2016. "Cell Boundary Elongation by Non-Autonomous Contractility in Cell Oscillation." *Current Biology: CB* 26 (17): 2388–96.
Hashimoto, Hidehiko, and Edwin Munro. 2019. "Differential Expression of a Classic Cadherin Directs Tissue-Level Contractile Asymmetry during Neural Tube Closure." *Developmental Cell* 51 (2): 158–72.e4.
Heissler, Sarah M., and Dietmar J. Manstein. 2013. "Nonmuscle Myosin-2: Mix and Match." *Cellular and Molecular Life Sciences: CMLS* 70 (1): 1–21.
Hirano, K., B. C. Phan, and D. J. Hartshorne. 1997. "Interactions of the Subunits of Smooth Muscle Myosin Phosphatase." *The Journal of Biological Chemistry* 272 (6): 3683–88.
Huber, Florian, Adeline Boire, Magdalena Preciado López, and Gijsje H. Koenderink. 2015. "Cytoskeletal Crosstalk: When Three Different Personalities Team up." *Current Opinion in Cell Biology* 32 (February): 39–47.
Ito, Masaaki, Takeshi Nakano, Ferenc Erd, and David J. Hartshorne. 2004. "Myosin Phosphatase: Structure, Regulation and Function." *Molecular and Cellular Biochemistry* 259: 197–209.
Iyer, K. Venkatesan, Romina Piscitello-Gómez, Joris Paijmans, Frank Jülicher, and Suzanne Eaton. 2019. "Epithelial Viscoelasticity Is Regulated by Mechanosensitive E-Cadherin Turnover." *Current Biology: CB* 29 (4): 578–91.e5.
Kelkar, Manasi, Pierre Bohec, and Guillaume Charras. 2020. "Mechanics of the Cellular Actin Cortex: From Signalling to Shape Change." *Current Opinion in Cell Biology* 66 (June): 69–78.
Kennedy, Matthew J., Robert M. Hughes, Leslie A. Peteya, Joel W. Schwartz, Michael D. Ehlers, and Chandra L. Tucker. 2010. "Rapid Blue-Light-Mediated Induction of Protein Interactions in Living Cells." *Nature Methods* 7 (12): 973–75.
Khaliullin, Renat N., Rebecca A. Green, Linda Z. Shi, J. Sebastian Gomez-Cavazos, Michael W. Berns, Arshad Desai, and Karen Oegema. 2018. "A Positive-Feedback-Based Mechanism for Constriction Rate Acceleration during Cytokinesis in Caenorhabditis Elegans." *eLife* 7 (July). https://doi.org/10.7554/eLife.36073.
Kazushi, Kimura, Masaaki Ito, Mutsuki Amano, Kazuyasu Chihara, Yuko Fukata, Masato Nakafuku, Bunpei Yamamori, Jianhua Feng, Takeshi Nakano, Katsuya Okawa, Akihiro Iwamatsu, and Kozo Kaibuchi. 1996. "Regulation of Myosin Phosphatase by Rho ad Rho-Associated Kinase (Rho-Kinase)." Science 273 (5272): 245-248.
Kinoshita, Noriyuki, Yutaka Hashimoto, Naoko Yasue, Makoto Suzuki, Ileana M. Cristea, and Naoto Ueno. 2020. "Mechanical Stress Regulates Epithelial Tissue Integrity and Stiffness through the FGFR/Erk2 Signaling Pathway during Embryogenesis." *Cell Reports* 30 (11): 3875–88.e3.
Kiss, Andrea, Beáta Lontay, Bálint Bécsi, László Márkász, Eva Oláh, Pál Gergely, and Ferenc Erdodi. 2008. "Myosin Phosphatase Interacts with and Dephosphorylates the Retinoblastoma Protein in THP-1 Leukemic Cells: Its Inhibition Is Involved in the Attenuation of Daunorubicin-Induced Cell Death by Calyculin-A." *Cellular Signalling* 20 (11): 2059–70.

Klewer, Laura, and Yao-Wen Wu. 2019. “Light-Induced Dimerization Approaches to Control Cellular Processes.” *Chemistry* 25 (54): 12452–63.

Kondo, Tomo, Kozue Hamao, Keiju Kamijo, Hiroshi Kimura, Makiko Morita, Masayuki Takahashi, and Hiroshi Hosoya. 2011. “Enhancement of Myosin II/actin Turnover at the Contractile Ring Induces Slower Furrowing in Dividing HeLa Cells.” *Biochemical Journal* 435 (3): 569–76.

Krueger, Daniel, Emiliano Izquierdo, Ranjith Viswanathan, Jonas Hartmann, Cristina Pallares Cartes, and Stefano De Renzis. 2019. “Principles and Applications of Optogenetics in Developmental Biology.” *Development* 146 (20). https://doi.org/10.1242/dev.175067.

Kunda, Patricia, Andrew E. Pelling, Tao Liu, and Buzz Baum. 2008. “Moesin Controls Cortical Rigidity, Cell Rounding, and Spindle Morphogenesis during Mitosis.” *Current Biology: CB* 18 (2): 91–101.

Kuragano, Masahiro, Yota Murakami, and Masayuki Takahashi. 2018. “Nonmuscle Myosin IIA and IIB Differentially Contribute to Intrinsic and Directed Migration of Human Embryonic Lung Fibroblasts.” *Biochemical and Biophysical Research Communications* 498 (1): 25–31.

Laplaud, Valentin, Nicolas Levernier, Judith Pineau, Mabel San Roman, Lucie Barbier, Pablo J. Sáez, Ana-Maria Lennon-Duménil, et al. 2021. “Pinching the Cortex of Live Cells Reveals Thickness Instabilities Caused by Myosin II Motors.” *Science Advances* 7 (27). https://doi.org/10.1126/sciadv.abe3640.

Levskaya, Anselm, Orion D. Weiner, Wendell A. Lim, and Christopher A. Voigt. 2009. “Spatiotemporal Control of Cell Signalling Using a Light-Switchable Protein Interaction.” *Nature* 461 (7266): 997–1001.

Litschel, Thomas, Charlotte F. Kelley, Danielle Holz, Maral Adeli Koudehi, Sven K. Vogel, Laura Burbaum, Naoko Mizuno, Dimitrios Vavylonis, and Petra Schwille. 2021. “Reconstitution of Contractile Actomyosin Rings in Vesicles.” *Nature Communications* 12 (1): 1–10.

Liu, Yan-Jun, Maël Le Berre, Franziska Lautenschlaeger, Paolo Maiuri, Andrew Callan-Jones, Mélina Heuzé, Tohru Takaki, Raphaël Voituriez, and Matthieu Piel. 2015. “Confinement and Low Adhesion Induce Fast Amoeboid Migration of Slow Mesenchymal Cells.” *Cell* 160 (4): 659–72.

Loiseau, Etienne, Jochen A. M. Schneider, Felix C. Keber, Carina Pelzl, Gladys Massiera, Guillaume Salbreux, and Andreas R. Bausch. 2016. “Shape Remodeling and Blebbing of Active Cytoskeletal Vesicles.” *Science Advances* 2 (4): e1500465.

Loria, Andy, Katrina M. Longhini, and Michael Glotzer. 2012. “The RhoGAP Domain of CYK-4 Has an Essential Role in RhoA Activation.” *Current Biology: CB* 22 (3): 213–19.

Martin, Adam C., and Bob Goldstein. 2014. “Apical Constriction: Themes and Variations on a Cellular Mechanism Driving Morphogenesis.” *Development* 141 (10): 1987–98.

Matthews, Helen K., Sushila Ganguli, Katarzyna Plak, Anna V. Taubenberger, Zaw Win, Max Williamson, Matthieu Piel, Jochen Guck, and Buzz Baum. 2020. “Oncogenic Signaling Alters Cell Shape and Mechanics to Facilitate Cell Division under Confinement.” *Developmental Cell* 52 (5): 563–73.e3.

Matzke, R., K. Jacobson, and M. Radmacher. 2001. “Direct, High-Resolution Measurement of Furrow Stiffening during Division of Adherent Cells.” *Nature Cell Biology* 3 (6): 607–10.

Mii, Yusuke, and Masanori Taira. 2009. “Secreted Frizzled-Related Proteins Enhance the Diffusion of Wnt Ligands and Expand Their Signalling Range.” *Development* 136 (24): 4083–88.

Miyazaki, Makito, Masataka Chiba, Hiroki Eguchi, Takashi Ohki, and Shin’ichi Ishiwata. 2015. “Cell-Sized Spherical Confinement Induces the Spontaneous Formation of Contractile Actomyosin Rings in Vitro.” *Nature Cell Biology* 17 (4): 480–89.

Mukhina, Svetlana, Yu-Li Wang, and Maki Murata-Hori. 2007. “Alpha-Actinin Is Required for Tightly Regulated Remodeling of the Actin Cortical Network during Cytokinesis.” *Developmental Cell* 13 (4): 554–65.

Murrell, Michael, Patrick W. Oakes, Martin Lenz, and Margaret L. Gardel. 2015. “Forcing Cells into Shape: The Mechanics of Actomyosin Contractility.” *Nature Reviews. Molecular Cell Biology* 16 (8): 486–98.

Murthy, Kausalya, and Patricia Wadsworth. 2005. “Myosin-II-Dependent Localization and Dynamics of F-Actin during Cytokinesis.” *Current Biology: CB* 15 (8): 724–31.

Narumiya, Shuh, Masahiro Tanji, and Toshimasa Ishizaki. 2009. “Rho Signaling, ROCK and mDia1, in Transformation, Metastasis and Invasion.” *Cancer Metastasis Reviews* 28 (1-2): 65–76.

Natwick, Dean E., and Sean R. Collins. 2021. “Optimized iLID Membrane Anchors for Local Optogenetic Protein Recruitment.” *ACS Synthetic Biology*, April. https://doi.org/10.1021/acssynbio.0c00511.

Niwa, H., K. Yamamura, and J. Miyazaki. 1991. “Efficient Selection for High-Expression Transfectants with a Novel Eukaryotic Vector.” *Gene* 108 (2): 193–99.

Oakes, Patrick W., Elizabeth Wagner, Christoph A. Brand, Dimitri Probst, Marco Linke, Ulrich S. Schwarz, Michael Glotzer, and Margaret L. Gardel. 2017. “Optogenetic Control of RhoA Reveals Zyxin-Mediated Elasticity of Stress Fibres.” *Nature Communications* 8 (June): 15817.

O’Connell, C. B., A. K. Warner, and Y. Wang. 2001. “Distinct Roles of the Equatorial and Polar Cortices in the Cleavage of Adherent Cells.” *Current Biology: CB* 11 (9): 702–7.

Oshiro, Noriko, Yuko Fukata, and Kozo Kaibuchi. 1998. “Phosphorylation of Moesin by Rho-Associated Kinase (Rho-Kinase) Plays a Crucial Role in the Formation of Microvilli-like Structures *.” *The Journal of Biological Chemistry* 273 (52): 34663–66.

Pagès, Diane-Laure, Emmanuel Dornier, Jean De Seze, Li Wang, Rui Luan, Jérôme Cartry, Charlotte Canet-Jourdan, et al. 2020. “Cell Clusters Adopt a Collective Amoeboid Mode of Migration in Confined Non-Adhesive Environments.” *bioRxiv*. https://doi.org/10.1101/2020.05.28.106203.

Paluch, Ewa K., Irene M. Aspalter, and Michael Sixt. 2016. “Focal Adhesion-Independent Cell Migration.” *Annual Review of Cell and Developmental Biology* 32 (October): 469–90.

Piekny, Alisa J., and Michael Glotzer. 2008. “Anillin Is a Scaffold Protein That Links RhoA, Actin, and Myosin during Cytokinesis.” *Current Biology: CB* 18 (1): 30–36.

Pollard, Thomas D. 2010. “Mechanics of Cytokinesis in Eukaryotes.” *Current Opinion in Cell Biology* 22 (1): 50–56.

Priya, Rashmi, Guillermo A. Gomez, Srikanth Budnar, Suzie Verma, Hayley L. Cox, Nicholas A. Hamilton, and Alpha S. Yap. 2015. “Feedback Regulation through Myosin II Confers Robustness on RhoA Signalling at E-Cadherin Junctions.” *Nature Cell Biology* 17 (10): 1282–93.

Rappaport, R. 1967. “Cell Division: Direct Measurement of Maximum Tension Exerted by Furrow of Echinoderm Eggs.” *Science* 156 (3779): 1241–43.

Reymann, Anne-Cecile, Fabio Staniscia, Anna Erzberger, Guillaume Salbreux, and Stephan W. Grill. 2016. “Cortical Flow Aligns Actin Filaments to Form a Furrow.” *eLife* 5 (October). https://doi.org/10.7554/eLife.17807.

Ridley, Anne J., Martin A. Schwartz, Keith Burridge, Richard A. Firtel, Mark H. Ginsberg, Gary Borisy, J. Thomas Parsons, and Alan Rick Horwitz. 2003. “Cell Migration: Integrating Signals from Front to Back.” *Science* 302 (5651): 1704–9.

Riedl, Julia, Alvaro H. Crevenna, Kai Kessenbrock, Jerry Haochen Yu, Dorothee Neukirchen, Michal Bista, Frank Bradke, et al. 2008. “Lifeact: A Versatile Marker to Visualize F-Actin.” *Nature Methods* 5 (7): 605–7.

Rodrigues, Nelio T. L., Sergey Lekomtsev, Silvana Jananji, Janos Kriston-Vizi, Gilles R. X. Hickson, and Buzz Baum. 2015. “Kinetochore-Localized PP1-Sds22 Couples Chromosome Segregation to Polar Relaxation.” *Nature* 524 (7566): 489–92.

Roney, Ian J., Adam D. Rudner, Jean-François Couture, and Mads Kærn. 2016. “Improvement of the

Reverse Tetracycline Transactivator by Single Amino Acid Substitutions That Reduce Leaky Target Gene Expression to Undetectable Levels." *Scientific Reports* 6 (June): 27697.

Ruprecht, Verena, Stefan Wieser, Andrew Callan-Jones, Michael Smutny, Hitoshi Morita, Keisuke Sako, Vanessa Barone, et al. 2015. "Cortical Contractility Triggers a Stochastic Switch to Fast Amoeboid Cell Motility." *Cell* 160 (4): 673–85.

Saitoh, M., T. Ishikawa, S. Matsushima, M. Naka, and H. Hidaka. 1987. "Selective Inhibition of Catalytic Activity of Smooth Muscle Myosin Light Chain Kinase." *The Journal of Biological Chemistry* 262 (16): 7796–7801.

Sedzinski, Jakub, Maté Biro, Annelie Oswald, Jean Yves Tinevez, Guillaume Salbreux, and Ewa Paluch. 2011. "Polar Actomyosin Contractility Destabilizes the Position of the Cytokinetic Furrow." *Nature* 476 (7361): 462–68.

Silver, D. L., A. V. Vorotnikov, D. M. Watterson, V. P. Shirinsky, and J. R. Sellers. 1997. "Sites of Interaction between Kinase-Related Protein and Smooth Muscle Myosin." *The Journal of Biological Chemistry* 272 (40): 25353–59.

Stachowiak, Matthew R., Caroline Laplante, Harvey F. Chin, Boris Guirao, Erdem Karatekin, Thomas D. Pollard, and Ben O'Shaughnessy. 2014. "Mechanism of Cytokinetic Contractile Ring Constriction in Fission Yeast." *Developmental Cell* 29 (5): 547–61.

Straight, Aaron F., Amy Cheung, John Limouze, Irene Chen, Nick J. Westwood, James R. Sellers, and Timothy J. Mitchison. 2003. "Dissecting Temporal and Spatial Control of Cytokinesis with a Myosin II Inhibitor." *Science* 299 (5613): 1743–47.

Straight, Aaron F., Christine M. Field, and Timothy J. Mitchison. 2005. "Anillin Binds Nonmuscle Myosin II and Regulates the Contractile Ring." *Molecular Biology of the Cell* 16 (1): 193–201.

Tanaka, J., M. Ito, J. Feng, K. Ichikawa, T. Hamaguchi, M. Nakamura, D. J. Hartshorne, and T. Nakano. 1998. "Interaction of Myosin Phosphatase Target Subunit 1 with the Catalytic Subunit of Type 1 Protein Phosphatase." *Biochemistry* 37 (47): 16697–703.

Taneja, Nilay, Matthew R. Bersi, Sophie M. Baillargeon, Aidan M. Fenix, James A. Cooper, Ryoma Ohi, Vivian Gama, W. David Merryman, and Dylan T. Burnette. 2020. "Precise Tuning of Cortical Contractility Regulates Cell Shape during Cytokinesis." *Cell Reports* 31 (1): 107477.

Tinevez, Jean-Yves, Ulrike Schulze, Guillaume Salbreux, Julia Roensch, Jean-François Joanny, and Ewa Paluch. 2009. "Role of Cortical Tension in Bleb Growth." *Proceedings of the National Academy of Sciences of the United States of America* 106 (44): 18581–86.

Totsukawa, Go, Yue Wu, Yasuharu Sasaki, David J. Hartshorne, Yoshihiko Yamakita, Shigeko Yamashiro, and Fumio Matsumura. 2004. "Distinct Roles of MLCK and ROCK in the Regulation of Membrane Protrusions and Focal Adhesion Dynamics during Cell Migration of Fibroblasts." *The Journal of Cell Biology* 164 (3): 427–39.

Truong Quang, Binh An, Ruby Peters, Davide A. D. Cassani, Priyamvada Chugh, Andrew G. Clark, Meghan Agnew, Guillaume Charras, and Ewa K. Paluch. 2021. "Extent of Myosin Penetration within the Actin Cortex Regulates Cell Surface Mechanics." *Nature Communications* 12 (1): 6511.

Tse, Justin R., and Adam J. Engler. 2010. "Preparation of Hydrogel Substrates with Tunable Mechanical Properties." *Current Protocols in Cell Biology / Editorial Board, Juan S. Bonifacino ... [et Al.]* Chapter 10 (June): Unit 10.16.

Turlier, Hervé, Basile Audoly, Jacques Prost, and Jean-François Joanny. 2014. "Furrow Constriction in Animal Cell Cytokinesis." *Biophysical Journal* 106 (1): 114–23.

Uda, Youichi, Yuhei Goto, Shigekazu Oda, Takayuki Kohchi, Michiyuki Matsuda, and Kazuhiro Aoki. 2017. "Efficient Synthesis of Phycocyanobilin in Mammalian Cells for Optogenetic Control of Cell Signaling." *Proceedings of the National Academy of Sciences* 114 (45): 11962–67.

Uehara, Ryota, Gohta Goshima, Issei Mabuchi, Ronald D. Vale, James A. Spudich, and Eric R. Griffis. 2010. “Determinants of Myosin II Cortical Localization during Cytokinesis.” *Current Biology: CB* 20 (12): 1080–85.

Uehata, M., T. Ishizaki, H. Satoh, T. Ono, T. Kawahara, T. Morishita, H. Tamakawa, et al. 1997. “Calcium Sensitization of Smooth Muscle Mediated by a Rho-Associated Protein Kinase in Hypertension.” *Nature* 389 (6654): 990–94.

Uyeda, Taro Q. P., Yoshiaki Iwadate, Nobuhisa Umeki, Akira Nagasaki, and Shigehiko Yumura. 2011. “Stretching Actin Filaments within Cells Enhances Their Affinity for the Myosin Ii Motor Domain.” *PloS One* 6 (10). https://doi.org/10.1371/journal.pone.0026200.

Valon, Léo, Ariadna Marín-Llauradó, Thomas Wyatt, Guillaume Charras, and Xavier Trepat. 2017. “Optogenetic Control of Cellular Forces and Mechanotransduction.” *Nature Communications* 8 (February): 14396.

Varadarajan, Saranyaraajan, Rachel E. Stephenson, Eileen R. Misterovich, Jessica L. Wu, Ivan S. Erofeev, Andrew B. Goryachev, and Ann L. Miller. 2021. “Mechanosensitive Calcium Signaling in Response to Cell Shape Changes Promotes Epithelial Tight Junction Remodeling by Activating RhoA.” *bioRxiv*. https://doi.org/10.1101/2021.05.18.444663.

Vicente-Manzanares, Miguel, Margaret A. Koach, Leanna Whitmore, Marcelo L. Lamers, and Alan F. Horwitz. 2008. “Segregation and Activation of Myosin IIB Creates a Rear in Migrating Cells.” *The Journal of Cell Biology* 183 (3): 543–54.

Vicente-Manzanares, M., X. Ma, R. S. Adelstein, and A. R. Horwitz. 2009. “Non-Muscle Myosin II Takes Centre Stage in Cell Adhesion and Migration.” *Nature reviews.Molecular Cell Biology* 10 (11): 778–90.

Vielemeyer, Ole, Clément Nizak, Ana Joaquina Jimenez, Arnaud Echard, Bruno Goud, Jacques Camonis, Jean-Christophe Rain, and Franck Perez. 2010. “Characterization of Single Chain Antibody Targets through Yeast Two Hybrid.” *BMC Biotechnology* 10 (August): 59.

Wagner, Elizabeth, and Michael Glotzer. 2016. “Local RhoA Activation Induces Cytokinetic Furrows Independent of Spindle Position and Cell Cycle Stage.” *The Journal of Cell Biology* 213 (6): 641–49.

Wang, Xiaohuan, Long Li, Yingfeng Shao, Jiachen Wei, Ruopu Song, Songjie Zheng, Yuqiao Li, and Fan Song. 2021. “Effects of the Laplace Pressure on the Cells during Cytokinesis.” *iScience* 24 (9): 102945.

Wiggan, O ’neil, Alisa E. Shaw, Jennifer G. DeLuca, and James R. Bamburg. 2012. “ADF/cofilin Regulates Actomyosin Assembly through Competitive Inhibition of Myosin II Binding to F-Actin.” *Developmental Cell* 22 (3): 530–43.

Worthylake, Rebecca A., and Keith Burridge. 2003. “RhoA and ROCK Promote Migration by Limiting Membrane Protrusions *.” *The Journal of Biological Chemistry* 278 (15): 13578–84.

Wu, Yue, Andrea Murányi, Ferenc Erdodi, and David J. Hartshorne. 2005. “Localization of Myosin Phosphatase Target Subunit and Its Mutants.” *Journal of Muscle Research and Cell Motility* 26 (2-3): 123–34.

Yamamoto, Kei, Kohei Otomo, Tomomi Nemoto, Seiichiro Ishihara, Hisashi Haga, Akira Nagasaki, Yota Murakami, and Masayuki Takahashi. 2019. “Differential Contributions of Nonmuscle Myosin IIA and IIB to Cytokinesis in Human Immortalized Fibroblasts.” *Experimental Cell Research*. https://doi.org/10.1016/j.yexcr.2019.01.020.

Yoneda, M., and K. Dan. 1972. “Tension at the Surface of the Dividing Sea-Urchin Egg.” *The Journal of Experimental Biology* 57 (3): 575–87.

Yonemura, Shigenobu, Takeshi Matsui, Shoichiro Tsukita, and Sachiko Tsukita. 2002. “Rho-Dependent and -Independent Activation Mechanisms of Ezrin/radixin/moesin Proteins: An Essential Role for Polyphosphoinositides in Vivo.” *Journal of Cell Science* 115 (Pt 12): 2569–

80.
Yusa, Kosuke, Liqin Zhou, Meng Amy Li, Allan Bradley, and Nancy L. Craig. 2011. “A Hyperactive piggyBac Transposase for Mammalian Applications.” *Proceedings of the National Academy of Sciences of the United States of America* 108 (4): 1531–36.
Zajac, Olivier, Joel Raingeaud, Fotine Libanje, Celine Lefebvre, Dora Sabino, Isabelle Martins, Pétronille Roy, et al. 2018. “Tumour Spheres with Inverted Polarity Drive the Formation of Peritoneal Metastases in Patients with Hypermethylated Colorectal Carcinomas.” *Nature Cell Biology* 20 (3): 296–306.
Zhang, Donglei, and Michael Glotzer. 2015. “The RhoGAP Activity of CYK-4/MgcRacGAP Functions Non-Canonically by Promoting RhoA Activation during Cytokinesis.” *eLife* 4 (August). https://doi.org/10.7554/eLife.08898.
Zhang, Wendy, and Douglas N. Robinson. 2005. “Balance of Actively Generated Contractile and Resistive Forces Controls Cytokinesis Dynamics.” *Proceedings of the National Academy of Sciences of the United States of America* 102 (20): 7186–91.

Acknowledgements

I would like to thank my supervisor Professor Kazuhiro Aoki for giving me the opportunity to study as a Ph.D. student in his laboratory. I am also grateful to assistant professor Yohei Kondo and Dr. Haruko Miura for helpful daily discussion, and guidance. This work would have not been possible without their understanding and support.

I would like to thank the collaborators, Dr. Yusuke Mii and Dr. Shinji Takada for supporting *Xenopus* experiments, Dr. Noriyuki Kinoshita and Dr. Naoto Ueno for laser ablation experiments, Dr. Motohiro Ishida and Dr. Satoshi Sawai for providing plasmids for iLID-SspB optogenetic system. I would also like to thank Dr. Miki Ebisuya and Dr. Masayuki Takahashi for helpful advice and discussions.

This work was supported by Japan Society for the Promotion of Science (JSPS) Research Fellowships for Young Scientists.

Finally, I am grateful to all the lab members in the Division of Quantitative Biology in NIBB for assisting me with experiments and daily life.